2013

Exchange Coupling In Molecular Magnets: Zero, One And Three Dimensions

Asma Amjad
University of Central Florida

STARS Citation

Amjad, Asma, "Exchange Coupling In Molecular Magnets: Zero, One And Three Dimensions" (2013). *Electronic Theses and Dissertations, 2004-2019*. 2597.
https://stars.library.ucf.edu/etd/2597

EXCHANGE COUPLING IN MOLECULAR MAGNETS: ZERO, ONE AND THREE DIMENSIONS

by

ASMA AMJAD
MS. Quaid-i-Azam University, 2005
M.phil. Quaid-i-Azam University, 2007

A dissertation submitted in partial fulfillment of the requirements
for the degree of Doctor of Philosophy
in the Department of Physics
in the College of Sciences
at the University of Central Florida
Orlando, Florida

Summer Term
2013

Major Professor: Enrique del Barco

ABSTRACT

Molecular magnets with different dimensionality, whether they are zero-dimensional single-molecule magnets (SMM) or one-dimensional single-chain magnets (SCM) are very interesting, since they allow probing the fundamental aspects bordering quantum and classical physics at the nanoscale level. This dissertation covers experimental studies of two Mn-based exchange-coupled molecule-based magnets and two Co-based single-chain magnets, using both dc Hall-effect magnetometry and electron paramagnet resonance (EPR) techniques. In these multi-dimensional systems, the spin of the molecule exhibits quantum mechanical behavior at low temperature. It is quite interesting to observe the effect of magnetic exchange interactions on the magnetic properties of various complexes; hence they strongly affect the magnetic behavior.

In this dissertation, the research is initiated with the study of low-magnetic-nuclearity molecules, starting with a spectroscopic study of a significantly anisotropic Mn(IV) monomer. At low temperature the molecule possesses easy-plane type anisotropy of a remarkable magnitude. Although the molecule is not a single-molecule magnet, the remarkable anisotropy can initiate synthesis of newer and better molecular magnets with Mn(IV) as the main building block.

Furthermore, the interplay between the magnetic anisotropy and the inter-ion exchange interactions (*J*) within the molecule are probed for a dimer and a trimer where the magnetic core is comprised of two and three ions respectively. In the Mn-based case of the dimer, the low coupling between the atoms leads to significant state mixing, thus making it impossible to assign the individual spin states to the dimer or to the respective individual Mn(II) ions. In the case of

the trimer, lowering of the symmetry achieved by fine tuning of the inter-ion exchange interactions leads to relieving of frustration in the antiferromagnetic (AF) triangular Mn(III) system, resulting in a well defined ground state and significant zero field splitting. Also a clear hysteretic behavior observed in this system demonstrates its SMM nature at low temperature.

Finally, high-field high-frequency magnetic and spectroscopic studies performed on two cobalt-based SCMs reveal that formation of magnetic domains by exchange interactions within the chain are strongly influenced by thermal fluctuations. The chain possesses a uniaxial anisotropy with the quantization axis lying along the length of the chain. Moreover it is shown that modulation of the magnitude of inter- and intra-chain interactions results in a three-dimensional dynamics in one of the samples. Interestingly, detailed dc magnetic studies show a tunable crossover between one- and three-dimensional magnetic dynamics as a function of temperature and/or magnetic field sweep rate.

Our voyage through several molecular systems of different dimensionality have allowed us to expand our understanding of the role of exchange interactions on the magnetic behavior in molecular magnetism.

ACKNOWLEDGMENTS

Many people have helped me succeed and accomplish the goals I set for myself during the course of my PhD. I would like to take this opportunity to thank them for their kind support and faith in my capabilities.

I would like to thank my advisor Dr. Enrique del Barco for taking me under his wing, for his guidance and advice he provided during the course of my research. He was kind enough to provide me financial support for my tuition whenever there was a need and he had the means.

I would like to thank the members of my dissertation committee, Dr. Richard Klemm, Dr. Robert Peale and Dr. Stephen Hill for their guidance. I must extend special thanks to Dr. Hill for accepting my proposal to spend the summer of 2012 in the National High Magnetic field Lab (NHMFL), Tallahassee. He was kind enough to teach me the nuts and bolts of his lab, I had an amazing time at the EMR facility working at different spectrometers available and I ended up spending most part of 2012 there. I am thankful to Dr. Johan van Tol and Dr. Andrzej Ozarowski for letting me work at their setups, for helping me analyze the results and providing very useful inputs. It goes without saying that my stay at Tallahassee was a success not only because I worked on multiple projects but also because of the new friends I made. I would like to thank Dr. Hill’s current and former graduate students and post docs for treating me as part of the group, we had a fun time doing experiments, discussions and trying out new restaurants. Sincerest thanks to Dr. Komu for helping me out at the end with my housing situation.

Many thanks, to my former and current group members at UCF for a wonderful experience and special thanks to Dr. Firoze ul Haque for teaching and helping me with the instruments in our lab. Thanks to David Bradford for all the help in the machine shop. Many thanks to the Chair of the department Dr. Talat Rahman for providing very useful advice and helping me out with my funds situation.

Life in graduate school is fun and tough, and one cannot bear it without friends. I would like to thank my study partner and my best friend Ahmed El Halawany, for his advice, encouragements and faith in my capabilities. We had an awesome time exploring the field of Physics and the states of US, and I wish him the very best in his future endeavors.

I would like to take this opportunity to acknowledge my mentor and teacher Dr. S. K. Hasanain. I want to thank him for his encouragement and the faith he showed in presenting me the opportunity to study in US on a scholarship and accomplish one of the greatest achievements of my life. It wouldn’t have been a smooth journey if I were not getting my funds regularly, so thanks to Pakistan’s funding agency.

Last but not least, I want to express my deepest gratitude towards my parents, my brothers and my sister in law. It was their continuous love, support and nonstop tales of my niece and nephew’s mind boggling adventures and schemes, that kept me on track and I never felt away from home. Many thanks, to my younger brother Ayyaz for being the best confidant ever. My friends in Pakistan, especially Zonz and Wafa, they were by my side throughout the years; I spent trying to design the course of my research and deal with the problems that were part of this journey. I love them and I wish them the very best in life.

Dedicated to Mr & Mrs Amjad Chattha (my Parents)

&

every single person in my life who believed in me

TABLE OF CONTENTS

LIST OF FIGURES

LIST OF TABLES

LIST OF ABBREVIATIONS

1D	One dimensional
3D	Three dimensional
AF	Antiferromagnetic
EPR	Electron Paramagnetic Resonance
FM	Ferromagnetic
GSA	Giant-Spin Approximation
JT	Jahn-Teller
MS	Multi-Spin
QTM	Quantum Tunneling of Magnetization
SCM	Single-Chain Magnet
SMM	Single-Molecule Magnet
ZFC	Zero-Field Cool
ZFC-FC	Zero-Field Cool Field Cool
ZFS	Zero-Field Splitting

CHAPTER 1 INTRODUCTION

1.1 Molecular magnetism

The field of molecular magnetism has provided a new class of magnetic materials based on molecular lattices instead of the normally occurring classical magnets. The properties of the new materials lie in between those of isolated paramagnets and those of bulk magnets [1,2]. In the field of molecular magnetism, the leading materials under study are multifunctional magnetic materials; nano magnetic materials and molecular nanomagnets. In this thesis the focus on single-molecule magnets (SMM) and single-chain magnets (SCM), which have became the prime focus of interest among physicists and chemists equally because of their intriguing nature; which allows them to behave as a permanent magnets exhibiting magnetic hysteresis and simultaneously one can observe quantum effects due to the small sizes, such as quantum tunneling of magnetization (QTM) and/or quantum interference phenomena [3,4]. Furthermore SMMs and SCMs are suggested as potential candidates for quantum computation and magnetic storage devices exercising the need to control and manipulate spin and charge degrees of freedom in these systems [5, 6]. Molecular magnets are in competition with other viable candidates proposed as qubits, such as Josephson junction devices [7] and semiconductor quantum dots [8]. Although appreciable work and time has been spent in understanding and exploring the field of molecular magnetism, there are still a lot of questions and aspects unresolved from both physical and chemical perspectives. Hence scientists continue to explore the field in search of new and unique materials hoping to grasp the fundamental aspects of this field in depth and what it has to offer.

1.1.1 Single-molecule Magnets (SMM)

A SMM is comprised of a magnetic core of one or more exchange-coupled transition metal elements (Mn, Fe, Ni etc) with unpaired electrons [1,9,10]. The core is surrounded by organic moieties that protect the core from the environment hence minimizing the intermolecular interactions. The exchange-coupled core is what's responsible for the magnetic moment per molecule. Single-molecule magnets exhibit hysteresis of molecular origin below a certain blocking temperature. This particular relaxation phenomenon depends on the nature of the spin-orbit coupling of the electron spin and is finally shaped by the magnetic configurations likely from exchange interactions.

Among the special features of SMMs [11-17] is metastability, which manifests itself below the blocking temperature T_B, which in turn leads to the observation of magnetic hysteresis of molecular origin and slow relaxation of magnetization. The metastability results from an energy barrier resulting from spin-orbit coupling and separating opposite spin projections along the easy magnetic axis. The uniaxial anisotropy barrier of a SMM is shown in Figure 1-1. At low temperatures the molecule of net spin S is represented by its ground state which is the lowest lying $m_s = \pm S$ levels. The height of the barrier Δ corresponds to the energy difference between the lowest level $m_s = +S$ and the top level $m_s = 0$. This is usually expressed as $\Delta = DS^2$ for integer spins. For half integer spins, the barrier height becomes $\Delta = D\,(S^2 - 1/4)$.

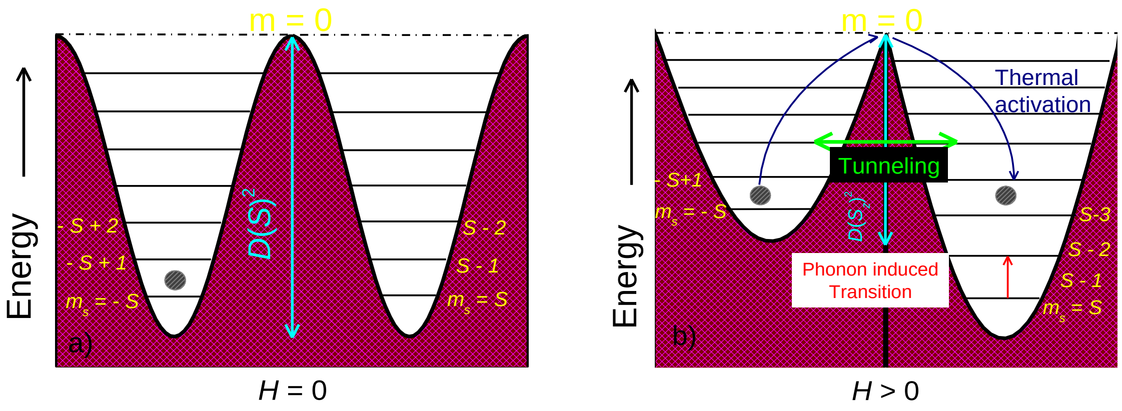

Figure 1-1: a) Schematic of the degenerate m_s *levels in zero magnetic field. Opposite spin projections are separated by the anisotropy barrier* DS^2*, where D is the zero-field splitting parameter. b) The application of magnetic field shifts the energy levels; at resonance magnetic quantum tunneling (MQT) is activated.*

In order for the system to overcome the barrier and relax to the opposite spin orientation it can follow two scenarios: a) thermal relaxation of magnetization, above the barrier or quantum tunneling across the barrier (Figure 1-1 (b)). The first dominates at higher temperature T and the relaxation time follows an exponential law (Arrhenius law) [18];

$$\tau = \tau_o \exp\left(\Delta / k_B T\right) \tag{1}$$

where, τ_0 is the attempt time, k_B is the Boltzmann's constant and Δ is the barrier height. As the temperature decreases the relaxation increases exponentially at low temperatures. Hence SMMs can be treated as permanent magnets. However at low temperatures the system can also relax via resonant quantum tunneling, whenever opposite spin projections coincide in energy (resonances). Its signature appears in the hysteresis of the molecule as periodic field steps where the magnetization drops abruptly. It is a purely quantum mechanical process and is temperature independent as long as the only involved state is the ground state, which occurs at the lowest temperatures. At intermediate temperatures tunneling occurs through excited spin levels, a process known as thermally assisted QTM (see Figure 1-1 (b)).

The recipe for a perfect SMM includes the following ingredients; 1) A large spin ground state. 2) Large negative uniaxial magnetic anisotropy; 3) Monodispersity: Single crystals comprised of identical molecules: 4) Existence of a set of well defined discrete magnetic states. SMMs have the ability to behave as tiny magnets and hence are considered very desirable materials for the fabrication of small magnetic devices in a controlled fashion, with unprecedented information storage capabilities. From the insight on very interesting phenomena associated to SMMs [19, 20], these materials are seen as potential candidates for qubits in quantum computing and information processes. In addition, SMMs have been also reported for having other applications: magnetic cooling or THz sources [1,5,6] are among the possibilities.

The magnetic properties of SMM can be described using the giant spin Hamiltonian approach (known as the giant spin approximation GSA) which includes the effect of an external magnetic field applied along the easy axis and the crystal field effects as shown in equation 2.

$$H = DS_z^2 + g\,\mu_B B_z S_z + H_A + H_{int} \tag{2}$$

Where S is the net spin of the molecule, D is the zero field splitting parameter (ZFS) as it removes the degeneracy of the S multiplet due to spin orbit interactions. The second term in the Hamiltonian is the Zeeman term. The third term corresponds to transverse anisotropies and the last term represents the various inter-molecular interactions such as dipolar, exchange [21].

The very first and the most studied SMM is $[Mn_{12}O_{12}(CH_3\text{-}COO)_{16}(H_2O)_4].4H_2O.2CH_3COOH$, commonly known as Mn_{12}-Acetate. The compound was first synthesized in 1980 but it took scientist years to understand the interesting characteristics associated with it [22-25]. Mn_{12}-Acetate, with a net spin of 10, is still among the SMMs with the highest temperature barrier T_B, of about 62K. It was in this molecule where the characteristic stepped curves in the hysteresis were first observed. Chemists have been studying in detail other Mn-based SMMs to achieve higher barrier temperatures and relaxation times. This dissertation is one such attempt to understand the quantum mechanical fundamentals of such systems and specifically of Mn-based systems.

1.1.2 Single-chain Magnets (SCM)

As discussed earlier, magnetic molecules are more inclined to exist as low dimensional clusters. Just as organic ligands lead to SMM, they can also lead to one-dimensional (1D) magnetic structures, exhibiting slow relaxation of magnetization as predicted by Glauber in 1963 [26]. The idea was first experimentally realized in 2001 by Gatteschi *et al.* [27] when they observed magnetic hysteresis of molecular origin and superparamagnetic behavior in $\{Co(hfac)_2[NIT(C_6H_4p\text{-}OMe)]\}$, where hfac is hexafluoroacetylacetonate,. These systems, like SMMs, soon became possible candidates for spin based information storage and by analogy to SMM were named as single-chain magnets (SCMs).

SCMs are one-dimensional isolated molecular structures comprised of magnetic ions linked together via bridging ligands. The SCM materials are magnetically isolated chains, with the ability to freeze their magnetization in the absence of an external magnetic field [28-30]. The systems are then considered as permanent magnets at low enough temperatures, because of the slow relaxation of magnetization. Ideal ID systems exhibit strong long-range magnetic order only at the critical temperature T_c = 0 K [21,30]. However real systems that host very weak residual inter-chain interactions like exchange coupling and/or dipolar interactions, along with intra-chain correlations arising, may give rise to magnetic ordering at $T_c > 0$. The inability of 1D systems to order at finite temperature does not hamper the existence of a large energy barrier, a consequence of strong coupling between the individual spin units within a chain and a large Ising like anisotropy, resulting in long relaxation times. Magnetic correlations play a vital role in understanding the magnetic response of 1D system especially at low temperatures. Generally the chains are classified using the following models: 1) Ising spins; the magnetic moment is restricted to point parallel to a certain direction, identified with two opposite states (up and down). In this limit the spins tend to have infinite uni-axial magnetic anisotropy and provided exchange interactions between first neighbors, the system is found to exhibit correlation lengths towards the higher end even at relatively higher temperatures, hence providing an opportunity to observe large barriers and relaxation times. 2) Heisenberg spins; magnetic moments are completely free to point in any direction, hence with a large enough spin ($S >> 1$), spin operators behave as classical vectors [31].

Although the field of exploring new and improved ID systems is rapidly developing [32] and many new SCMs have been introduced, it is still very hard to comply with the stringent requirements to observe slow relaxation of magnetism in these 1D systems [4]. The most important is the ratio of the intra-chain interactions J and the inter-chain interactions J', one normally expects it to be high, 10^4 or more. Increasing the intra-chain interactions can theoretically result in high temperature SCMs, hence the 1D systems which are stacked by van der Waals interactions or weak hydrogen bonding are expected to have infinitesimal inter-chain interactions [29,33]. Furthermore the material must be designed to behave as a 1D Ising ferro- or ferrimagnet with a significant easy-axis magnetic anisotropy with significant isolation between chains. Although SMMs and SCMs both exhibit blocking of magnetization as a result of a large uni-axial magnetic anisotropy, the SCM possess a distinctive advantage over SMM in terms of the correlation energy, Δ_ξ. The correlation energy is an additional energy term to the relaxation barrier, emerging as a result of the intra-chain coupling that exists between the anisotropic spin units of a single-chain. Thus putting forward a large enough relaxation barrier to ensure a stabilized orientation of magnetic moments (hence freezing of the magnetization), against thermal and quantum fluctuations. These systems are generally represented by the following Hamiltonian:

$$H = D\sum_{i} S_{iz}^{2} - J\sum_{<ij>} S_i\,.S_j + Zeeman\ energy \qquad (3)$$

Where $\boldsymbol{S_i}$ is the spin operator, D is the single ion anisotropy of the spin unit and J is the exchange coupling between neighboring spins within a chain. The summations are over the length of the chain L. In real systems L is never infinity due to the naturally occurring defects in the crystal. The mean value of the length of the chain $<L>$ can induce certain behaviors in the system as explained by the correlation length ξ. It is a quantity that dictates the probability of two spins spaced by a certain distance having the same orientations. The system will behave as an infinite chain if $\xi \ll L$, while if $\xi \gg L$, the chains are regarded at a set of finite segments. Each segment is comprised of iso-oriented spins separated by the next segment by L / ξ domain wall, which is actually a separation between segments of different spin orientations [4,29].

In SMMs the ground multiplet is split to result in a double quantum well, where spins have to overcome the anisotropy barrier $\Delta = |D|S^2$ using energy generated only by the magnetic anisotropy of the system. Unlike SMMs, where the energy barrier corresponds to a flip of the total magnetic moment, in SCMs the relaxation follows the Glauber dynamics, in which the relaxation process is initiated by a single spin flip within the chain, and a subsequent motion of the domain walls. In an Ising systems, the barrier energy required to create a domain is $\Delta_\xi = 4|J|S^2$ as shown in Figure 1-2 (top left), after this first flip, the spins continue to flip with no cost of energy as now the nearest neighbors have opposite spins (Figure 1-2 bottom). The probability that each spin can flip independently depends on the environment and the temperature. Hence the magnetization dynamics of 1D system follow a thermally activated law, (Arrhenius law) i.e. with a unique characteristic relaxation time given as [4,29];

$$\tau = \tau_0 \exp (\Delta_\xi / k_B T) \tag{4}$$

τ_0 is a prefactor representing the flipping rate of an isolated spin in the absence of interactions. It is thus useful to create SCMs with significantly large intra-chain interactions to achieve large relaxation times as the height of the barrier depends on the strength of J. However the magnitude of the creation energy and the relaxation time varies when single-ion anisotropy is present, Eqn. 2. In the high anisotropy limit, i.e. $|D/J| > 4/3$ for a uniaxial system, at low temperatures the magnetic excitations in the system follow the Ising model, resulting in nucleation of sharp domain walls (~ 1 unit cell thick) with creation energy magnitude of $\Delta_\xi = 4|J|S^2$ as before. While systems with smaller anisotropies i.e. $|D| << |J|$ (the Heisenberg limit) tend to form wider domain walls and Δ_ξ becomes a function of D and J both ~ $4S^2\sqrt{|JD|}$ [34,35]. Also the modified relaxation time for spin inside a domain wall follow Arhenius law given by:

$$\tau(\mathrm{T}) = \tau_i \exp\,(\Delta_\mathrm{A} / k_B T) \tag{5}$$

where Δ_A is the barrier experienced by spin during flipping and is equal to DS^2 and the prefactor τ_i represents the behavior of a spin in contact with a thermal bath when there is no energy barrier.

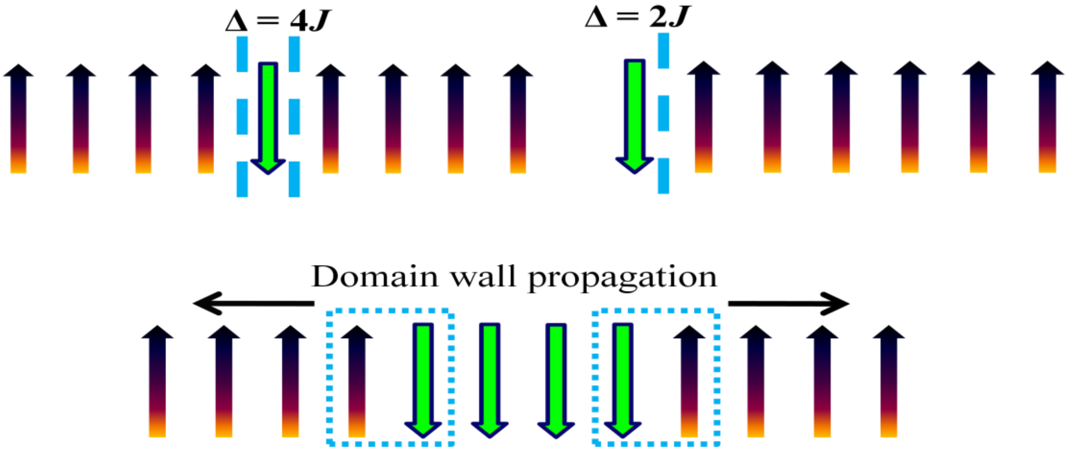

Figure 1-2: Top lef) Energy required to flip a spin in an infinite chain. Top right) Energy required to flip a spin in a finite chain, or near a defect. Bottom) once the domain wall is created it continues to move along the chain at no energy expense.

As mentioned above a one-dimensional Ising magnet must fulfill the exponential divergence requirement, however in real systems this process is always hampered by some small residual interaction between the chains J' (dipolar or exchange) hence triggering a cross-over from 1D to 3D magnetic dynamics in some cases, or by presence of defects in most cases. As mentioned above, a 1D system can behave as a chain comprised of smaller segments of length L, which depends not only on the correlation length ξ but on the concentration c of defects as well. In terms of lattice steps, this probability can be written as:

$$P_L = \mathrm{c}^2\,(1\text{-}c)^{\,L} \tag{6}$$

This behavior along with temperature poses significant effects on the magnetic dynamics of the system. In the low T regime, when ξ is much larger than L the spin flip occurs at a defect with an energy cost of breaking one bond of $2JS^2$ (Figure 1-2(top right)). At low temperatures, nucleation of spin reversal will always be initiated at the end of a chain. At high T, when ξ is significantly less than L, the reversal of spin direction is a random process, hence doubling the barrier energy $4J\,S^2$. Once the wall is created it propagates itself to the end and the propagation steps required for full reversal of magnetization is directly proportional to the length of the segment and hence the relaxation time [4,21].

1.2 Characterization techniques for molecular magnets

The vast interest in the field of molecular magnetism has been generated thanks to the diverse experimental techniques available that probe and highlight the various interesting characteristics associated to these materials. Among such is the understanding of the magnetic anisotropy of the spin centers, interactions among the spin centers, energy spectrum of the available spin states and more. There are different techniques available to answer these questions like SQUID (Superconducting Quantum Interference Device) magnetometry, torque magnetometry, ac susceptometry and neutron magnetic resonance [1,21, 36]. However, two techniques have shown to be particularly suited for the investigation of molecular magnets; a)

Hall-effect magnetometry, which allows investigation of slow relaxation of magnetization an hysteresis effects and; b) electron paramagnetic resonance (EPR), which allows the determination of the energy landscape of the complexes. These are indeed the two techniques employed in the studies presented in this thesis.

1.2.1 Low-temperature Hall-effect Magnetometry

The magnetic properties can be probed via Hall-effect Magnetometry. The Hall-effect magnetometer works on the principle of the Lorentz force. For our measurements micro-Hall effect sensors made up of AlGaAs/GaAs 2DEG (two dimentional electron gas) hetero-structures are used [37]. A typical measurement setup involves placing a single crystal near the Hall-sensor cross, such that a current of about 1-2 μA is applied through two opposite leads and the Hall voltage is measured (via a lock-in amplifier) through the other two leads of the cross, as shown in Figure 1-3(a). The sensor is then placed at the end of the sample holder of the cryostat. Once the cryostat is in the magnet, the system is cooled down with liquid helium and pumped to reach the desired temperatures.

In this work I present magnetic properties of different complexes studied using micro Hall-effect magnetometers fabricated in our lab at UCF. Our system works, with a 3D rotating superconducting magnet, which allows the application of magnetic fields in arbitrary directions, this tool is especially useful when locating the quantization axis of the crystal or investigating phenomena like QTM or Berry phase interference, which are highly dependent on the external field orientation. Furthermore the system is equipped to work with a ^{3}He cryostat that allows a variable temperature range down to 240 mK, and a dilution fridge refrigerator with the ability to go down to 30 mK, hence providing a wide range of temperatures to understand the thermal behavior of the magnetic hysteresis associated to molecular magnets. A typical measurement is shown in Figure 1-3(b), which includes hysteresis loops recorded on a single crystal of $[NEt_4]_3[Mn_5\text{-}(salox)_3O(N_3)_6Br_2]$ where Et is ethyl and saloxH_2 is salicylaldoxime [38].

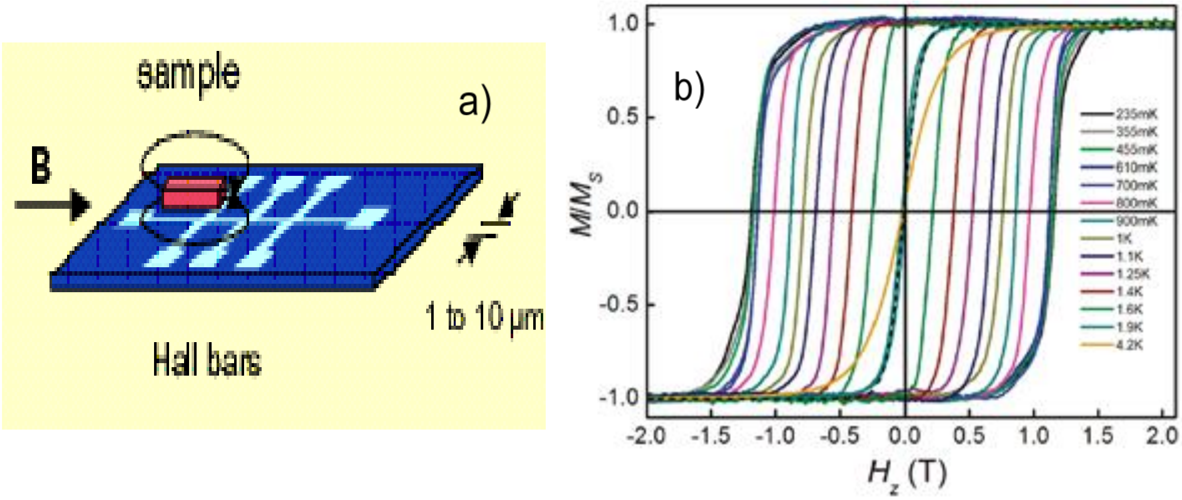

Figure 1-3: a) A typical micro Hall bar used for magnetic studies of molecular magnets. b) Hysteresis measurements for a single crystal of $Mn^{III}Mn^{II}$ *as a function of temperature at 0.2T/min. The magnetization is normalized by the saturation value* M_s.

We would like to point out that the labels of the *x* axis in all the figures showcasing the Hall-effect magnetometry measurements like the one shown in Figure 1-3 (b), are following standard literature labels for external magnetic field i.e. *H*. The experimental magnetic field mentioned through out the thesis is actually the magnetic induction *B* expressed in Tesla.

1.2.2 Electron Paramagnetic Resonance (EPR)

Electron paramagnetic resonance (EPR) is one of the basic techniques to probe and study chemical species with unpaired electrons, like inorganic complexes with one or more transition metal ions [39-41]. In paramagnetic solids with unpaired electrons, transitions can be induced between different states of a spin multiplet by introducing electromagnetic irradiation, usually in the microwave range. The result is absorption spectra known as EPR. The EPR absorptions occur when the energy spacing $\Delta\varepsilon$ between two spin states coincide with the energy of the microwave field,

$$\Delta\varepsilon = hf \tag{7}$$

where h is the Plancks's constant and f is the microwave frequency. Considering a system of total spin S, in the presence of an external magnetic field H, the interaction of the electron spin with the applied field will split the energy levels into $2S+1$ non-degenerate states. In addition, at H = 0, the intrinsic anisotropy can produce the same effect (ZFS). Figure 1-4(a) shows a typical energy diagram of a spin $S = 2$ system with a reasonable zero-field splitting. The separation between the states is proportional to the magnetic field (Zeeman energy) and the ZFS parameters give insight into the anisotropy of the complex. In a continuous-wave EPR experiment, either the frequency of the microwave is swept and the magnetic field is fixed or vice versa. In the EPR measurements described in this thesis the later technique is employed. The cavity is irradiated with microwaves of a fixed frequency and the transmission intensity through the sample is recorded as a function of the external applied magnetic field. The intensity of an EPR transition provides an insight into the population density of the states as it is proportional to the difference between the thermo-population of the initial and final states of molecules. According to the magnetic dipole selection rule for EPR the allowed transitions should obey $\Delta S = 0$ and $\Delta m_s = \pm 1$, i.e. only transitions within the same spin multiplet are allowed; here m_s is the magnetic quantum number for the spin projection onto the quantization axis. If the system is coupled properly, a spectrum would be observed with dips in the transmission indicating transitions between different energy states.

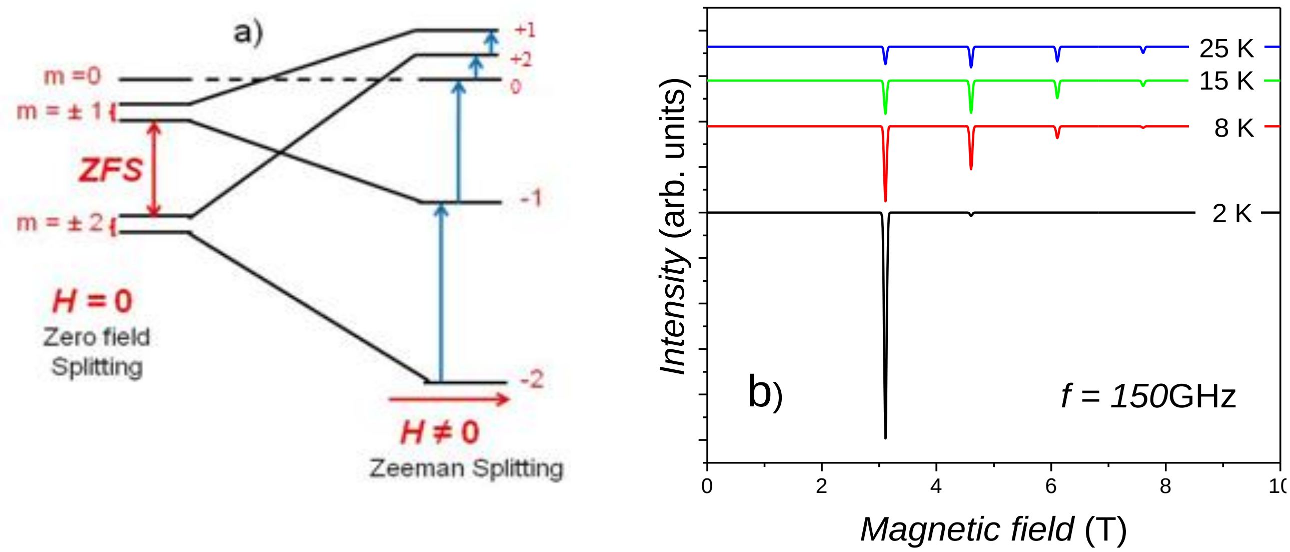

Figure 1-4: a) Energy level diagram of spin S = 2 system as a function of the applied magnetic field. The blue arrows indicate the possible transitions between the energy levels. b) Simulated spectrum of a spin S = 2 system at 150 GHz. The intensity of the four transitions is shown at different temperatures.

Figure 1-4(b) shows a simulated EPR spectra of a spin $S = 2$ at $f = 150$ GHz. For a spin $S = 2$ system following the selection rules four transitions are expected between energy states, whose energy difference $\Delta\varepsilon$ equals Planck's constant h times the incident microwave frequency f. Each transition denotes the transition from m_s *to* $m_s - 1$. In a typical EPR experiment, the positions of the transition peaks are studied as functions of frequency, temperature and magnetic field orientation. In order to obtain information on the ZFS parameters the EPR spectra is collected at different frequencies and a 2D frequency versus resonant field plot is then generated. The intercepts of the resonance branches are related to ZFS parameters and the slope of the branch is proportional to the g - values. The magnitude of transition intensity at various temperatures separates the ground state transitions from the excited state transitions. At lower temperature only ground state is expected to be heavily populated and the intensity is expected to decrease with elevating temperature, as the higher states start populating (Figure 1-4(b)).

The EPR experiments discussed in the following chapters were performed at the Electron Magnetic Resonance facility at the National High Magnetic Field Laboratory (NHMFL) in Tallahassee. The single crystal EPR measurements were performed using a cavity perturbation technique in combination with a broadband millimeter-wave vector network analyzer (MVNA) [42,43] in the laboratory of Professor Stephen Hill. Cavity perturbation EPR experiments were carried out on a 6.8 T superconducting magnet equipped with a calibrated temperature sensor and a cylindrical resonant cavity of high quality factor. A millimeter-wave network analyzer (MVNA) was employed to obtain the transmission spectra, allowing measurements over a wide range of frequencies. The MVNA acts as a tunable microwave source as well as a phase sensitive detector. The system is equipped to work at temperatures down to 2K. Some of the single crystal continuous-wave and pulsed EPR measurements [Chapter 2] were done using the Heterodyne Spectrometer with a 12.5 T superconducting magnet in Dr. Johan van Tol's laboratory. The sample was mounted on a single axis goniometer for both the continuous-wave and the pulse EPR studies [44, 45]. The EPR measurements on polycrystalline samples were performed in Dr. Andrzej Ozarowski's laboratory [46], with the use of a commercial Bruker spectrometer. Furthermore, the plots of the EPR experiments are expressed in terms of the standard literature labels i.e. the energy of the transitions is expressed in GHz to relate to the experimental frequencies, furthermore the external magnetic field s identified as H, instead of the magnetic induction B.

CHAPTER 2 UNDERSTANDING THE ROLE OF ANISOTROPY AND EXCHANGE IN LOW-NUCLEARITY MAGNETIC SYSTEMS

In contrast to larger clusters, the inherent simplicity of low-nuclearity molecules and the fact that the exchange can be more easily modulated makes them very attractive. In this chapter two Mn-based systems are discussed, a weak exchanged coupled Mn(II) dimer and a significantly anisotropic Mn(IV) monomer. Extensive EPR experiments are performed on each molecule to understand the role of exchange interaction (in the former) and magneto-anisotropy associated to these systems. EPR experiments on the Mn(II) dimer were performed in Hill's laboratory at NHMFL, whereas the DC magnetometry studies were performed at UCF. For the Mn(IV) monomer continuous-wave and pulsed single crystal EPR experiments were conducted at van Tol's laboratory, while powder EPR measurements were performed in Ozarowski's laboratory, also at NHMFL.

2.1 Introduction

2.1.1 Exchange interactions in molecular magnets

Exchange interactions are crucial in molecular magnetism as they dictate the spin ground state of interacting ions resulting from the type of interactions (FM or AF) between them. The manipulation of the magnitude and sign of the exchange interaction J can lead to very interesting results, as will be shown in later chapters. The coupling between the ions can be tailored by adjusting the structural bond lengths, bond angles and/or by intervening with the right non-magnetic ligands [47-49]. In exchange-coupled systems the number of spin states in the energy diagram depends on the number of ions N present in the magnetic core of the molecular magnet, i.e. $(2S + 1)^N$. Furthermore, the interplay between the exchange interactions J between the ions that constitute the magnetic core and the single-ion magneto-anisotropy d dictates the observed magnetic behavior of the molecular magnet. Correspondingly, understanding the strength of exchange couplings in the magnetic core becomes crucial for unveiling the interesting phenomena associated to single-molecule or single-chain magnets [21,48,50].

The behavior and the respective analysis of the magnetic properties of molecular magnets can be placed in two categories based on the strength of the exchange interactions in the magnetic core. For large J, the net spin of the system is treated as a rigid giant spin, which can be taken as an exact quantum number. In this case the energy landscape follows the Hamiltonian provided in equation 2 i.e. the GSA Hamiltonian. However, for small J or $J \approx D$, the giant spin scheme fails to explain the experimental data properly. Furthermore it becomes quite difficult to interpret the behavior of a weakly exchanged coupled system, since low lying excited spin levels start playing a significant role, thus leaving behind a not well defined ground state. Since weakly interacting molecules cannot be described by the giant spin Hamiltonian, a more appropriate scheme to solve these kinds of systems involves assigning an anisotropy term to individual ions in the magnetic core, along with exchange interactions between the constituent ions. This multi spin system is illustrated by the following Hamiltonian [51];

$$H = \sum_i (d_i s_{iz}^2 + \mu_B B.g.s_i) + \sum_{<ij>} J s_i.s_j \qquad (8)$$

Where d_i is the second order axial anisotropy parameter associated to individual ions in the complex. The third term in the Hamiltonian provides the sign and strength J of the Heisenberg interaction between the ions. Depending on the complex under study it can be either isotropic or anisotropic. The last term in the Hamiltonian is the Zeeman energy associated with the coupling of each spin with the applied magnetic field.

This model can be put to work in slightly complicated systems, where SMMs couple to form more complicated and fascinating species like dimers, chains, etc [52]. One such example is a dimer of two Mn(IV) ions [53] where each unit in the dimer is composed of exchanged coupled SMMs. Understanding and control of these parameters can lead to the observation of interesting QTM effects [54,55]. In general, this model is quite successful for small molecules, with a low number of ions in the magnetic core, but it becomes computationally difficult for complex (high nuclearity) magnetic clusters.

In this chapter two low-nuclearity Mn-based molecules are discussed. Manganese has been an active ingredient in many chemical and biological processes and lately a strong interest in shown in manganese-based materials for information storage and spintronics [56]. Flexible chemistry of manganese can result in the synthesis of fairly simple yet rich in count polynuclear crystals i.e. molecular clusters containing a few strongly interacting spins [57], resulting in large ground-state spin S values, which is important for the synthesis of new SMMs. SMMs of wide nuclearity provide a wide range of spin values, from $S = 3$ to 83/2, and are perfect entities to study many interesting effects, like QTM, exchange bias and/or quantum phase interference.

Mn(IV) has been part of the SMM community from the very beginning and has been used as building block for many zero and one-dimensional systems [16,22,23,21]. A lot of interest lies particularly in studying Mn(IV) and its potential in chemical and biological processes[56]. One such significance lies in the manganese-catalyzed oxidation to synthesize catalysts using stable, cheap and readily available oxidants. The catalyst life time is directly dependent on the stability of the respective manganese complexes; hence to have strong catalysts it is crucial to design stable manganese complexes. Although multinuclear manganese complexes have been reported to be stable enough in solution, experimental results are significantly lagging behind for mononuclear Mn(IV) stable compounds [58]. In this thesis, a water stable monomeric Mn(IV) is presented, an insight into its energy landscape and magnetic nature is explained in the main text.

2.2 High-field high-frequency electron paramagnetic resonance (EPR) study of an anisotropic mononuclear Mn(IV) molecule

The motivation of the current study is to explore the anisotropy of high valent mononuclear Mn(IV) as well as the orientations of the magneto-anisotropy axis with respect to the crystal. More specifically we are interested in rationalizing the ZFS parameters associated with the individual Mn(IV) ions. In this work we study a water stable Mn(IV) complex; it's a monomeric specie with chemical formula $C_{20}HClCoMnN_4O_6$ that crystallizes in a *P21/c* space group in which the manganese ion has a distorted-octahedral geometry with four oxygen and two nitrogen atoms. The asymmetric unit in this case is the individual monomer and there are 4 monomers per unit cell as shown in Figure 2-1. The nature of the EPR spectrum of the Mn(IV) specie can be explained in terms of the giant-spin axial (*D*) and rhombic (*E*) zero-field splitting parameters and their response to the energy (*hf*) delivered to the sample from the spectrometer [59].

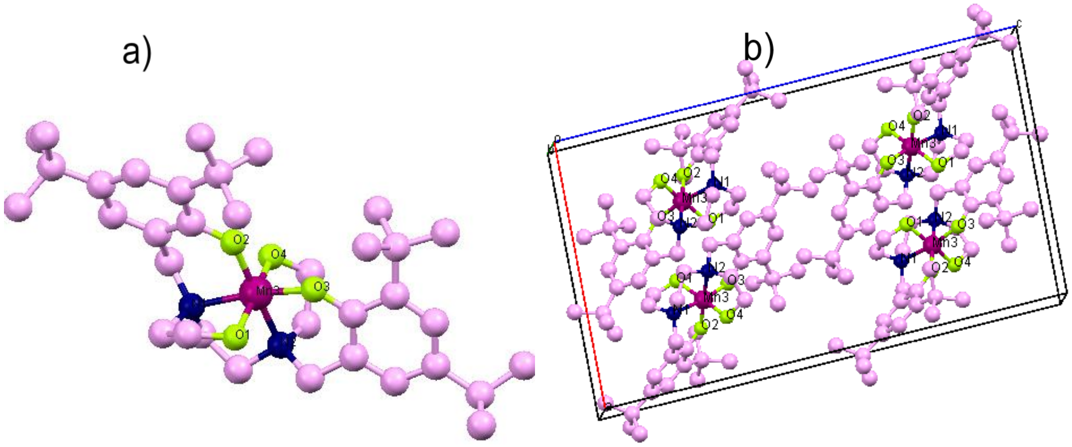

Figure 2-1: Left) Asymmetric unit of the Mn(IV) monomer complex. Right) a packed unit cell of the complex houses four asymmetric units. In both cases hydrogen are omitted for clarity.

For a Mn(IV) system with S = 3/2, three transitions $|S\ ,\ m_S> \rightarrow |S\ ,\ m_S +1>$ are expected. These transitions should exist for each orientation of the magnetic field along any of the principal anisotropy axes associated with D. The crystals used for the experiments are long thin black rectangles, with a wider flat side. For the measurements the longer side of the crystal is used as reference. The details of the crystallographic structure are provided in Table 2-1.

Table 2-1: X-ray Crystallographic data for single crystal of the Mn(IV) complex.

Crystal space group	P 2_1/c
Unit cell dimensions; Length (Å)	a =14.0488(4), b = 9.9929(3), c = 24.7991(7)
Angles	α = 90.00, β = 93.193(2), γ = 90.00
Asymmetric unit per unit cell	4
Volume ($Å^3$)	3476.1
Z, Z'	6, 0

2.2.1 Polycrystalline EPR measurements

For the powder EPR experiment crystals were grounded finely in a powder ~ 130mg and then mixed with KBr to make a pellet, which is then wrapped in Teflon and placed in the EPR probe for measurements. The powder measurements were done over a broad frequency and temperature range ($f = 50 – 420$ GHz and $T = 2 – 35$ K). Figure 2-2(a) shows the powder EPR spectra observed at 208GHz at the lowest available temperature 2.5K (top blue line). S_{21} is the transmission parameter. A weak signal appears at $g = 2$ (7.41T) with strong features at higher and lower fields. In order to understand and identify the ground state transitions, the powder EPR spectrum was simulated by a complete diagonalization of the spin Hamiltonian (bottom red data) [21]:

$$H = D\left[S_z^2 - \frac{1}{3}S(S+1)\right] + E\left(S_x^2 - S_y^2\right) + \mu_B g.B.S \qquad (9)$$

where D and E are factors parameterizing the uniaxial and the rhombic ZFS parameter. The positions of the two strongest peaks in the spectrum, i.e. $H_1 = 5.83$ T and $H_2 = 11.2$ T, can be well explained using $S = 3/2$, $D = +18$ kG (~1.7 cm^{-1}), $E = +30$ G (0.0023 cm^{-1}) and anisotropic g's, $g_x = 2$, $g_y = 1.945$ and $g_z = 1.974$. Figure 2-2(b) shows the Zeeman energy level diagram of a spin 3/2 system with a positive D. The arrows indicate transitions between consecutive m_s levels within the $S = 3/2$ multiplet at the frequency of the experiment (208 GHz) and with the field applied parallel to the z-axis. At high frequency (high field), the ground state transition corresponds to $m_s = (-3/2 \rightarrow -1/2)_{//}$, which justifies the EPR absorption peak observed at the highest field ($H_2 = 11.2$ T) for molecules feeling the field applied along the anisotropy axis. The other main EPR resonance observed at low field ($H_1 = 5.83$ T) corresponds to a transition between the two same spin projection levels, $m_s = (-3/2 \rightarrow -1/2)_{\perp}$, for the molecules feeling the magnetic field perpendicular to the z-axis. Furthermore, the small intensity peaks around $H = 7.0$ - 7.5 T in the spectra can also be identified in the simulation to come from transitions between excited states (e.g. $m_s = -1/2 \rightarrow +1/2$). The good agreement between the simulated and measured spectrum allows an accurate determination of the zero-field-splitting (ZFS) parameters in the spin Hamiltonian governing this system.

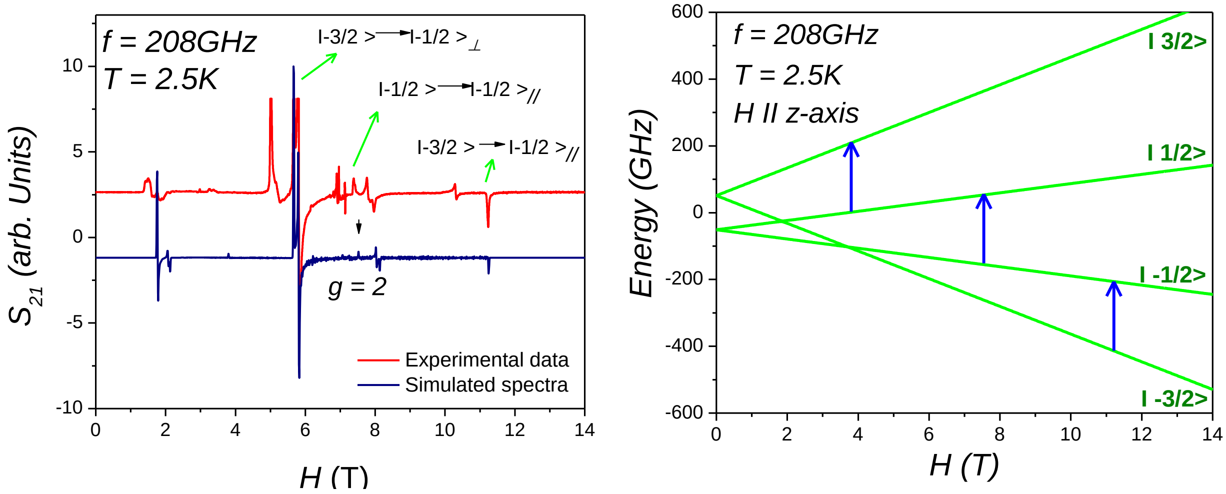

Figure 2-2: Powder EPR spectrum of the Mn(IV) monomer observed at 208 GHz at 2.5K. Both experimental (top red data) and simulated (bottom blue line) data are shown. Inset) Zeeman splitting of the spin levels with the EPR transitions (arrows) expected at 208 GHz with the field applied along the z -axis.

The sign of D is further explored from the temperature dependence of the EPR spectra. Figure 2-3 shows 208 GHz powder spectra at temperatures varying from 2.5 K up to 35 K. The intensity of the high field ($H_2 = 11.2$ T) EPR peak decreases in increasing temperature, indicating a decrease in the ground state population at high temperatures, until it completely disappears at temperatures over 25 K. Since this transition appears at the highest field it can only be explained with a positive *D* parameter and, as stated above, corresponds to the $m_s = (-3/2 \rightarrow -1/2)_{//}$ transition. Note that for a negative *D*, the ground state transition would be the first to appear at the lowest magnetic field (around 4 T with the current ZFS parameters).

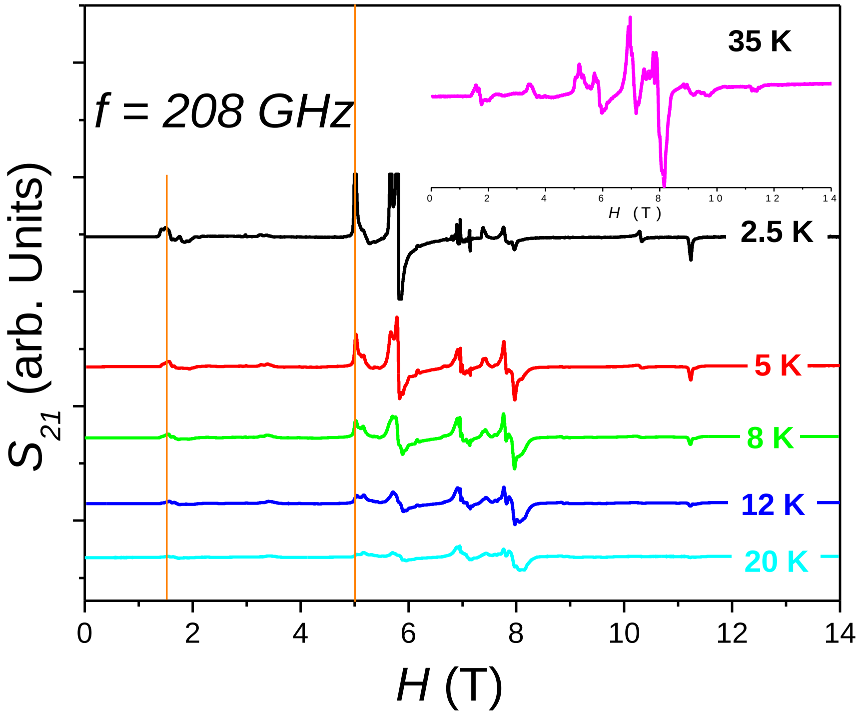

Figure 2-3: Powder EPR spectra of Mn(IV) monomer observed as a function of temperature at high frequency 208 GHz. The top right part shows new resonances appearing at 35 K at low fields.

A detailed literature search found similar studies on Mn(IV) monomers isolated or as impurities in aluminum and magnesium oxide with a somewhat small ZFS parameters, on average $|D|$ ~ 0.3cm^{-1} [60-62]. This indicates that the value of the ZFS parameter in this compound (D = 1.7 cm^{-1}) is towards the higher end of the D range. It should be noted the above parameters are unable to simulate the peaks at 5.02T, it is a response of the impurity and has nothing to do with the sample itself as can be seen in the single crystal studies where no suck peak is observed. Whereas peaks appearing at <2T are attributed to another specie present in the unit cell. EPR spectra on the powder samples was also recorded at different frequencies (ca. 50 to 416 GHz) at the lowest temperature allowed by the experimental setup (T = 2.5K). A two-dimensional map of frequency versus field positions of the corresponding EPR absorptions is shown in Figure 2-4 (open squares). The solid lines are generated using the spin Hamiltonian parameters close to those extracted from the powder measurements. Red solid curves indicate transitions expected when the field is applied parallel to the z-axis, whereas green and blue dashed curves represent the perpendicular components. The slight difference between the latter two is due to the presence of the transverse anisotropy term E. One immediately observes a single zero-field energy gap (i.e. ZFS) between the two Kramer's doublets in the S = 3/2 spin state ($m_s = \pm 1/2$ and $m_s = \pm 3/2$). This gap is approximately equal to 102 GHz, which is equal to 3.4 cm^{-1}, thus making the axial ZFS parameter approximately $|D|$ = 1.7 cm^{-1}. As mentioned above, the rhombicity factor is very small E/D ~ 0.0013, as can be seen in Figure 2-4 in the slight doubling of the perpendicular components (dashed curves). The graph also depicts off axis transitions (marked by arrows). The off-axial resonances often appear in spectra of spin states with S > 1/2.

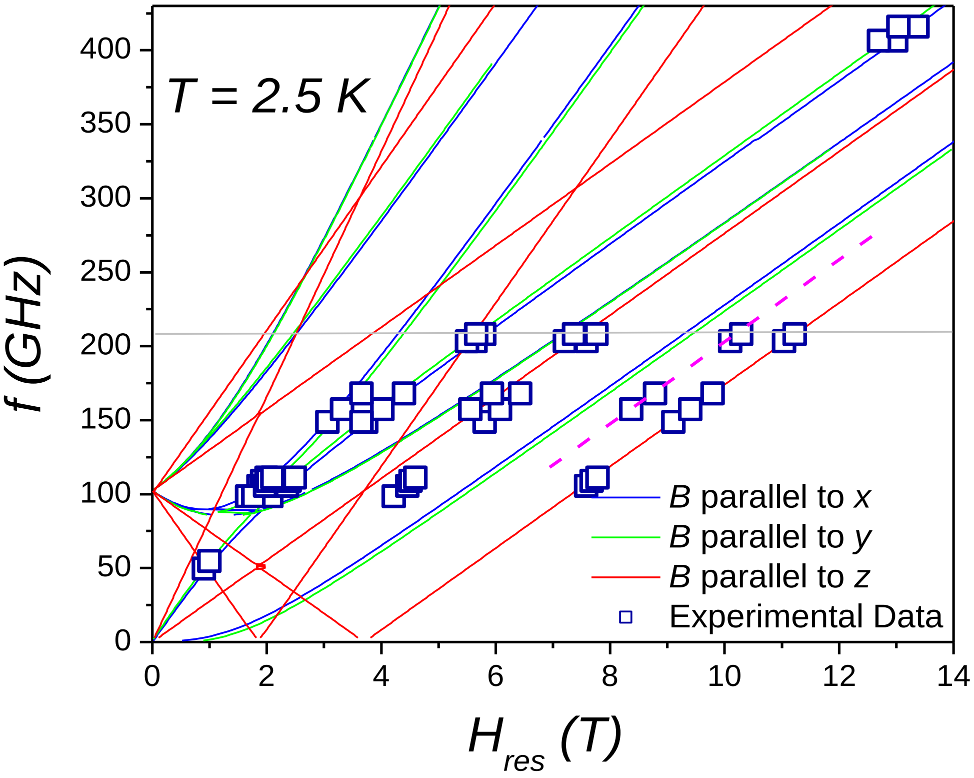

Figure 2-4: Two-dimensional map of frequency versus peak field positions observed in the powder EPR spectra of Mn(IV) monomer at 2.5 K. The squares are experimental points; the lines indicate various components (x(blue), y(green) and z(red)) of the transitions calculated using the spin Hamiltonian parameters mentioned above. The horizontal gray line indicates the frequency and field positions of the spectra observed in Figure 2-2 (a). The pink dashed line is the off axis transition.

2.2.2 Single Crystal continuous-wave and pulsed EPR measurements

High-field EPR experiments have also been performed on a single crystal of this compound. The sample was mounted on a single axis goniometer for both the continuous-wave and the pulsed EPR study. The sample was mounted with the rotation axis parallel and perpendicular to the long axis of the crystal. The studies reveals spectra containing sharp resonances that can be directly associated with spin 3/2 system, hence allowing precise comparisons with the theoretical simulations. A detailed study of the temperature dependence (5 – 60 K) and the angular modulation of the EPR spectra for this sample have been conducted at two frequencies, 240 and 336 GHz. As it will be shown below, the angle dependent high-field EPR study of the ground state transition within the S = 3/2 multiplet reveals an axial symmetry with an easy anisotropy plane perpendicular to the z-axis (hard axis).

The inset of Figure 2-5 shows the EPR spectrum obtained at 239GHz at 5 K with the field along the hard anisotropy axis (*z*-axis). Three strong absorption peaks are observed at ~ 6.9 T, ~ 8.5 T and ~ 10 T, with the lowest field peak displaying the highest intensity, as expected from a positive *D* system for this orientation of the magnetic field. The temperature dependence of the peaks and similar behavior observed at other frequencies (discussed later in the text) confirms this deduction. The complex structure dictates octahedral coordination; a reasonable assumption is to expect almost axial anisotropy, which in this case is of an easy plane type. The main part of Figure 2-5 shows the Zeeman energy levels of a spin S = 3/2 system as a function of the field applied along the hard anisotropy axis (*z*-axis) calculated by direct diagonalization of the Hamiltonian using the same parameters used to fit the powder spectra at low temperature. The arrows indicate the three main expected transitions for 239 GHz, which correspond to the three peaks observed in the experiment (see inset to Figure 2-5). The same behavior is observed at 366GHz (not shown here), with the strongest low field peak appearing at ~10.4T.

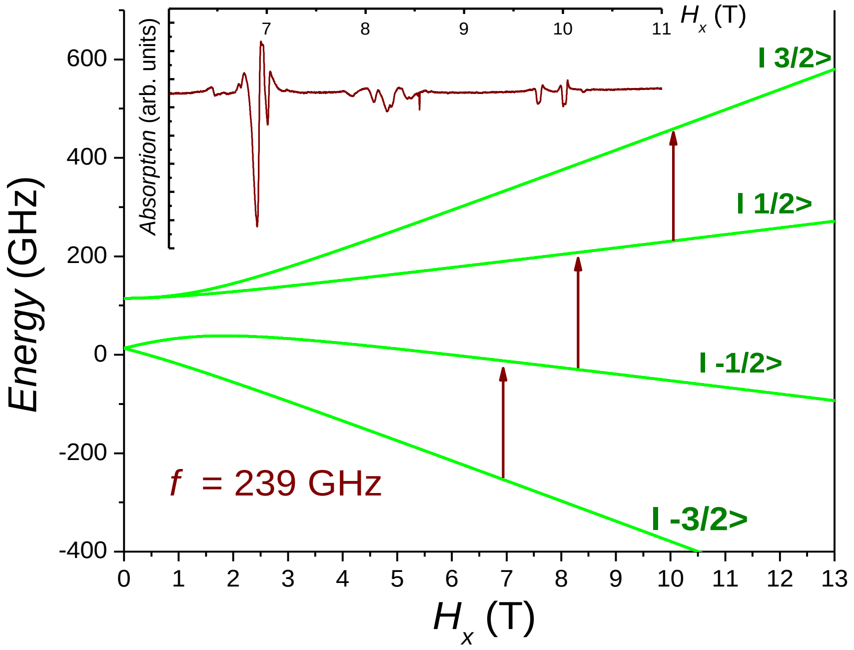

Figure 2-5: Zeeman energy diagram of the spin levels of Mn(IV) with the field applied along the hard anisotropy axis (z-axis) of the molecule. The expected transitions induced by microwaves of frequency 239 GHz are indicated by arrows. Inset) Single crystal absorption spectrum observed at 239 GHz and 5K, with the external magnetic field applied along the hard anisotropy axis.

In order to confirm that the transition associated to the peak observed at 6.9 T for 239 GHz and 10.4 T for 336 GHz is actually a ground state transition, the spectrum was recorded over a wide range of temperatures for both set of frequencies. With the magnetic field applied along the crystal's long axis it is very clear from Figure 2-6 that the peak at 10.4 T in case of 336 GHz is definitely a ground state to first excited state transition as the intensity of the peak significantly increased with the decrease in temperature. Very small features are observed at higher fields but the intensities are so small compared to the main peak that it is hardly worth it to resolve them.

The same behavior was observed at 239 GHz. So here onwards the focus is on the high intensity low field ground transition.

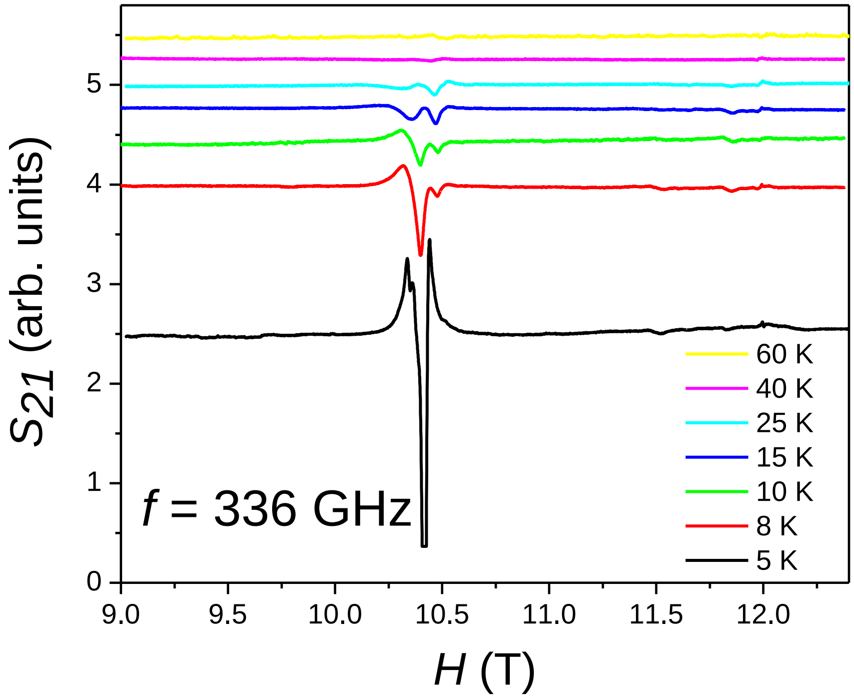

Figure 2-6: Temperature dependence of the low field main peak i.e. ground state ms = -3/2 to -1/2 transition of Mn(IV) monomer indicated in figure 2-5.

In order to establish the direction of the anisotropy axes with respect to the crystallographic axes of the sample, EPR spectra have been recorded at different orientations of the magnetic field with respect to the crystal faces. Figure 2-7 shows the angular dependence of the ground EPR transition at 239.2 GHz (circles) and 336 GHz (stars) with the magnetic field rotated in two orthogonal planes related to the crystal faces as depicted in the central sketch of Figure 2-7. The magnetic field is rotated in two different planes of the crystal. The crystal is oriented such that the *y*-axis lies along the longest crystal axis, and the *x*-axis is perpendicular to the flattest crystal face. The first experiment is performed with the external magnetic field rotated at an angle θ within the *zx*-plane ($\phi = 0$, red plane). Both frequencies (239 GHz and 336 GHz, solid circles and stars, respectively) show minima at $\theta = \pm 90$ degrees, with a maximum in the peak field position when the field is applied along the z-axis ($\theta = 0$), which corresponds to the hard anisotropy axis. The strong anisotropic nature of this molecule is evident for the strong modulation of the main EPR absorption, which shifts by almost 5 T between the easy plane (6.8 T for 239 GHz) and the hard anisotropy plane (11.5 T). The second rotation is done by rotating the field by an angle ϕ within the *xy*-plane ($\theta = 90^{\circ}$, blue plane). Both frequencies (239 GHz and 336 GHz, open circles and stars, respectively) show a small modulation of the main EPR absorption peak ($\Delta H \sim 0.5$ T), indicative of being rotating the magnetic field almost within the easy anisotropy plane of the molecules. The data can be effectively fitted using the spin Hamiltonian of Eqn. (2) with the ZFS parameters obtained from the powder measurements. To take into account for the possible misalignment between the molecular anisotropy axes and the crystal faces, the orientation of the main axis of the ZFS tensor is left to be determined by the Euler angles α, β and γ(=0), as indicated in the central sketch of Figure 2-7. The best fit was achieved for $\alpha = 18^{\circ}$ and $\beta = 0$ (solid and dashed lines in Figure 2-7 (a) and (b)). One must keep in mind that the small deviations between experimental and calculated results is a consequence of two factors: First, the parameters used in the fitting are close to those extracted from the powder measurements with isotropic $g = 1.974$ and are not fine-tuned to fit the single-crystal data. Second, there is always an uncertainty in the alignment of the crystal with respect to the main axes of the magnet used to obtain the spectra. With this in mind, one can still conclude that the Mn(IV) presents an easy-plane type anisotropy with the axial symmetry *z*-axis (hard anisotropy axis) aligned within 18 degrees from the flattest face of the crystal, as indicated in Figure 2-7 (a) and (b). The two-fold angular modulation of the EPR spectra is indicative of strong axial magnetic anisotropy ~ 5 T, which is substantially large in Mn(IV) systems.

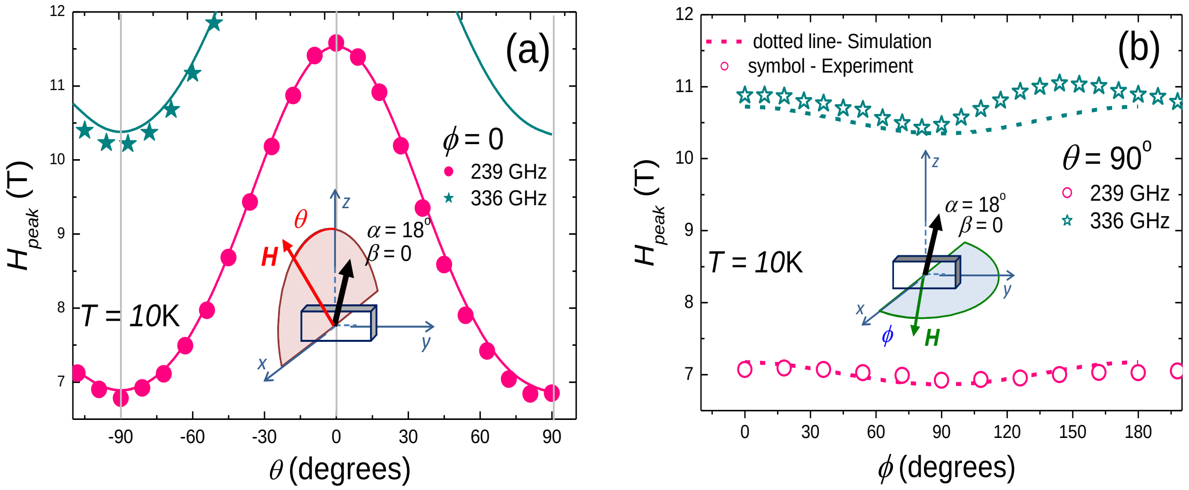

Figure 2-7: a) Angle dependence of the ground state transition of the Mn(IV) complex with field applied perpendicular to the long axis in the xz plane. b) Angle dependence of the ground state transition with rotation observed in the xy plane with magnetic field along the crystal's physical long axis. The angular behavior is observed at 10 K for a frequency of 336 GHz. The symbols (solid and hollow) indicate experimental data, whereas the solid and dotted lines are obtained from simulations.

Pulsed EPR spectroscopy [63] was also employed to determine the characteristic spin-spin relaxation time of this system. Spin echo measurements and the consequent echo decay were studied via high-field pulsed EPR as a function of temperature and magnetic field orientations at 240 GHz. The experiments were performed using a Hahn echo sequence ($\pi/2 - \tau - \pi - \tau -$ echo) where the delay τ between pulses was varied. The optimum results, i.e. strong echo signals, were obtained by adjusting the pulse lengths of both the π and π /2 pulses. The optimal $\pi/2$ pulses employed for the experiments were 1000 ns and 1350 ns in length, each with a delay of 140nsec. Echo signals were observed at 1.47 K for the m_s = -3/2 to -1/2 transition as shown in inset of Figure 2-8.

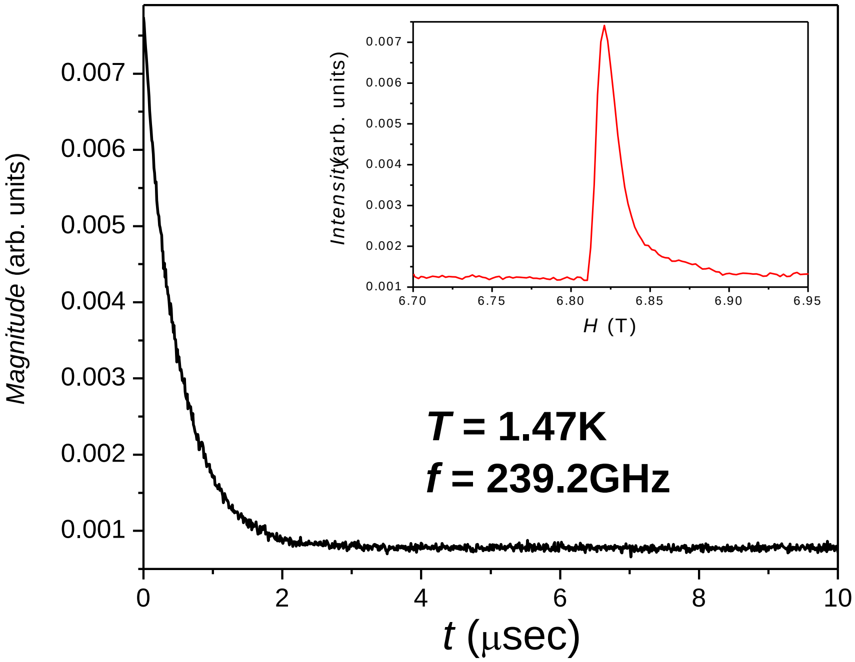

Figure 2-8: Time decay of the spin echo amplitude (T_2 relaxation time) observed for the Mn(IV) complex with the magnetic field applied along the x-axis. The inset shows the spin echo signal observed at 7.08T, with the applied field along the length of the crystal.

The echo signal observed in Figure 2-8 (inset) is studied as a function of magnetic field orientation and temperature. With the field applied initially along the length of the crystal (*y*-axis) and then rotated in the *xz*- plane, a decrease in the strength of the echo signal was observed. For the same orientations the T_2 experiment was also conducted with the exponential decay as shown in main part of Figure 2-8 with the field along *x*-axis. The decay is then fit using $T_c \alpha$ exp $(-t/T_2)$, where t is the time of the experimental response in μsec, on average the exponential decay is characterized with a T_2 of about 500 ns.

In summary, we studied a water stable Mn(IV) mononuclear compound. Detailed powder and single crystal multi-frequency, high field EPR spectroscopy measurements show that the Mn(IV) presents a $S = 3/2$ ground spin state with a strong axial anisotropy of the easy-plane type ~ 1.7 cm^{-1}. In addition, spin echo experiments reveal a spin-spin relaxation time T_2 ~ 500 ns. Although this molecule is not a SMM, its strong anisotropic character and its stability in water may enable future technological applications.

2.3 Weakly ferromagnetically exchange-coupled dinuclear $[\mathrm{Mn(II)}]_2$ molecule

Magnetic oxides have gained considerable interest not only as prototype materials for spintronics but they are also potential candidates for catalysis and corrosion applications [64]. A number of theoretical studies are available, which focus on the behavior of their magnetic properties at the nanoscale level. However, so far experiments have failed to catch up with the theoretical work and provide a physical realization of the expected interesting behavior associated with oxides. This section is one such effort to contribute experimentally to the understanding of the magnetic behavior associated to transition metal oxides at the nanoscale. In transition metal oxides the magnetic interactions in the complex can be tuned by altering the particle size, and a clear transition is predicted from nano to bulk phase [65, 66]. Initial theoretical studies revealed that nanoscale MnO clusters embedded in certain symmetry posses a FM behavior in contrast to its AF bulk phase. However more general and extensive studies revealed the existence of an AF coupling at low scales as well. This behavior suggests that the couplings designed within the crystal structure of the complex are central for the magnetic behavior of these systems. Hence it is crucial to design new and stable clusters where the role and effect of exchange interactions is clearly identified on the magnetic properties of the system in question.

The Mn(II) complex with chemical formula $C_{80}H_{64}Cl_8I_{12}Mn_8N_{16}$ [here on referred as Mn(II) dimer) presented in this work is first of its kind, where the complex depicts a hydrophobic environment generated by the $[Mn(bipy)_2Cl]_2^{2+}$, where bipy is bipyridine as shown in Figure 2-9 (a). The complex has C2/c space group. This is achieved using the characteristics of a free atom of Mn, which has a half-filled d and a closed s shell. Thus the Mn_2 is treated as a weakly bonded dimer with the bond strength defined by the van der Waals interaction. The symmetric unit of this complex consists of one dimeric $[Mn(bipy)_2Cl]_2$, and two I_3^- as shown in Figure 2-9 (b), the two I_3^- act as charge balancers for the excess positive charge on the first unit. Moreover there are short contacts between all the Mn2 and O3 with 4 I_3- ions in such a way that the supermolecular 2D-network parallel to the *ac* plane is obtained.

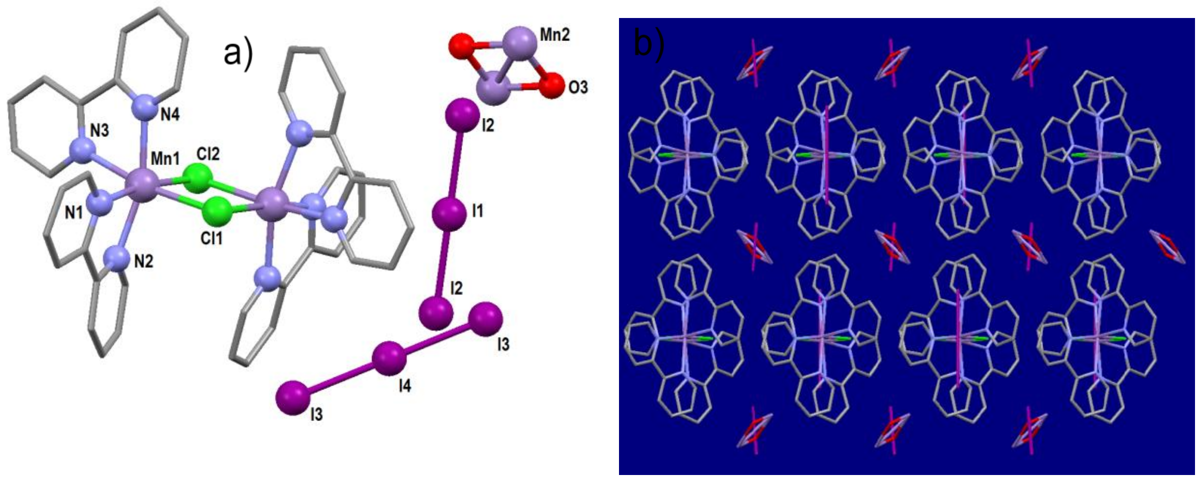

Figure 2-9: a) Molecular view of the asymmetric unit consists of one dimeric $[Mn(bipy)_2Cl]_2{}^{2+}$ *and two* I^{3-} *(purple). H atoms are omitted for clarity. b) Packing of the complex showing the clusters in the hydrophobic pockets.*

In the magnetic susceptibility χ measurements, the χT vs. T plot (not shown here) shows no evidence for magnetic impurities at high temperatures, and at low temperature a clear proof of existence of two weakly ferromagnetically coupled Mn^{II} metals ions each with $S = 5/2$ ground state is revealed. Using the weak field approximation, the data is modeled using isotropic exchange interactions J between the two Mn^{II}. The spin Hamiltonian $H = -2\, J\, (S_1 \bullet S_2)$, where S is the spin of the individual Mn gives $J/k_B = 0.18$K and $g = 1.92$.

2.3.1 Investigation of magnetic hysteresis

The field dependent magnetization $M(H)$ is measured at low temperatures (0.24 to 3.5 K) is shown in Figure 2-10, where M_s is the saturation magnetization. The external field is applied parallel to the crystal's physical long axis and it is swept at a constant rate of 0.6T/min. A fast increase in magnetization is observed at low fields, $H < 0.4$T, reaching saturation at higher fields.

A small coercive field H_c ~ 0.5 KG is observed in the whole range of experimental temperatures (< 3.5 K). The observed hysteresis indicates the presence of intra-molecular interactions (spin-orbit coupling) or inter-molecular interactions (exchange or dipolar).

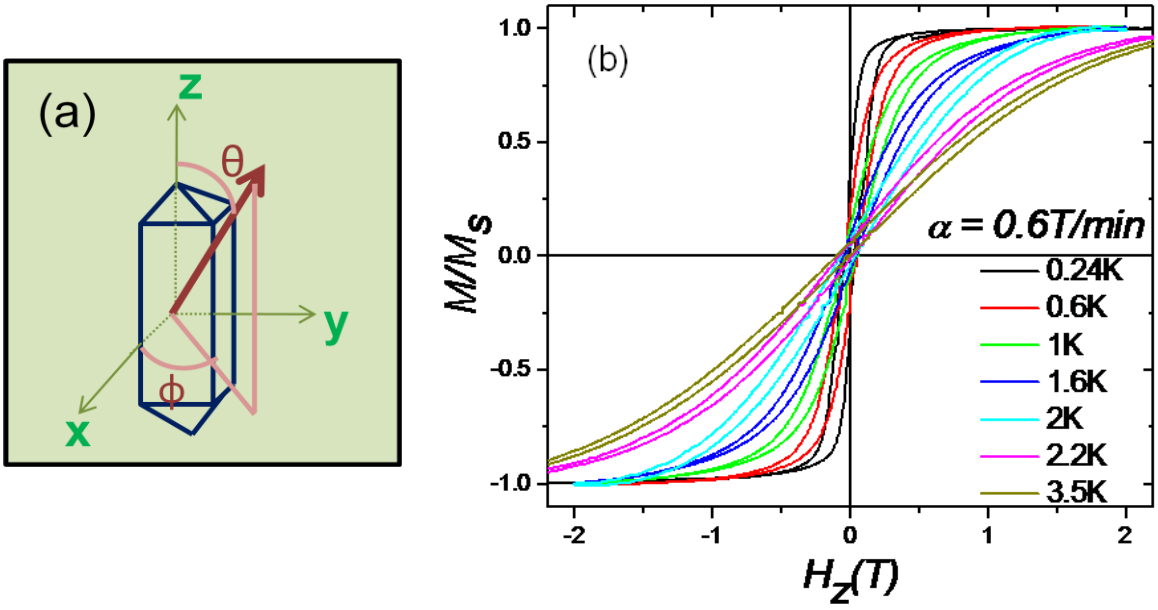

Figure 2-10: a) Orientation of the magnetic field (red arrow) with respect to the crystal axes. b) Hysteresis measurements on a single crystal of Mn(II) dimer over a wide temperature range at a sweep rate of 0.6 T/min.

2.3.2 Single Crystal EPR measurements

The anisotropic nature of the $C_{80}H_{64}Cl_8I_{12}Mn_8N_{16}$ complex is probed via single-crystal electron paramagnetic resonance (EPR) experiments. The sample response was studied over a wide range of frequencies (67 to 177 GHz) and temperatures (2 to 25 K). Figure 2-11 (b) shows the angular modulations of the main EPR resonance observed at 67.3 GHz at the lowest available temperature ($T = 2$ K). As later explained in the text, this transition is from the ground spin projection state to the first excited state. The field was rotated in two orthogonal planes, one of them including the long crystal axis (rotation by an angle θ), and the other perpendicular to it (rotation by an angleϕ), as depicted in Figure 2-11 (a).

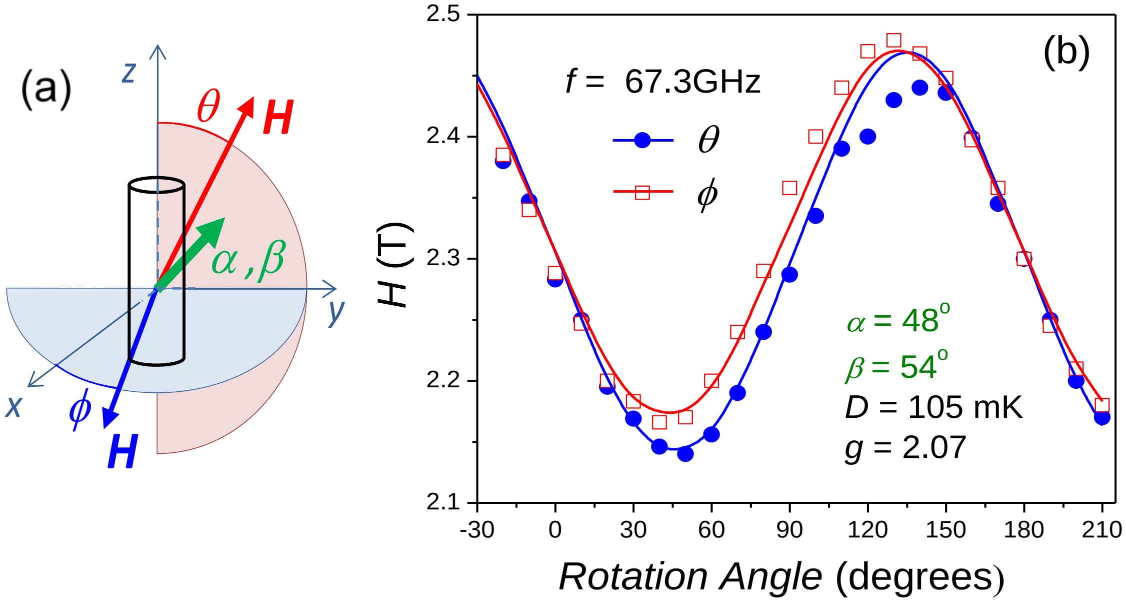

Figure 2-11: a) The rotation of the external field H in two orthogonal planes, as depicted in the Figure 2-11 (b). b) Angular modulations of the strongest resonance observed at 67.3 GHz of the Mn(II) dimer at the lowest available temperature 2 K.

Unfortunately, experimental constraints used in these experiments do not allow one to relate this angle with respect to the crystal faces, so the crystal is represented as a cylinder (Figure 2-11 (a)). Minima at ~ 45 - 225 degrees are observed in both cases, which are expected when the field is applied closest to the molecular anisotropy axis within the rotations. A maximum is observed

~ 135/140 degrees for the two scenarios, which is usually attributed to the field applied close or along the hard axis of the crystal. The solid lines are fits to the data obtained from diagonalization of the spin Hamiltonian;

$$H = \vec{S}.\hat{R}.\hat{D}.\hat{R}^{T}.\vec{S} - \mu_B g.\vec{S}.\vec{H} \tag{10}$$

Where $S = 5/2$ is the Mn(II) spin, $\hat{R}$ is the rotation matrix and $\hat{R}^{T}$ is it's transpose. $\hat{D}$ is the diagonal zero-field splitting tensor arising from spin-orbit coupling, with principal values D = 105 mK, E (= 0 in this case) and $-E$, which is rotated with respect to the crystal x-y-z axes by the Euler angles $\alpha = 48^{o}$ and $\beta = 54^{o}$. The Euler angle β does not provide meaningful information about the orientation of the anisotropy axis within the single crystal. The results show an easy anisotropy axis lying at angle $\alpha = 48^{o}$ away from the long crystal axis. As mentioned above, the x and y axis are arbitrarily oriented with respect to faces of the crystal, consequently β is just used to fit the observations.

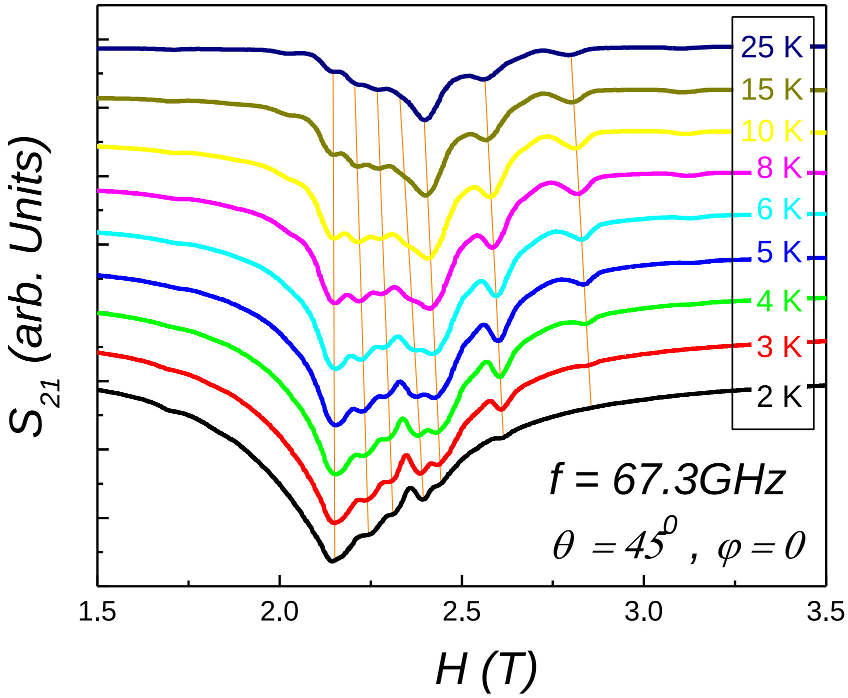

Figure 2-12: Temperature-dependent EPR transmittance spectra of the Mn(II) dimer obtained at the minima in the angular dependence.

Figure 2-12 presents a detailed temperature behavior of the EPR spectrum with the field applied along one of the minima observed in the $\phi = 0$ rotation (Figure 2-11). The results show that the lowest field resonance (H = 2.3 T) can be definitively associated to a transition from the ground spin projection state, since it becomes stronger as the temperature is decreased. A series of well-defined absorption peaks (dips in transmission) are also observed above the ground state transition. At least six more can be clearly identified at higher temperatures. These peaks appearing at field > 2.75T are most probably excited transitions as they tend to diminish and eventually vanish as the temperature is decreased. Furthermore these peaks shift to low fields when increasing temperature, as indicated by orange lines in Figure 2-12. The origin of these peaks is not quite clear, since they cannot be just transitions between the excited energy levels of a single Mn(II) ion of spin S = 5/2, since a maximum of only five transitions would be expected from a single spin S = 5/2. As discussed earlier it is quite hard to analyze the spectra associated with weakly coupled systems because more often the result is a cascade of transitions that are coming from energy states belonging to an individual ion or all the way between and to the case of a reasonably good coupled system represented by a giant spin [21, 67].

Multi-frequency spectrums were also measured at 10 K, to incorporate the behavior of peaks appearing at higher temperature. With the field applied along the minima observed in Figure 2-11, a plot of the peak positions as a function of resonance frequency is shown in Figure 2-13. The symbols depict the experimental points whereas the straight lines are guide for the eyes. As shown earlier multiple peaks are observed, moving to higher field positions as expected with an increase in microwave frequencies. The g values from the linear fit of experimental data give g values between 1.97 and 2.10. Furthermore the first line (black) from the left is the ground state transition as seen in Figure 2-12.

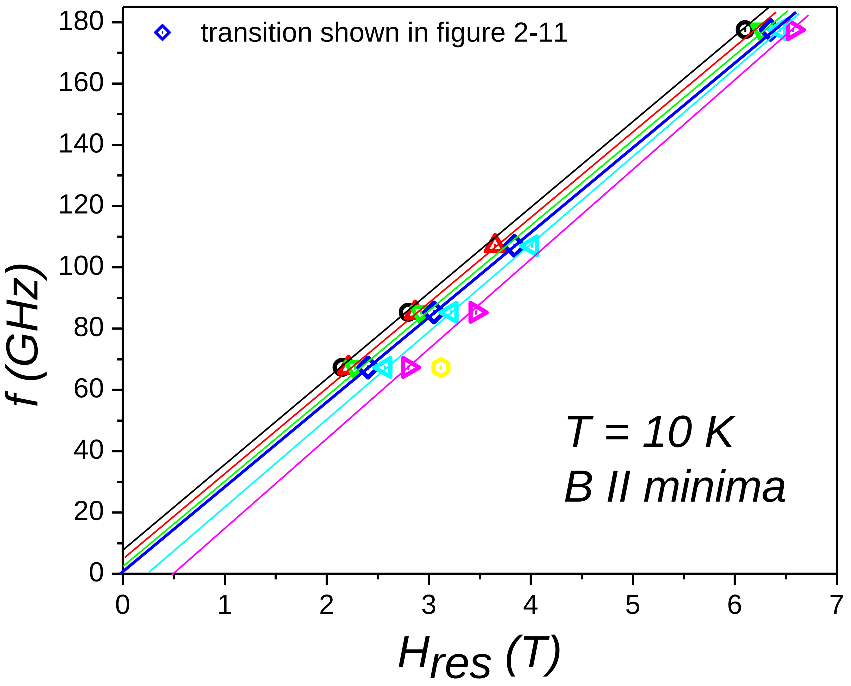

Figure 2-13: Plot of the EPR peak positions of the Mn(II) dimer as a function of the applied magnetic induction strength at 10K.

Using the fitting parameters used earlier to fit the angular modulation, the 67.3 GHz spectrum at 10 K was also calculated. Multiple models were used with: a) Mn(II) spins treated as independent $S = 5/2$ spin, b) two spins weakly coupled, and c) a giant spin of $S = 5$. Unfortunately none of these could provide a conclusive match to the transitions observed experimentally, although we were able to come close to the observations. Figure 2-14 shows one such effort, comparison between the data recorded (continuous black curve) and the spectrum calculated (dotted blue curve) with the parameters $D = 105$mK, $g = 2.07$ and $S = 5/2$. As clearly observed treating the Mn(II) spins as independent $S = 5/2$ spins does not account for all of the observed EPR absorption peaks, although with the above parameters we can narrow down the ground state transition.

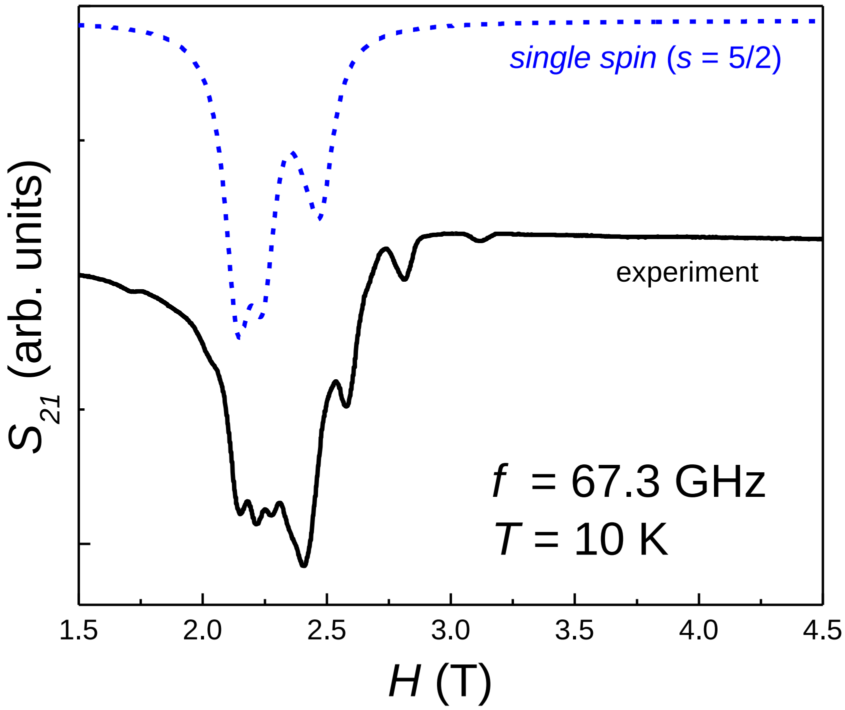

Figure 2-14: a) Comparison between the 67.3 GHz EPR spectrum at 10 K and the calculated spectrum using independent Mn(II) S = 5/2 spins. b) Energy level diagram of a two-spin 5/2 interacting system with weak J.

2.3.3 Discussion of EPR and Magnetometry results

As hinted by the susceptibility results some of these peaks may result from transitions within mixed states existing as a result of a ferromagnetic interaction between the two Mn(II) ions, i.e.

with the system behaving as a weakly coupled dimer, described by the giant spin Hamiltonian. According to the magnetic dipole selection rules, $\Delta S = 0$ and $\Delta m_s = \pm 1$, only a single ground-state transition within a spin multiplet state is expected at low temperatures, $T \rightarrow 0$ [68] , as seen in Figure 2-11, with a total of 5 absorption peaks arising from transitions between the 6 ($2S+1$) spin projection levels of a 5/2 spin. However, systems with weak exchange interactions ($|J| \sim |D|$), can lead to significant state mixing between the compactly spaced low-lying spin levels and multiple transitions can be expected at moderate temperatures. Indeed, exchange interactions between neighboring Mn_2 dimers are also likely in this compound. Mediated by the I_3 ligands, these inter-dimer interactions can be comparable to the intra-dimer exchange coupling and would complicate the energy landscape associated to the resulting spin projection states of this system. The shifts of most of the peaks to lower fields observed in Figure 2-12, when increasing temperature are in support of this possibility. Unfortunately, the complexity inherent to the presence of intra- and inter-molecular interactions in this system prevents a unique quantitative interpretation of the experimental results. What we can conclude from the EPR study is that the anisotropy barrier of this system is too low to account for the magnetic hysteresis observed at temperatures below 3.5 K. The hysteretic behavior is most likely arising from intra- or inter-molecular interactions within the crystal [69].

Hence we present a weakly coupled Mn(II) dimer with chemical composition $[Mn(bipy)_2Cl]_2^{2+}$, the low-temperature magnetic studies show small hysteresis at low temperatures. Detailed EPR measurements as functions of angle, temperatures and frequencies reveal a complicated energy landscape mostly originating from the inter-dimer interaction present on top of the inter-ion exchange interactions present within the dimer. However, the weak exchange interaction and small anisotropy of the individual Mn ions does not allow a comprehensive analysis of the various observed EPR peaks The observed results are attributed to the $[Mn(bipy)_2Cl]_2$ dimer.

CHAPTER 3 RELIEVING FRUSTRATION; THE CASE OF ANTIFERROMAGNETIC Mn(III) MOLECULAR TRIANGLES

The experimental work done on this chapter is done in collaboration with Dr. Stephen Hill group at NHMFL. I am presenting here the whole project to provide a complete description of the interesting aspects of this work. The magnetic measurements were done at UCF, while the EPR were conducted at the NHMFL. This chapter is directly extracted, although conveniently modified from a published article as a result of this collaboration [J. Liu, C. Koo, A. Amjad, P. L. Feng, S. –E. Choi, E. del Barco, D. N. Hendrickson and S. Hill, Phys. Rev. B, **84**, 094443 (2011).

3.1 Introduction

This chapter discusses detailed high-field Electron Paramagnetic Resonance (EPR) and magnetization [low temperature Hall-effect and high field torque magnetometry] studies on the distorted $[NEt_4]_3[Mn_3Zn_2(salox)_3O(N_3)_8].MeOH$ complex [hereafter denoted as antiferromagnetic (AF) Mn_3Zn_2] illustrated in the inset of Figure 3-2(a). In this molecule the distortion from a perfect equilateral triangular geometry resulted in a significant relief of frustration within the molecule. A very clean EPR spectra [an indication of frustration relief] was observed and the EPR measurements identified the existence of a reasonably isolated ground state of spin S = 2, with an appreciable zero field splitting (ZFS) or uniaxial molecular magnetoanisotropy. Moreover, it will be seen that the existence of magnetic hysteresis at low temperature Hall-effect magnetometry indicates a SMM; this behavior is consistent with the large anisotropy reduction observed through EPR. Interestingly high field magnetic torque measurements revealed multiple spin cross over transitions involving the (S > 2) higher spin value excited states. An excellent agreement is observed between experiment and the simulations performed using the multi-spin Hamiltonian. In the present study, the Hamiltonian is solved by including contributions of the single-ion anisotropies of each Mn and the AF exchange coupling between the Mn….Mn ions.

In the literature an extensive assortment of SMMs are present that contain Mn(III) as the transition ion magnetic core [22,21,70,71]. The primary focus of the thesis resides on characterizing low-nuclearity systems as they are likely to represent the ‘‘molecular’’ nanoscale bricks for the synthesis of high-nuclearity molecular clusters [72]. Furthermore it is the proclivity of octahederally coordinated Mn(III) to undergo a Jahn-Teller (JT) distortion, the outcome of which is a considerable Ising type easy-axis magnetoanisotropy, and large and negative zero field splitting D [14,57], yet another criteria physicists and chemists look for in a good SMM. The aim is to explore new strategies to improve overall molecular anisotropies in these systems. The particular interest lies in exploring the interplay between isotropic (Mn . . . Mn) exchange interactions and single ion anisotropy. Along this stream of research, quite extensive studies have been done on the ferromagnetic (FM) Mn(III) molecules, the credit goes to the existence of no disordered solvents molecules in these high symmetry crystals [73, 74]; however the literature has been lacking considerably spectroscopic information on AF triangular Mn(III) molecules till now. The primary reason is the lack of clear EPR spectra due to the inherent frustration in these molecules For a long time, the presented triangular topology was believed to result in AF coupling with a low spin ground state and for a decade or so there has been exceptional improvement in the synthesis, one such example is a ferromagnetically coupled molecule with a

[Mn_3-(μ_3-oxo)] core and $S = 6$ spin [13, 75-78]. These triangular units are also in great demand as building blocks for larger molecules to achieve higher blocking temperatures (T_B) and anisotropy barriers.

3.1.1 Competing interactions and geometric spin frustration in molecular magnets

Spin frustration is by definition a system's inability to cope with AF interactions between spins on neighboring sites within the same magnetic entity. In other words, the system cannot satisfy all the interactions present. The result is a pool of low lying energy states that cannot simultaneously be minimized. Also, even in systems that project significant Ising-type anisotropy, the frustration not only leads to a high density of low lying spin states but also results in significant state mixing [57]. Furthermore, some specific frustrated magnets show a tendency to evade Néel ordering, i.e. the frustration leads to a reduction or complete suppression of the magnetic ordering system.

Competing interactions and low dimensionality in crystals can be either a natural manifestation, i.e. the crystal growth forces the magnetic moments to occupy sites on a frustrated unit cell, or as a result of artificial production by various fabrication techniques. The most extensively studied spin frustrated systems are the geometrically frustrated magnets, i.e. the geometrical properties of the crystal lattice obstructs the simultaneous minimization of the interaction energies at given sites. As the temperature is lowered, spin-spin interactions in the system start dominating the thermal fluctuations and the spins further lower their energy by ordering with each other. This topological effect can be attributed to the competition between AF magnetically coupled spin carriers and ferromagnetic polarization [48]. The most common alignment of these spins is anti-parallel. Figure 3-1 (a) is an example of a system in which spins are at the corner of a square plane; it is very easy to satisfy the requirement of AF interactions between neighboring spins and there is no impediment to the establishment of nearest neighbor spin order [79]. However, consider an AF coupled equilateral triangle ABC with three spins, one on each vertex and same *J*'s on all three bonds (Figure 3-1(b)). Consider Ising spins [each spin can take on only two values up or down], the system has $2^3 = 8$ possible states. Now all spin-up and all spin-down configurations are not the ground states, where as the rest of the six are ground states and in all these, there will always be two favorable interactions and an unfavorable one. The unfavorable one is faced with the dilemma of orienting itself in a way to reduce the energy of the system to result in a single unique ground state. Hence a conflict arises between the geometry of the space defined by the degrees of freedom and the interaction preferred by local correlations. Whichever way it decides, one of the neighbors will end up with higher energy and the system will possess a variety of similar low energy states. Hence the system exhibits frustration.

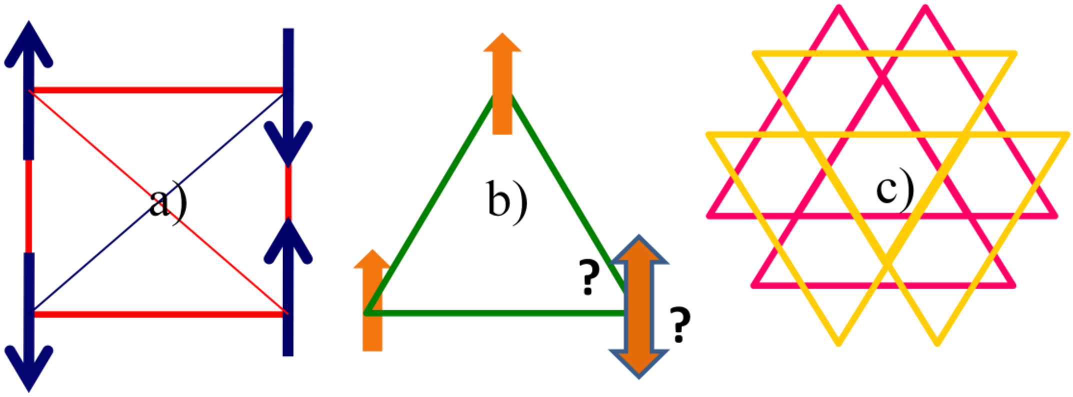

Figure 3-1: a) Unfrustrated system, b) frustrated AF equilateral triangle, c) Kagome (T8) Lattice.

The concept of geometric frustration came to surface in 1950, when it was noticed that Ising AFs on a triangular lattice behave differently in comparison to FMs [80].Spin frustration is particularly intersecting in molecular magnetism as it can give rise to qualitatively new states of matter and macroscopic degeneracies. Based on the complex magnetic or thermal history this frustration will lead to hysteresis and time dependent relaxation towards equilibrium. An evidence of frustrated systems is the appearance of broad contentless EPR absorptions [75, 76]. More fundamentally, although AF ordering is known to exist at very low temperatures, in frustrated systems a classical ground state of a quite different sort may occur. These systems are interesting because of their unique behavior as compared to ordinary, unfrustrated magnets. Where conventional magnets order with a decrease in temperature, strong fluctuations may prevail in frustrated magnets even at low temperature.

These competing interactions are not limited to triangular topologies. More sophisticated spin frustrated lattices can be synthesized by basic connections of triangles and square lattices [81], for example, the Kagomé lattice (T8) shown in Figure 3-1(c). Since frustration obscures the way to easy formation of ordered spin-states, these higher dimensional complexes are especially appealing if we are interested in understanding the exotic quantum paramagnetic spin-liquid ground state [a manifestation of geometric frustration and quantum fluctuations], spin glasses (random freezing of spins), spin ice (a special case of a spin liquid) and the observation of long range phase order [82].

In this work, the basic interest is placed on understanding how topological distortions lead to a reduction of frustration in low nuclearity systems and result in a well-defined ground spin state.

3.2 Experimental magnetic and EPR studies on AF Mn_3Zn_2 triangle

The current work on AF Mn_3Zn_2 molecule exhibits a trigonal bipyramidal structure, with an approximate planar $[Mn_3^{III}\text{-}(\mu_3\text{-oxo})]^{7+}$ triangular core as shown in inset of Figure 3-2 (a) [75]. Each Mn(III) (d^4) ion in this core is placed in octahedral coordination geometry with an axial Jahn Teller elongation. The neighboring Mn(III) ions are magnetically coupled via peripheral oximate (Mn-N-O-Mn) bridges (important for realizing the sign of the exchange interaction) [13,76] and the central – $\mu_3$oxo bridge atom. In our case, the oximate bridges lie close to the Mn core, resulting in AF coupling. The Mn-azide bonds are oriented along the axial JT distortion axis and connect the core to the two tetrahedral, non-magnetic Zn ions. These capping Zn^{II} ions lie above and below the triangular plane, however they do not contribute directly to the magnetic moment of the molecule, but they are effective in constraining the Mn(III) JT axes, which lie approximately < 3.7^o away from the normal to the plane of the Mn_3^{III} triangle.

AF Mn_3Zn_2 crystallizes in the monoclinic $P2_1/n$ space group [unlike most of its family] [75], the non axial symmetric terminal azido-ligands restrict the occurrence the 3-fold axial symmetry hence prohibiting the occurrence of an equilateral Mn_3^{III} triangle. The result is Mn(III) sites within the molecule setting themselves at ends of an inequivalent triangle, resulting in three different exchange coupling constants and three distinctive ZFS tensors. This inequivalence then relieves the spin frustration in the molecule. This low symmetry further results in two differently oriented molecules within the unit cell i.e. the $Mn_3^{III}\text{-}(\mu_3\text{-oxo})]$ planes are misaligned by approximately 32^o. The crystal single easy axis direction is actually an average of the two sites, i.e. approximately 16^o from each of the local easy axes. Furthermore even with its low symmetry we are expecting considerable easy-axis anisotropy because of the nearly parallel JT axes.

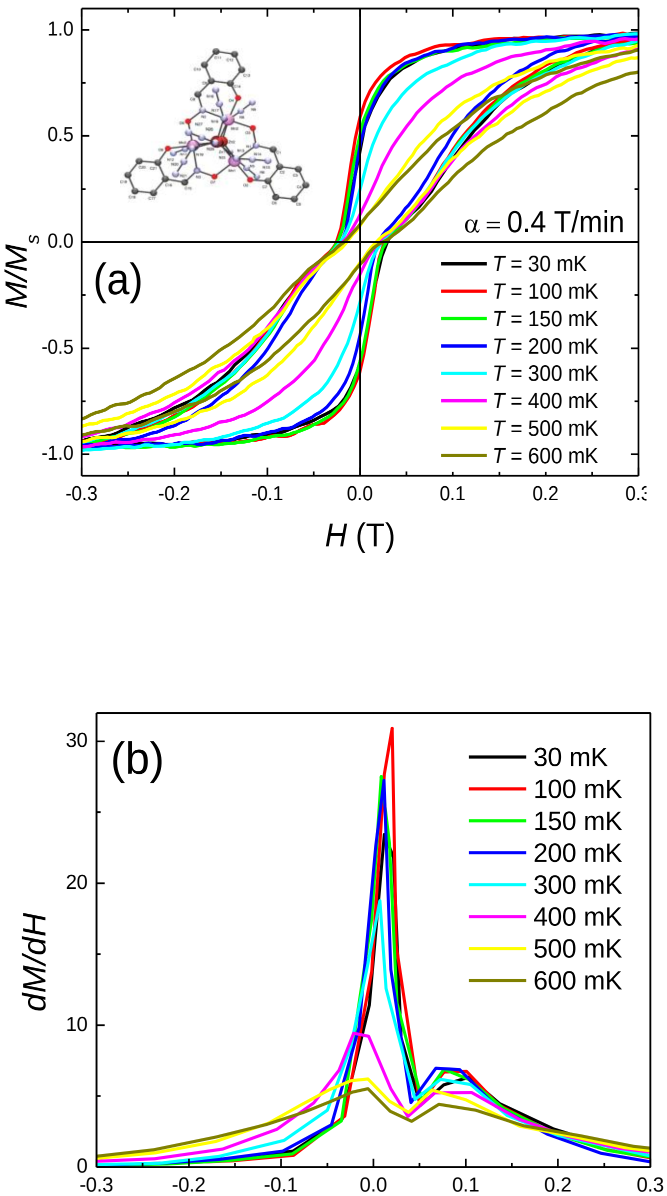

Figure 3-2: a) Hysteresis as a function of the applied magnetic field at different temperatures below the blocking temperature; M_s represent the low-field (<10 T) saturation magnetization. The inset shows the Structure of the AF Mn_3Zn_2 molecule; viewed from directly above the plane of the triangular Mn_3 core. b) The field derivative of the magnetization curves shown in part a.

The small oximate bridge's distortion angle and the fact that these lie close to the plane of the shift of the Mn_3 core and the shift of the μ_3-oxo center signify the occurrence of AF exchange interactions between the Mn(III) ions. The existence of dominant anti-ferromagnetic interactions is further explored via magnetic susceptibility studies. The structure was measured to have a $\chi_m T$ value of 7.38 cm^3 mol^{-1} K at 300 K. This value decreases with temperature, and a minimum is observed at1.85 cm^3 mol^{-1} K at 4.83 K, reaching 1.98 cm^3 mol^{-1} K at 1.8 K [75]. This low temperature data suggests a low spin ground-state $S = 2$ and antiferromagnetic exchange. The near parallel JT axes result in the easy-axis type magnetoanisotropy of the molecule. Based on EPR studies, we anticipate significant easy type magnetic anisotropy for the members of this family. The crystals are plate-shaped, with the average easy axis lying perpendicular to the largest flat surface.

In order to probe the anisotropy and resonant (QTM) of the complex, sensitive low field magnetization measurements were performed on a single crystal. Figure 3-2 (a) shows the magnetization response of the sample, with temperature ranging from 30 mK to 1.3 K. The external field is applied parallel to the average easy axis of the crystal i.e. perpendicular to the large flat surface of the crystal. Magnetic hysteresis is observed at low temperatures, the hysteresis indicate an opening of the loop at a temperature of 1 K at a sweep rate of 0.4 T/min; this loop continues to increase as the temperature is decreased to 0.2 K. The relaxation below this is temperature independent, suggesting a complete suppression of the thermally activated phenomenon. Hence the residual relaxation is most likely due to processes that involve the quantum tunneling via the lowest lying spin states and/or direct spin lattice relaxation. Furthermore the magnetic hysteresis shows an onset at a blocking temperature of ≈ 0.8 K. This behavior is a consequence of magnetic molecular bistability originating via the anisotropy barrier separating the spin up and down projection states [21]. This behavior in addition to the clear step observed at zero fields as seen in the inset of Figure 3-2 (b), can be described as a consequence of resonant QTM [16]. A ground spin S of 1.7 (≈ 2) is suggested by the fitting of the Langevin function to the high temperature magnetization curve. It should be noted that these observations achieved at low temperature are unique in itself for this high symmetry. As for AF Mn_3 single crystals, extensive studies on the observation of the above mentioned SMM properties of AF Mn_3 complexes [Complex 4 in Ref. 75] have been futile to this moment.

The unit cell of the AF Mn_3Zn_2 complex has two differently oriented molecules with unique easy axis directions, resulting in two distant peaks in the EPR spectra. In order to perform high frequency EPR measurements as function of frequency and temperature, it is essential to first find the average easy axis of the molecules in the unit cell. For this purpose angle dependent EPR measurements were carried out and the average easy axis was found to be approximately 16^0 away from the local easy axis (z-axis) of each molecule. Multiple high frequency EPR measurements were performed on a single crystal using cavity perturbation techniques over a range of frequencies up to 600 GHz, and temperatures up to 20 K, for both low and high magnetic fields as illustrated in Figure 3-3. Two distinguished patterns in the spectra are observed; a) at low fields and frequencies, complicated patterns of sharp transmission peaks appear with increased temperature and except for a few isolated peaks, the rest of the intensities tend to diminish as the temperature drops to approximately 2 K. b) At low fields and higher frequencies more clear peaks in the spectra were observed.

This chapter will focus on the relatively stronger peaks labeled as *α* [this peak appears at all temperatures but at only frequencies > 500 GHz], *β, γ* and *δ* [peaks are observed at very low frequencies only]. The sharpness of these peaks indicates the high merit of the crystal. Further analysis of the temperature dependence data designates *α, β* and *γ* resonances as the ground state resonances, where as we can definitely state that the jungle of peaks observed at high temperatures are a result of transitions occurring among the low-lying excited spin states. We continue to observe this behavior for lower frequencies well below 244 GHz all the way down to 67 GHz.

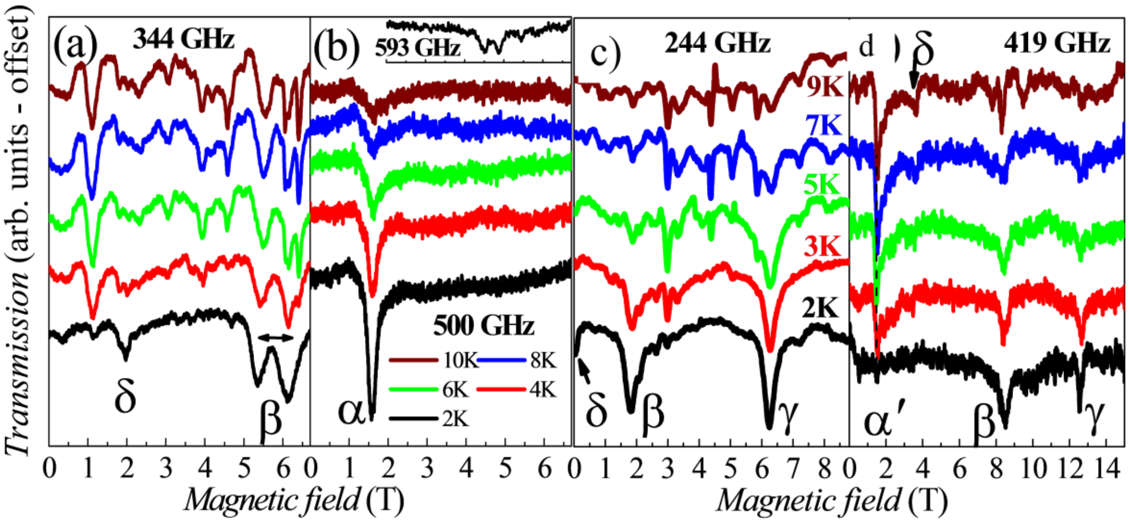

Figure 3-3: In all figures, the transmission versus magnetic induction of AF Mn_3Zn_2 molecule at various frequencies and five temperatures spanning the range 2-10 K. The ground-state resonances observed at the lowest temperatures have been labeled accordingly. At the highest frequency (593 GHz) reveals α resonance at a temperature of 2 K.

An interesting feature in these EPR spectra is the observation of multiple resonances at low temperatures, especially when the magnetic dipole selection rules [$\Delta S = 0$ and $m_s = \pm 1$] only allow a single ground-state transition within a spin-multiplet state. The reason of the breakdown of the selection rules is the strong mixing between the abundant low lying levels (as will be explained later in the chapter, as illustrated in Figure 3-5), the primary sources being substantial spin frustration in the molecule and the fact that the exchange coupling between the Mn(III) in the molecule is relatively weak ($|J| \approx |D|$). Since these levels are mostly responsible for the peak intensities in EPR spectra, S and m_s stop being the ideal quantum numbers to explain the transitions [83]. From here on the focus will be only on the ground state transitions, since it is extremely crucial to understand and extract the information from the inordinate number of peaks observed in the thermally excited EPR spectra. Furthermore, it would be prudent to avoid these terms in the Hamiltonian since the Hamiltonian parameters are extremely sensitive to the positions of these transitions (vide infra). In order to track the origin of the ground state transitions, detailed frequency dependence measurements were done at the lowest possible temperature of 2 K over a wide range of frequencies, for instance from 50 GHz to 600 GHz.

At 334 GHz β appears as two peaks with a spacing of about 0.8 T (Figure 3-3, (a)), where as only a single β peak is observed at lower and higher frequencies as shown in Figure 3-3, (c) and (d). The origins of the double peaks lie primarily with the two molecular orientations and to the existence of misalignment of the sample. The same manifestation was observed for α at higher frequencies (593 GHz). It is also possible to confirm the above statement by running simulation for a 3^0 to 5^0 degree misalignment. Figure 3-4 shows the energy landscape of the molecule highlighting the positions of the resonances observed at different frequencies. The double-peak data point occurs on the 2D plot as the average position of the peaks. Furthermore, the error bars reflect the associated uncertainty. The lower field side of the plot shows larger error bars as compared to the higher fields where we were able to get a better alignment of the crystal for the EPR high frequency measurements. In order to calculate the zero field splitting parameters associated with each of the labeled resonances observed at each frequency, linear fits were calculated for the Figure 3-4. The solid lines indicate the linear fits for α, β and δ resonances, where as second order polynomial was used to fit the curvature observed in the γ resonance data. The parameters observed are as follows; $\Delta\alpha$ = 459(2) GHz, $\Delta\beta$ = 196 (2) GHz, $\Delta\delta$ = 245 (2) GHz and $\Delta\gamma$ = 66 (2) GHz. The average slopes of the linear fits agree quite nicely with the parameters expected for an axial system like Mn(III) with Δm_s = +1 and g = 2.00, keeping in mind an approximately 16^0 misalignment from the easy axis because of the two molecular orientations. The curvature observed in the γ is attributed to the coulomb repulsion between the Zeeman levels i.e. state mixing. This is an expected consequence due to the presence of residual spin frustration in the crystal. For the δ resonance, the g value is closer to 4.00 [3.60 (7) when corrected for sample alignment] as is calculated from the slope of the linear fit. This g value suggests that this resonance is either a double quantum transition (Δm_s = +2) or involves strongly admixed states. Over a range of temperature frequencies and fields, Figure 3-3 (b) and (d), it is observed that the intensity of the δ resonance vanishes at higher fields with lower temperatures; whereas an opposite behavior is observed at lower fields and frequencies Figure 3-3 (a) and (c). Furthermore as seen in Figure 3-4 it is completely absent at high frequencies such as 500 GHz and is observed only at 419 GHz at elevated temperatures, hence making it unlikely that δ resonance is a result of an excitation from the ground state. One can speculate in light of the observed data that a low lying state ($|m_s < +2|$) excitation is involved, that vanishes at low temperatures due to the depopulation triggered by the applied field. Two more resonances observed in Figure 3-3 (b) are the excited state resonance labeled as $\alpha^{\prime}$ and $\beta^{\prime}$. The $\alpha^{\prime}$corresponds to a Δm_s = -1, i.e. from the metastable m_s = +2 state to m_s = +1 state [In SMM $\alpha^{\prime}$ is a ground state transition within the metastable potential well]. The $\alpha^{\prime}$ transition has the same zero field intercept as α and is related to the α resonance through the inversion of the field; α corresponds to Δm_s = +1, (m_s = -2 state to m_s = -1 state). The same holds true for β and $\beta^{\prime}$. In SMMs, this behavior usually corresponds to a ground state transition within the metastable potential well [21].

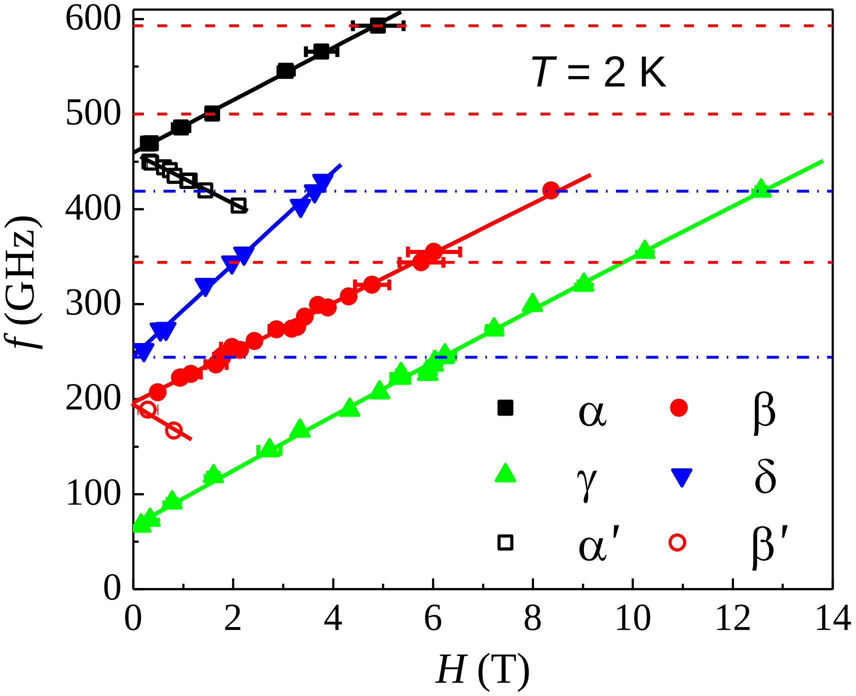

Figure 3-4: 2D energy landscape (frequency versus B) of the resonance positions of Mn_3Zn_2 observed within the range of 60 to 600 GHz with the field applied parallel to the average easy-axis direction. The dashed horizontal lines depict the measurements shown in figure 3-3.

From here on the focus will be on Δ_α, Δ_β and Δ_γ, these parameters that describe the spacing between the ground state and the lowest lying excited states accessible via the magnetic dipole operator. We start with the assumption of a completely frustration-free system i.e. the strong exchange limit. This limit allows us to essentially set one of the exchange interactions in the molecule to be zero [as in the case of a linear AF trinuclear molecule], while keeping the other two exchange interactions large compared to the single-ion anisotropy. This scenario is well studied in the case of molecular magnets [13, 69,76,79, 84].

The initial analysis is based on many approximations (some not well-justified), however at the end of this chapter it will be proved that the results obtained from a more exact calculation are equivalent. The approach employed is a simple theoretical framework that comes in handy to acquire reasonable estimates for guiding the experiments. The ground state is treated as a rigid $S = 2$ spin, with a molecular anisotropy $D_{mol} = (64/49)d$, where d parameterizes the Ising-type easy axis ZFS associated with the individual Mn(III) centers; for simplicity these are assumed to be identical and parallel. As discussed later, using the best fit value of $d = -4.9$ K, $D_{mol} = -6.9$ K is achieved. It is worth noting here that this value is approximately six times larger than the D_{mol} observed in the case of FM Mn(III)$_3$ molecules (1.2 K) [75]. This implies that our molecule has the potential for a very significant magnetization reversal barrier ($\approx |DS^2|$); in spite of the presence of a lower spin $U_{AF} \approx 28$ K compared to that observed for the FM cases ≈ 45 K. This crude technique suggests a colossal ground state ZFS, $\Delta_0 = (2S-1)D_{mol} \approx 20.7$ K (430 GHz) for $S = 2$, hence necessitates the use of unusually high frequencies for the experiment. This value is very close to the experimentally determined value for α resonance i.e. $\Delta\alpha = 459$ (2) GHz. This however is not a coincidence, as will be shown later that this spacing does indeed belong to a roughly $S = 2$ ground state. The small difference < 10% between $\Delta\alpha$ and the estimated strong exchange Δ_0 is a consequence of our approximation, which also cannot explain the β and γ ground-state resonance branches. A multispin Hamiltonian shown in equation 8, for $i \geq j$ is used to stimulate the spectrum. As mentioned before the single-ion anisotropies are of the Ising type and are the same for the three Mn(III) centers, and parallel to z-axis. Further for simplicity we assume isotropic Zeeman interactions for all the ions ($g = 2.00$). The second summation in the Hamiltonian parameterizes the isotropic coupling between the spins; here we have the possibility of having different exchange constants between the ions. Under these assumptions the current Hamiltonian provides two critical pieces of information: (a) we can relieve the frustration in the molecule by appropriately choosing the three exchange constants J_{ij}; (b) there is no restriction on the relative magnitudes of d and coupling constants.

The data is simulated in light of the earlier described magnetic measurements, that shows that the AF Mn_3Zn_2 has a reasonably isolated $m_s = \pm 2$ ground state [Figure 6 and 7 in ref 75], and as our expectation was that with this state (i.e. $m_s = \pm 2$ to $m_s = \pm 1$) the ZFS should be greater than 400 GHz, it is reasonable to assume for computational analysis that this transition corresponds to the α resonance branch in Figure 3-4. This hypothesis gains strength when we look at the intensity of α' resonance (excited state). This resonance quickly takes over the ground-state β and γ resonances. This indicates that the matrix elements of the α and $\acute{\alpha}$ [which should be the same] are notably stronger than those of the β and γ resonances. This conclusion is achieved by comparing the intensities recorded at a single frequency. Therefore in our efforts to simulate the EPR data, the α resonance branch acts as a milestone. Later in this chapter it would be demonstrated that in taking the above approach, we were able to come up with vigorous, testable predictions regarding the spacing of the excited spin states relative to the nominal $S = 2$ ground state. For the best simulations restrictions were applied on the axial parameters to values in the range of 4 to 6 K. Our range is also fairly accurate on the basis of EPR studies of related FM complexes, where d is relatively independent of structural distortions that affect the exchange constants [13]. Further optimization is achieved by playing with the three exchange coupling constants, but here again the limitations like the susceptibility data [75] do not allow us to designate a value to J beyond 25 K. The best simulation of the zero-field eigenvalue spectrum obtained from equation 1 is shown in Figure 3-5 (a). The highest energy states belong to a well-defined spin multiplet and Figure 3-5 (b) is the expanded view of the low lying excited states responsible for the majority of the low-temperature EPR data; the different colors and sizes of the data points have been coded according to $<\sqrt{\boldsymbol{S(S+1)}}>$ expectation values. Because of the assumption of axial anisotropy [parallel orientations on the three Mn(III) centers] m_s is a good quantum number for the simulations instead of S. The simulated ZFS values between the ground and relevant excited states are $\Delta\alpha_{sim}$ = 459 GHz, $\Delta\beta_{sim}$ = 196 GHz and $\Delta\gamma_{sim}$ = 69 GHz. These values match remarkably well with the ZFS values observed experimentally; $\Delta\alpha_{exp}$ = 459 GHz, $\Delta\beta_{exp}$ = 196 GHz and $\Delta\gamma_{exp}$ = 66 GHz.

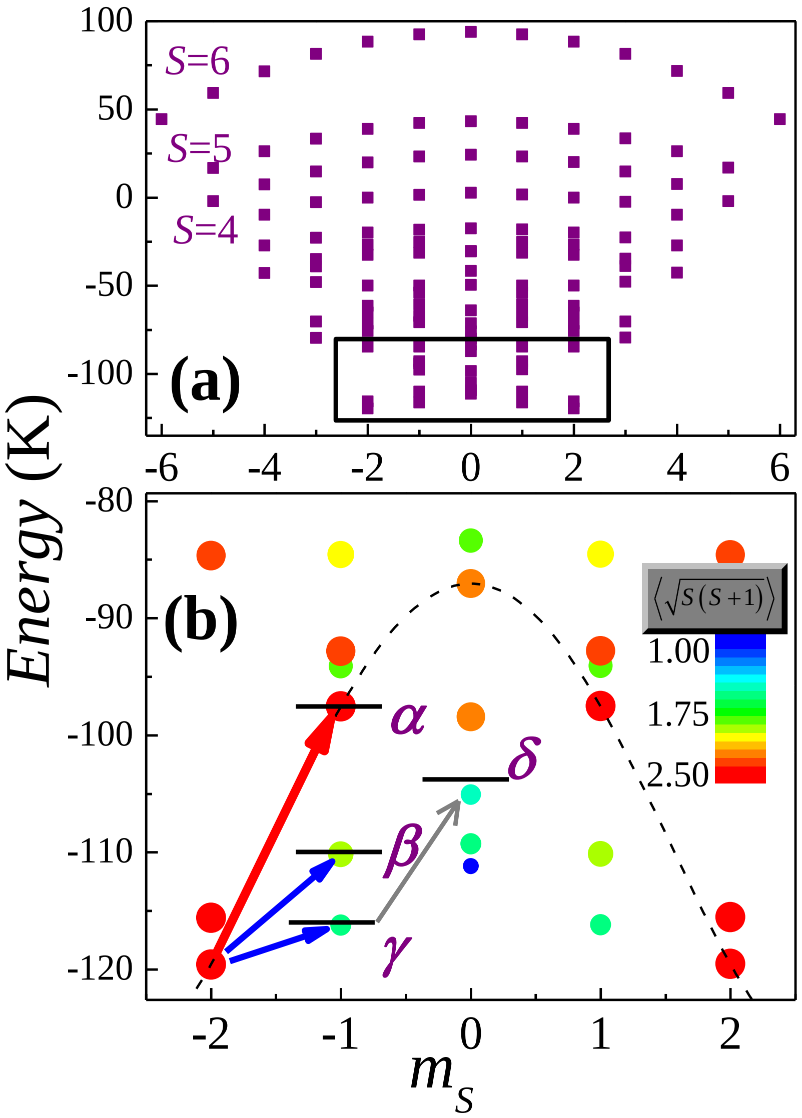

Figure 3-5: For the AF Mn_3Zn_2 molecule (a) Simulation of the zero-field eigenvalue spectrum generated from Eq. (8) using the best fitting parameters, (b) Plot of the expanded low energy spectra, indicated by the black rectangle in a. The different colors and sizes of the data points have been coded according to the expectation value of $\sqrt{S\,(S+1)}$, with radii proportional to this value. The details on the arrows and solid lines are provided in the text.

The horizontal black lines in Figure 3-5 (b) indicate the experimentally calculated excitation energies ($\Delta\alpha$, $\Delta\beta$, and $\Delta\gamma$) above the ground state, whereas the dashed horizontal line corresponds to the energy separation $\Delta\delta$ from the lowest-lying $m_s = -1$ state. The α resonance depicts a solid curve; it is attributed to the fact that it involves states with similar expectation values of the total spin, i.e. the states belong to a nominal ground state of $S = 2$, whereas β and γ resonances connect states of unique total spin values. Nevertheless, the matrix elements associated to with these transitions are non-negligible. As for the remaining δ resonance, it is safe to conclude that the origin of this resonance lies in the low-lying excited state with $|m_s| < 2$, as this transition is indeed explained by the current parameters and is specified by the gray arrow in Figure 3-5 (b). The dashed horizontal line, labeled δ, is the experimental representation of the excitation energy $\Delta\delta$ from the lowest-lying $m_s = -1$ state. The figure shows it is good enough agreement, along with the fact that the states involved exhibit similar *S* characteristics of size and color. Moreover, the lowest-lying $m_s = \pm 1$ states appear just above (~ 3 K) the ground state at zero field.

It is reasonable to predict a high population of states at zero fields, even at the lowest possible temperatures that the system allows. However, when a magnetic induction of 4 T is applied parallel to the z-axis, we observe an approximate 6 K increase in the separation from the ground state compared to the zero field result. For temperatures close to 9 K, this is consistent with the appearance of δ resonance at the induction of 4 T. In light of the earlier EPR analysis, we expect a spin-crossover transition from $S = 2$, a low spin state, to $S = 6$, a high spin state at high magnetic fields as shown in Figure 3-6. Our simulations indicate that the low-energy portion of the energy spectrum is field dependent. The simulations performed took into account the assumption of field alignment parallel to the average easy axis i.e. 16^0 away from the local easy axes of each molecule. Three transitions are observed, the α transition within the multiplet [from the nominal $S = 2$, $m_s = +2$ ground state to the $m_s = +1$ excited state], β and γ are the result of transitions from the ground state to the excited spin multiplet. A rather interesting transition is observed at higher B, 25 T < field < 35 T as shown with black arrows. This represents the spin cross over transitions from the low spin, low field state |2, 2> to the high spin, high field state |6, 6>. Figure 3-6 (b) displays the calculated variable temperature magnetic moment per molecule. Also a high field study is expected to provide an additional constraint on the spin Hamiltonian parameters.

High field torque magnetometry experiments were performed on a single crystal of AF Mn_3Zn_2 in the National High Magnetic Field Lab (NHMFL) in Tallahassee. The sample was placed on the edge of a capacitative sensing, harmonic cantilever beam torquemeter. The change in capacitance is directly proportional to the magnetic torque on the sample. The system works with a 32 mm bore, 36 T resistive magnet and has the ability to vary temperatures from 0.3 to 10 K using a ^{3}He refrigerator. In torque magnetometry experiments one must ensure a reasonable torque signal, leading to the assumption of a linear capacitance response to the deflection of the cantilever beam which, in turn, is directly proportional to the torque ($\tau = |\boldsymbol{M} \times \boldsymbol{B}|$) on the sample. The fact that torque measurements not only require a prior knowledge of the magnetic anisotropy tensor but also the complete knowledge of the spin Hamiltonian parameters makes the magnetic measurements highly complicated to analyze. This is so because of the following reasons; 1) the torque signal in the vicinity of a spin-crossover transition is sensitive to any mixing of levels and also in response to the transverse anisotropy terms, 2) the torque is not a true thermodynamic quantity, where as magnetization and susceptibility are. The former is ignored in the present study, due to insufficient experimental restrictions [85]. Nevertheless in regions where there is sufficient gap between the ground and the excited spin states; one expects a monotonic dependence of the low temperature signal on the magnetic field strength.

The flat crystal was placed on the cantilever in a way to guarantee close alignment of the applied magnetic field to the minimum torque signal. This was achieved by using the system's ability to measure at different angles of the applied field to the crystal. We followed two simple steps, first the angle dependence of the torque signal at 1T [for this purpose the samples are mounted so that the rotation plane is perpendicular to the largest flat surface of the crystal, thus at the zero angle it ensures field alignment close to easy axis] was measured, second the probe was aligned within 1^{o} of the minimum torque signal. This leads to negligible torque at low fields (magnetization being approximately parallel to applied magnetic field). Nonetheless, a misalignment in these systems is inevitable, resulting in a strong torque at high magnetic fields. Furthermore, this initial placement allows us to assume that the same field orientation is also nearly parallel to the average easy axis direction.

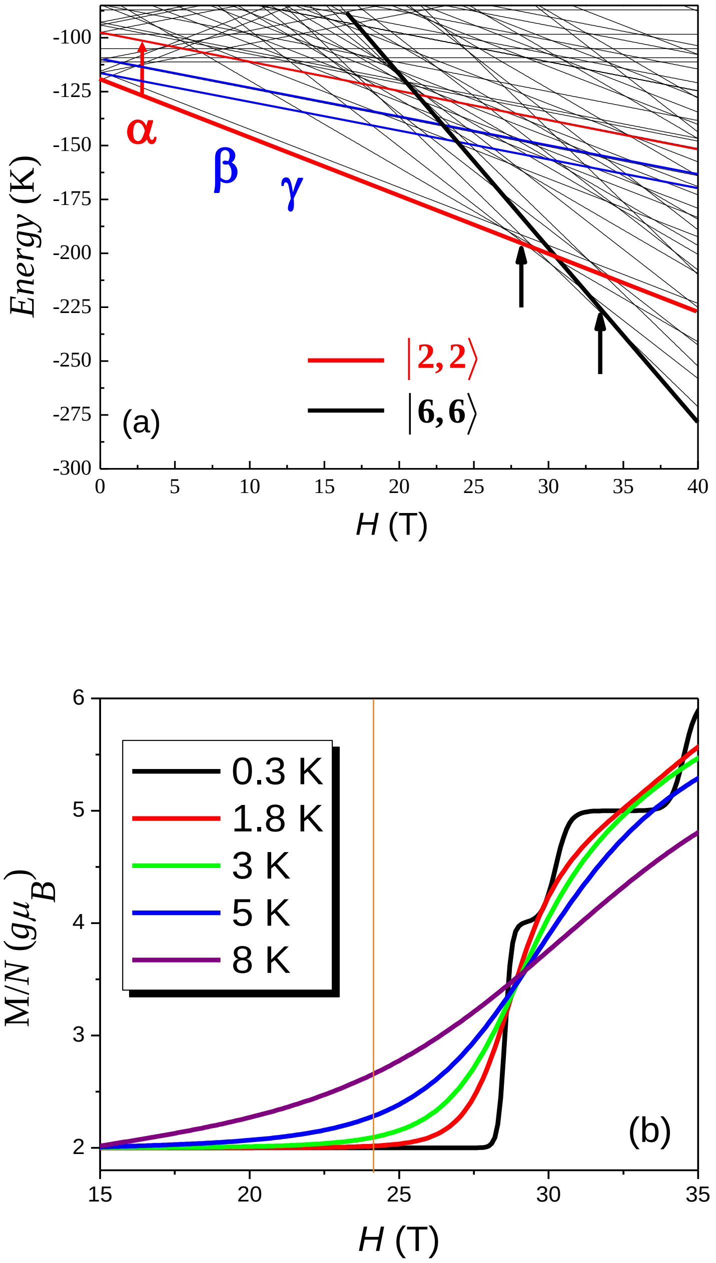

Figure 3-6: a) Simulated Zeeman diagram representing the field dependence of the low-energy portion of the spectrum. The vertical black arrows above 25 T indicate positions of spin-crossover transitions from the |2, 2> state at low field, to the presumed |6, 6>. b) The same behavior is displayed for the magnetization, depicting the simulated high-field magnetization.

Figure 3-7 (a) shows the capacitance of the cantilever magnetometer in high magnetic fields for variable temperatures. The measurements are conducted at a constant magnetic field sweep rate of 3 T/min. Clear low temperature oscillations were observed between 28 to 35 T, which is attributed to the existence of multiple spin-crossover transitions. The existence of these oscillations on a monotonically increasing torque signal signifies the steady population of the excited spin states, all the way up to higher spin values ($S = 6$). The behavior continues to appear with increasing temperatures until about 5 K. In the Hamiltonian, this effect can be understood as a consequence of the competition between diagonal and off diagonal components of the anisotropy tensor. Also the oscillations occurring just below 30 T and at 0.9 K suggest spin crossings between states lying just above the ground state.

3.3 Discussion

As expected the torque magnetometry provides compelling support for the Hamiltonian parameters estimated from the EPR analysis. Hence the simulation accounts very well, for the zero field intercepts associated with the individual resonances observed in the experimental data, and also includes the magnetic field range of the torque oscillations, as shown in Figure 3-7 (b). The locations of the spin crossover transitions is an additional discriminator in determining an appropriate simulated fit; the first step is the construction of a four dimensional χ^2 (d, J_1, J_2, J_3) surface via comparison of the simulated values of $\Delta\alpha_{sim}$, $\Delta\beta_{sim}$ and $\Delta\gamma_{sim}$; the next step is the search for the minima on that surface. Any minima that did not produce spin-crossover transitions in the experimental magnetic field range, 25 T < B < 36 T are discarded.

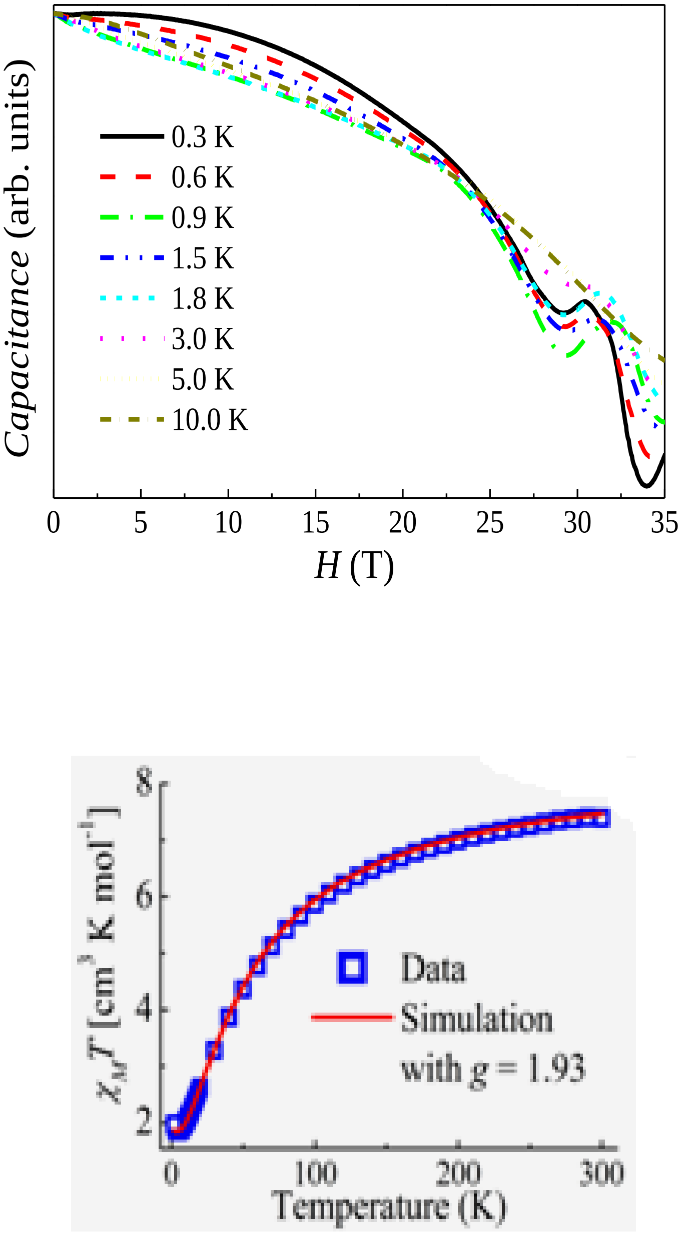

Figure 3-7: For the Mn_3Zn_2 molecule, a) Capacitance of the cantilever torquemeter as a function of temperature and magnetic field. The field sweep rate is 3 T/min. The change in capacitance is proportional to the magnetic torque on the sample. b) Display of experimental (from Ref. 20 and simulated temperature-dependent susceptibility data for a powder sample). For the simulated data the ZFS parameters inferred from the EPR analysis.

The search was conducted under a very restricted parameter space designed by several sources e.g. as mentioned before the susceptibility measurements and anisotropy values of similar compounds [75, 76]. Furthermore any unphysical parametric ranges were absolved by computing the magnetic dipole matrix elements for all ground state (lowest energy state) transitions i.e. using the α resonance matrix element to be approximately 2.5, a cutoff is enforced $2 > \langle m \mid S_x \mid m' \rangle > 0.03$. Hence the results portrayed in Figure 3-5 are a “best fit” for a broad range of experiments from DC magnetic to high frequency measurements. The best fit parameters are as follows: d = - 4.9 K, J_1 = 6.9 K, J_2 = 7.3 K and J_3 = 11.8 K. Many set of parameters were tried, but given the constraints mentioned above, these numbers were found to give a satisfactory explanation of the combined measurements. The calculated d value is a close match to values observed in the literature for the FM Mn_3Zn_2 and other analogous complexes. One should mention here that it is not possible to allocate the calculated J’s to the individual Mn . . . Mn contacts within the molecule [75,73]. In this project, the different J’s in terms of the structural information were not explored; however this investigation is a good motivation for future computational studies.

The exchange constants are also deduced from the computational fits of the magnetic susceptibility data $J_1 \approx 0$, $J_2 = J_3 = 10$ K [75]. These numbers are not exclusively mismatched with the earlier exchange constants but for consistency’s sake, the best fit ZFS parameters were used to simulate the temperature-dependent susceptibility of the powder sample. Figure 3-7 (b) shows the experimental and simulated data; a near perfect agreement of the exchange constants is achieved by reducing the g-factor by approximately 3% or lower over the expected value of about 2, thus giving $g = 1.93$. This reduction is relatively justified and not uncommon; as in the literature, materials are available where g-values are under reported by as much as 10%. This is probably a result of quantitative errors whose origin lies with the estimations of the absolute susceptibility; being sensitive to errors in accurate sample weight and solvent content after drying. The high point of this discussion is that when scaled vertically by the reduced g - value, the current simulation matches perfectly with the data, thus even if the absolute value is off by a few percent, the parameterization correctly captured the temperature dependence of the susceptibility data. It is worth mentioning that in our case where there is residual frustration in the cluster and there is not clear enough spacing of energy scales associated with the exchange and anisotropy, the fit of the susceptibility data becomes notoriously unreliable and one is left with not enough information from the susceptibility data [13] and a fit with too many variables.

The coupling constants in the broken C_3 symmetry of the triangle induce significant differences between the three exchange coupling constants. The difference between J_1 and J_2 is approximately 7 K; while J_3 is almost double, approximately 12 K. This difference in the three J's and the relative magnitudes of d, significantly affects the location of the spin moments on the individual Mn(III) sites within the molecule. This was further explored by computing the expectation values of $<m_i>$ and $<m_i^2>^{1/2}$ at the individual ions sites (i = 1-3). Specifically in the lowest energy molecular doublet $m_s = \pm 2$, the deviation of $<m_i^2>^{1/2}$ from 2.00 gives a measure of the spin delocalization in the system. The parameter set has, $<m_1^2>^{1/2} = 1.87$, $<m_2^2>^{1/2} = 1.98$, and $<m_3^2>^{1/2} = 1.85$, and the stronger exchange coupling constant J_3 couples spin 3 to spin 1. These numbers indicate delocalization weak entanglement between the strongly coupled spins 1 and 3, while spin 2 is almost completely localized along the z-axis. The entanglement between spins 1 and 3 can be understood in terms of J_3. An increase in J_3 results in an increase in entanglement between spins 1 and 3, meanwhile no significant change is observed in spin 2 i.e. $<m_1^2>^{1/2} = <m_3^2>^{1/2} = 1.62$ for $J_3 = 30$ K. However, an increase in localization between spins 1 and 3 is observed relative to the decrease in J_3 i.e. for $J_1 = J_2 = J_3 = 6$ K, we get $<m_1^2>^{1/2} = <m_2^2>^{1/2} = <m_3^2>^{1/2} = 1.95$. This happens because as the *Js* decrease, the Ising-type anisotropy ($d < 0$) dominates the Heisenberg interaction. Based on the information discussed above, it is safe to state that the unique low-temperature properties of the AF Mn_3Zn_2 complex arise from two important phenomenon: (a) The significant Ising easy-axis anisotropy ($d \approx J_i$) along with the parallel disposition of the Mn(III) Jahn-Teller axes, gives an approximately collinear display of spins in the ground state; (b) Existence of different exchange constants lift the frustration in the molecule, and the result is a low density of the ground states and hence a reasonably well-isolated ground state from the first excited state. Furthermore these factors are the underlying cause of the observation of magnetic hysteresis and high quality EPR spectra.

Also from giant-spin behavior of the ground state, it is observed that the expectation value of the states connected by the α resonance comes out to be approximately 2.5, a total spin not far from 2.0. In Figure 3-5 (b) the black curve is a fit of the five m_s states associated with the ground spin multiplet. Using a fourth-order polynomial for the fit, the calculated second and fourth order coefficients are -11.3 K and 0.785 K. One can treat these parameters as D and C in an effective spin Hamiltonian with fourth order term $H = DS_z^2 + CS_z^4$. The contribution of a considerable fourth-order term in the spectrum should not cause alarm when making direct comparisons with the usual Stevens operator formalism, as the magnitude of the estimated D value in this case is found to be 64% larger than as predicted from the strong exchange approximation discussed earlier. On the other hand, a closer look into Figure 3-5 (b) reveals that the 0 sublevel of the ground state multiplet is more strongly mixed than are the non-zero sublevels. We confirm this behavior (spin-state mixing) to be the origin of the fourth order term in the spin Hamiltonian [13]. Interestingly, discarding the m_s = 0 sublevel and fitting the non-zero sublevels using a second-order polynomial, results in a more reasonable D parameter ~ -7.35 K, and this value is only 6.5% larger than the value estimated earlier using the strong exchange limit approximation earlier. Hence it was successfully demonstrated that the ground state of the complex is reasonable, and has a spin equal to 2, either estimated by the strong exchange limit approximation or by giant spin approximation and that $\Delta\alpha$ corresponds to ZFS within this ground state. If we compare the matrix elements [calculated from the optimum parameterization discussed above] of the α resonance to those of the low temperature 'inter-spin-multiplet' transitions β and γ, a major reduction, more specifically a factor of 4 for the β and a factor of 2 for the γ resonances is observed. However, these matrix elements are extremely sensitive to even very small changes in the exchange parameters. Also a huge change is observed in these matrix elements when second order transverse anisotropy terms $e\ (S_x^2 - S_y^2)$ are introduced for the Mn(III) sites. Several attempts were made to play with the above mentioned parameters along with the single transverse anisotropy e. The result was a good overlay with the experiments i.e. comparable intensities for β and γ resonances and a stronger signal for α resonance were calculated. Following the same approach and within a factor of 5 to 10 of α, several higher-lying m_s = ± 1 states connected to the ground state by non-negligible matrix elements were calculated. Unfortunately these transitions [the first occur in the approximate 550 GHz range] were not observed in the EPR experiments as can be seen in Figure 3-3. One possibility is that the peak is buried under the noise at these high frequencies, i.e. the spectrometer is approaching the limits of its operating range for crystals of this size. One cannot rule out the possibility that since the second-order transverse anisotropy is included, the matrix elements can both decrease and increase and hence lead to relative high values.

3.4 Summary

These results provide the first pristine demonstration that the reduced symmetry of the AF Mn_3Zn_2 molecular nanomagnet relieves the spin frustration inherent in most other AF μ3-oxo-centered triangular Mn_3^{III} complexes. The result is a relatively isolated S = 2 ground state that experiences a very significant axial anisotropy due to the near collinearity of the JT axes on the three Mn(III) ions. A significant magnetization hysteresis is observed below a T_B of 0.8 K, the hysteresis indicates SMM behavior. And a spin-crossover transition is observed at high magnetic fields as predicted by preliminary simulations of the EPR data employing a multi-spin Hamiltonian. These detailed multi-frequency EPR measurements allow us to explore important comparisons between related FM and AF Mn_3 systems that had previously been lacking in the literature.

CHAPTER 4 SLOW MAGNETIC RELAXATION IN EXCHANGE-COUPLED COBALT SINGLE-CHAIN MAGNET

The work presented in this chapter has been done in collaboration with Dr. Stephen Hill from National High Magnetic Field Lab (NHMFL), Tallahassee and Dr. Eugenio Coronado from Instituto de Ciencia Molecular, Universidad de Valencia, Spain. The crystals were synthesized by Coronado’s group, EPR experiments were performed at the NHMFL in the EMR facility and the DC Hall-effect Magnetometry experiments were performed at UCF. The first half of this chapter is directly extracted, although conveniently modified from a published article as a result of this collaboration [A. Amjad, G. M. Espallargas, J. Liu, J. M. Clemente-Juan, E. Coronado, S. Hill and E. del Barco, Polyhedron, 2013].

4.1 Introduction

Single-chain magnets (SCMs) are potential candidates for ultra-high magnetic storage devices. Furthermore, 1D structures have proven to be extremely good candidates for probing and understanding exchange interactions in extended systems. Uniaxial anisotropic spin centers paired with strong magnetic correlations at first neighbors within the chain result in slow relaxation of the magnetization in these one-dimensional (1D) systems [27,28,30,86]. The magnetic dynamics of an ideal SCM is ascribed to the nucleation and motion of domain walls (spin-flips in the case of an Ising chain) that break the otherwise infinite chain into finite segments. An important factor controlling the dynamics of these extended systems reside on the manipulation and understanding of inter and intra- molecular interactions existing between and within the chains. Hence, research efforts have been focused in the synthesis of chains with weak inter-chain couplings to achieve one–dimensional systems [21,32,87]. Following the same thought process, recently, single-ion cobalt-based SCMs with halogenated axial ligands, which lead to the organization of linear cobalt chloride chains *via* halogen bonds, have been synthesized in order to study the possibility to tune the inter-chain interactions and modify the metamagnetic properties of the system [88].

Two SCM compounds of formula *trans*-$[CoCl_2(3,5\text{-}X_2py)_2]$ [88], where py is pyridine and halogens $X = Br$ for sample (**1**) and $X = Cl$ for (**2**), have been studied in this work. The compound forms single crystals composed of four chains per unit cell, running parallel to the crystallographic *c* axis, as shown in Figure 4-1. The chains are formed by Co^{II} ions (effective spin $S = ½$) as the magnetic core, lying at the intersections of three 2-fold symmetry axes and each attached to two pyridines via their nitrogen. The Cobalt (II) sits in octahedral symmetry, ideally a Co when in an octahedral position, has ground state $^4T_{1g}$, with a corresponding anisotropic Kramer's doublet as a result of crystal field and spin orbit coupling effects, hence resulting in an effective spin $S = ½$ system [48, 89,90]. If the thermal population is restricted to the lowest Kramer's doublets, the magnetic anisotropy in the system is renormalized within an anisotropic *g* tensor. The Co…Co distances within the chain lead to ferromagnetic exchange interactions within the chain as evidenced by high temperature ($T > 2$ K) susceptibility measurements [86].

In this section we present EPR studies on the complex with the Br halogen (**1**) demonstrate that the system behaves as a collection of finite SCMs at temperatures below 2 K. In addition, ac and dc magnetometry studies have been performed in both complexes. The results show that complex (**1**) develops 3D dynamics at low temperatures. Published dc susceptibility measurements $\chi_m T$ showed that ferromagnetic intra-chain interactions develop through the μ_2-Br bridges, whereas comparatively weak antiferromagnetic interactions exist between the chains in the unit cell.

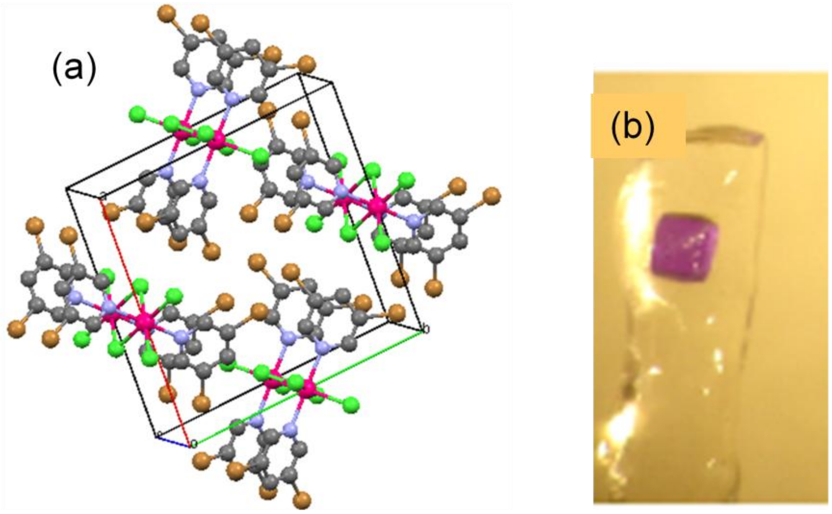

Figure 4-1: a) A unit cell of the trans-[$CoCl_2(3,5\text{-}Br_2py)_2$] SCM structure with chains running parallel to the c-axis. Cobalt (deep pink), bridging chlorine (green), nitrogen (blue), carbon (grey) and Bromine (gold). b) Placement of the crystal on the EPR quartz pillar in such a way that the direction of the applied magnetic field is along the crystal's long axis.

4.2 Single crystal electron paramagnetic resonance (EPR) spectroscopy

The magnetic dynamics in SCMs at a finite temperature follows the Arrhenius law, where the relaxation rate is given by $\Gamma = \Gamma_0 \exp\left(-\frac{\Delta}{k_B T}\right)$, with Δ accounting for the activation barrier associated to the creation of a magnetic wall, which will then propagate within the chain leading to its full magnetization reversal. This barrier is determined by Δ_A: a) the energy to reverse a single spin over the anisotropy barrier resulting from the spin-orbit interaction, $\Delta_A = DS^2$ (for integer spins), where D is the zero-field splitting parameter; and, b) the correlation energy, Δ_{ξ}, which is the energy necessary to overcome the intra-chain exchange interactions, and, in the Ising limit and assuming a $-JS_1S_2$ type exchange interaction between first neighbors, is given by $\Delta_{\xi} = 2|J|S^2$. Note that the energy required to create a magnetic domain is larger in the case of infinite chains ($\Delta = \Delta_A + 2\Delta_{\xi}$), since the formation of two domain walls is necessary. However, in real samples, chains present finite lengths due to the presence of crystalline defects, whose concentration ultimately determines the maximum average length of the magnetic domains. In the latter case, a smaller activation energy ($\Delta = \Delta_A + \Delta_{\xi}$) is required, since a single nucleation occurs at the end of the chain. In fact, the two scenarios can be found in the same sample at different temperatures [91,92], since the correlation length (length of a domain) depends exponentially on temperature. For high temperatures, where the correlation length is smaller than the average distance between defects, the system behaves as composed of infinite chains. As the temperature is decreased, the increasing correlation length will eventually be limited by defects and the system will behave as a set of finite chains. The nucleation and motion of the domain walls dictate the magnetic dynamics of a SCM. Note that, once created, the domain walls can move within the chains at no energy cost [4].

In this work we investigate the effect of strong ferromagnetic intra-chain interactions on the cooperative magnetic properties of the Co-based one-dimensional system. For high-field EPR measurements, complex (**1**) was mounted on a quartz pillar perpendicular to the cavity base at the end of the EPR probe. In this geometry, the long physical axis of the crystal is aligned almost parallel to one of the axes of application of the magnetic field, initially the *z*-axis shown in Figure 4-1 (b). The experiments were carried out over a wide range of frequencies (50 to 400

GHz) and temperatures (2 to 35 K). Initially, the anisotropic nature of the chain was probed via EPR measurements by rotating the applied magnetic field away from the *c* axis. The magnetic field is rotated over 180 degrees at 20^0 increments in two orthogonal planes parallel to the lateral crystal planes. The first rotation $\varphi = 0$ as shown in Figure 4-2(a) corresponds to rotation in one of the planes of the crystal, which corresponds to the *zx* laboratory plane. The spectrum observed at a fixed strong mode 72.6 GHz shows strong resonances at the lowest temperature of 2K as shown in the top part of Figure 4-2(b), this spectra is obtained for field applied almost 20^0 from the *c* - axis. Multiple peaks are seen at this temperature, but the main part of Figure 4-2(b) shows the angular modulation of only the lowest four resonant fields (black, red, green and blue squares in the inset). These resonances are especially highlighted as they survive at all orientations of the magnetic field in the *xz* plane, whereas the rest tend to slowly vanish and reappear at certain applied field orientations.

The angle dependence reveals that all four resonances share the same minimum at field parallel to the *c* axis, while the peak positions move to higher fields, reaching a maximum at 1.9 T (for the lowest field resonance indicated by black squares) when the field is transverse to the *c* axis. The solid line is a fit using a simple angle dependence of the form $B_{min} + \delta B\cos^2\theta$, where B_{min} is field value at the minima, δB is the difference between the maxima and minima resonant field values and θ is the angle of application of the magnetic field with respect to the *z* axis [93].

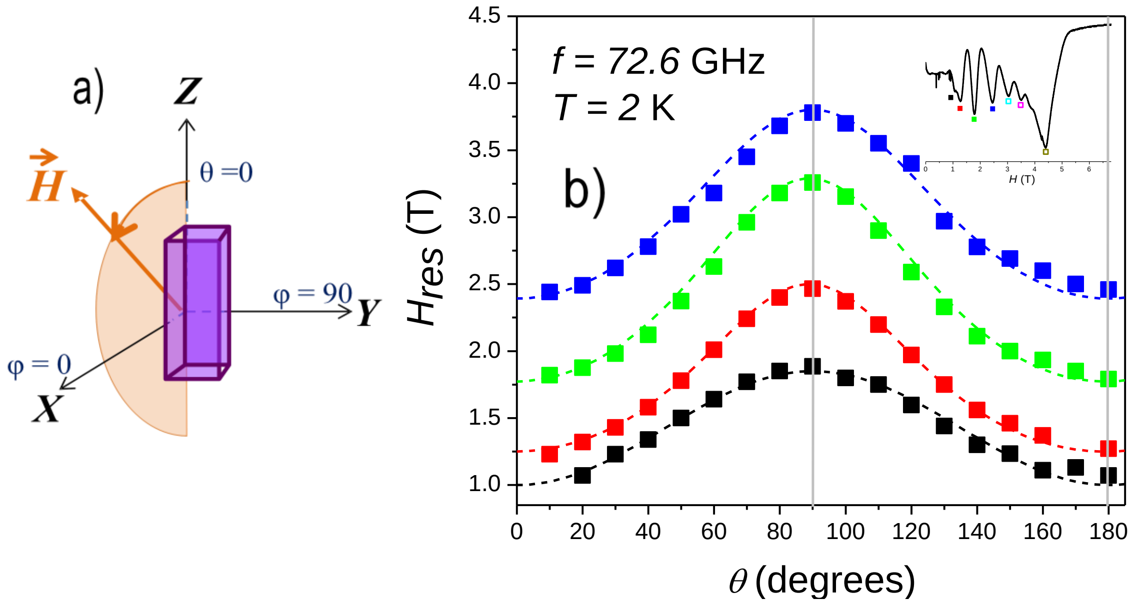

*Figure 4-2: a) A geometrical representation of initial placement of the complex (**1**) crystal in a magnetic field and the active rotation plane. b) Field positions of peaks in the EPR spectra versus θ, angle representing field rotation in the zx plane. The starting angle is referenced to the crystallographic c-axis as shown in part (a) of this Figure. Inset: EPR spectra observed at 2 K for a frequency of 72.6 GHz.*

Figure 4-3(a) shows plots of the peak positions of the resonances as functions of the microwave frequencies obtained at 2K. These data were collected with the magnetic field applied parallel to the *c* axis of the crystal, i.e. at the minima of the angle dependent graph. As mentioned above although there are clearly more resonances but they are harder to resolve particularly close to the highest field resonance as seen in Figure 4-3(b) as well. Furthermore the peaks seem to get closer to each other as the field increases, with more and not well resolved peaks above $H = 4$T which appear to collapse in a single broad peak at $H \sim 4.6$ T. The frequency behavior can be well followed for most of the peaks, as shown in the dotted data in Figure 4-3 (a). The positions of the peaks corresponding to the spectrum in the bottom of the Figure are color coded (solid squares) and straight lines of the same color are used to guide the eye in following the behavior of most of the peaks. Note that some peaks are not easy to follow at high frequencies (dashed lines) since the EPR spectra are not equally clear for all the resonant modes of the cavity employed. From the slopes of the lines, we extract *g*-factors lying in the range between 4.5 and 4.9 for the observed peaks. In particular, from the slope of the first absorption peak (black straight line in Figure 4-3 (a)) we extract the longitudinal *g*-factor, $g_{//} = 4.9$.

Figure 4-3 (b), display the temperature dependencies of the EPR spectra obtained at 72.6 GHz with the crystal's crystallographic *c* axis parallel to the applied magnetic field. Exactly eight resonance modes are observed at the lowest temperature 2 K. As the temperature increases the intensity of the absorptions decreases, with the peaks completely vanishing one by one above $T \sim 5$ K, starting from the one at the highest field (~ 4.6 T, golden square). For temperatures above ~ 20 K only the lowest field peak survives (~ 1 T, black square). The origin of this behavior is discussed later in the text.

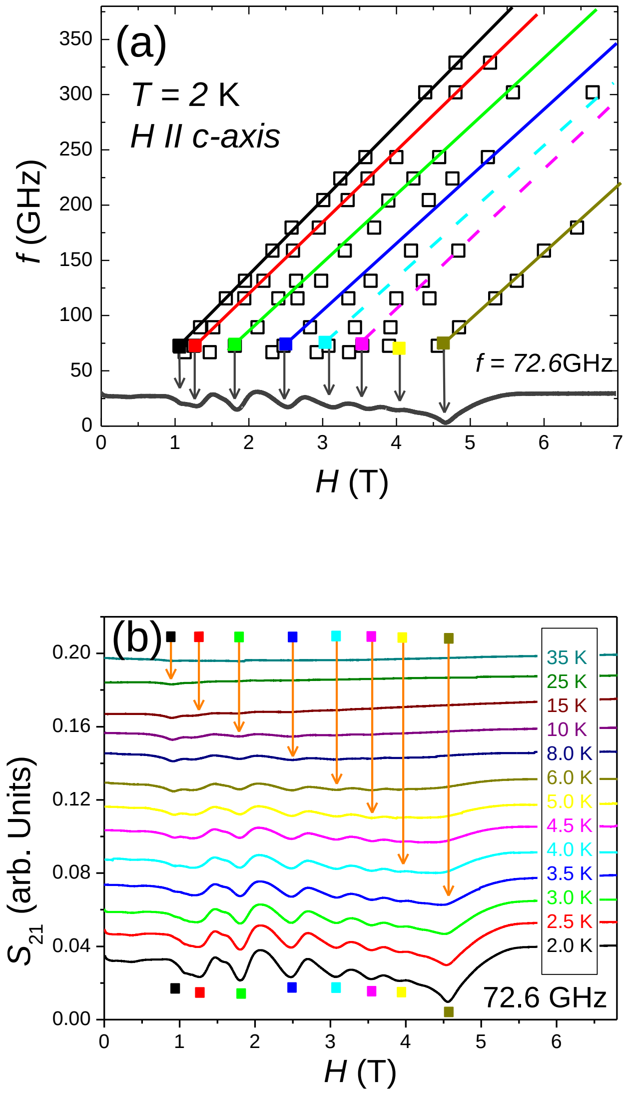

Figure 4-3: For the -[CoCl$_2$(3,5-Br$_2$py)$_2$] SCM a) At 72.6 GHz, EPR spectrum obtained at T = 2 K with the field applied along the axis of the molecular chains (lower part of the figure). In this orientation, the frequency dependencies is shown (open squares), with those obtained at 72.6 GHz highlighted as solid squares with the same color as that of the straight lines used to guide the eyes in following the behavior of most of the peaks. b) Temperature dependence of the peaks observed at the same frequency and field orientation as part (a).

Variable frequency and temperature measurements were also performed at the orientation depicting the maxima in the angle dependencies, i.e. applied field parallel to the *x*-axis. Unlike the minima, at this orientation only four peaks are observed, as shown in the bottom of Figure 4-4(a), however more peaks appear at intermediate frequencies and they tend to disappear again at higher frequencies. The field values represented by open black squares of all peaks observed in 50 to 250 GHz range are shown in main part of Figure 4-4(a). The colored lines matching the color coded resonances are just an indication for the eye to highlight the behavior of the peaks. Measurements with the field applied perpendicular to the *c* axis give $g_{\perp} = 4.3$, illustrating the anisotropic nature of the system. The extracted values of the anisotropic *g*-factor ($g_{//} = 4.9$, $g_{\perp} = 4.3$) also lie in the vicinity of those extrapolated from the fitting of the susceptibility data. The temperature dependence of the EPR spectra obtained at 72.6 GHz with the crystal's crystallographic *c*-axis transverse to the external field is shown in Figure 4-4 (b). As shown earlier, only four absorption peaks are observed at the lowest temperature (~ 2 K). The resonances intensities decrease systematically with the increase in temperature, in a similar way that is previously discussed.

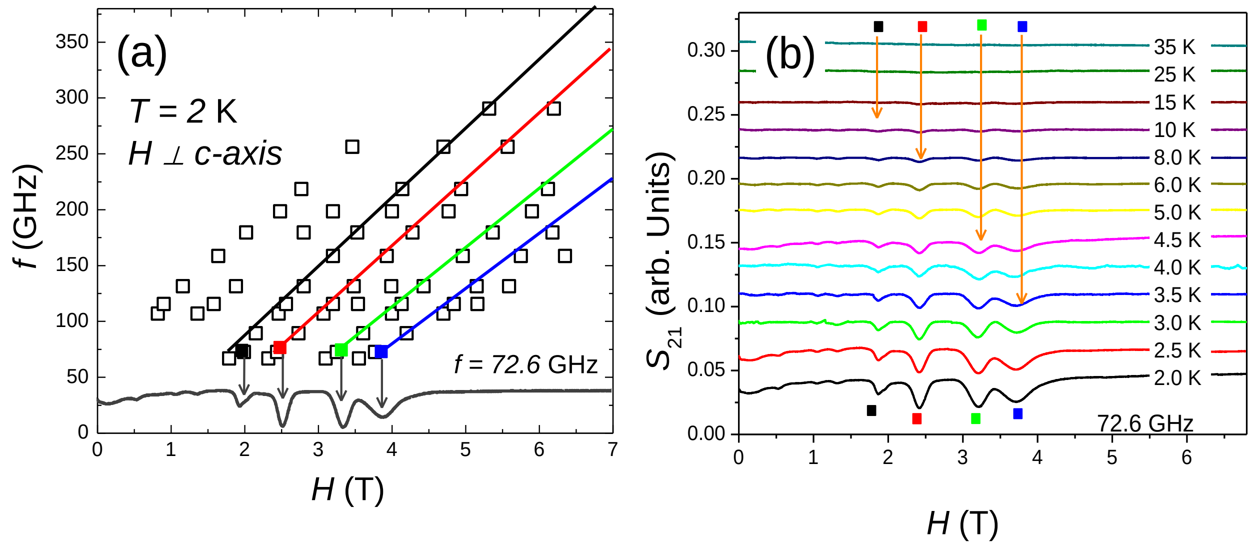

Figure 4-4: a) 2D plot of the magnetic field values of the EPR peaks of the -[CoCl$_2$(3,5-Br$_2$py)$_2$] chain (open squares) obtained at different frequencies. B) V-band (72.6 GHz) EPR spectra versus the magnetic field obtained at different temperatures.

The second set of rotation data is collected by rotating the field within the *yz* plane, Figure 4-5 shows the angular behavior of the four lower field resonances, displaying similar behavior as observed for the angular modulation in the *yz* plane. Minima of the peak positions are observed for the field along the *z* axis. Based on the two rotation sets we conclude that the minima at zero degrees correspond to the easy axis of the sample, which in this case is the physical long axis of the chains, i.e. the crystallographic *c* axis, while the *xy* plane (i.e. the *ab* plane) is the hard plane.

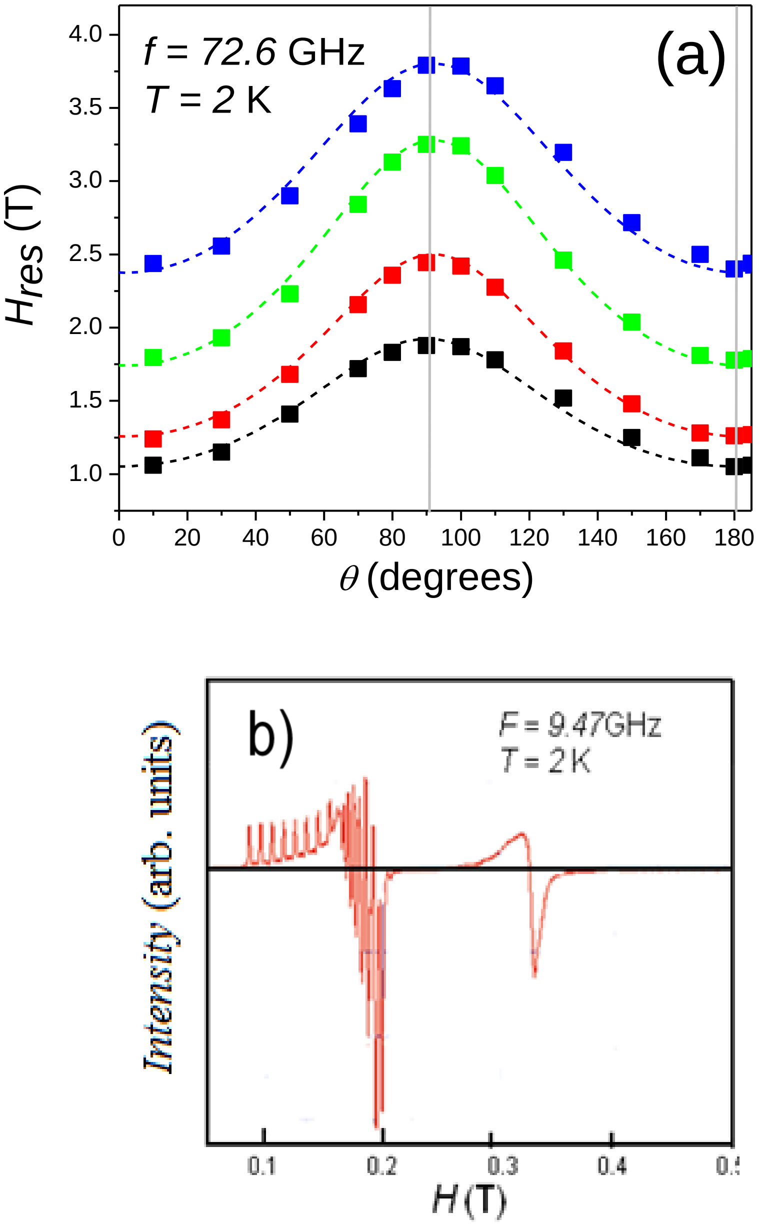

Figure 4-5: a) Angle dependence EPR peaks of [CoCl$_2$(3,5-Br$_2$py)$_2$] chain, observed at 2 K for a frequency of 72.6 GHz. The data displayed is for a field rotation in the bc plane of the crystal. b) EPR spectrum obtained at T = 4 K in a powder sample of cobalt-diluted crystallites at 9.47 GHz.

Hence the two-fold angular modulation of the EPR spectra is indicative of strong uniaxial magnetic anisotropy. Furthermore, this spin anisotropy is also seen in the EPR spectrum obtained in a diluted powder sample as shown in Figure 4-5(b), which gives the values g_1 = 5.55, g_2 = 3.75 and g_3 = 2.04 for the individual cobalt ions. The anisotropic g values extracted from the experimental data, the susceptibility fits and the EPR results of the diluted sample lie in close agreement to one another.

4.2.1 Correlations versus thermal fluctuations

The temperature behavior at both axial and transverse field orientations can be interpreted in terms of a competition between intra-chain correlations due to exchange coupling between the Co(II) ions and thermal fluctuations of the spins within the chains. At high temperature ($T >> J$), thermal fluctuations overpower the correlations between neighbors in the chain, and the Co^{+2} ions behave nearly as independent anisotropic spins (S = 1/2), barely noticing the other ions in the vicinity. This would correspond to the peak observed at the lowest magnetic field (Figure 4-3 (b)), whose behavior should be similar to that observed in the diluted powder sample (Figure 4-5 (b)). In fact, this peak that appears at ca. 1 T and roughly corresponds to that calculated from the single-ion g_1-value (0.94 T) extracted from measurements in the diluted sample. Note that this EPR excitation passes closest to the origin of the frequency vs. field plot shown in Figure 4-3(a) (black straight line), indicating that single Co ions are the basic anisotropic entities within the chains, as observed also in the weaker angular modulation of this resonance (black data in Figure 4-2 (b)). As the temperature decreases, correlations between neighboring spins start to develop and the chains start to behave as collections of independent segments (domains) of different length, with an average length inversely dependent on the experimental temperature. Segments composed of two spins would form first, while longer segments with three, four, five and more spins will appear as the temperature continues to decrease. The zero-field splitting (intercepts in Figure 4-3 and 4-4 (a)) cannot be a property of the isolated Co (II) ions, or that of a collection of exchange-coupled Heisenberg spins. Therefore, the anisotropy has to arise from pairwise anisotropic (non-Heisenberg) exchange interactions, as also inferred from magnetic studies. In other words, the zero-field anisotropy (i.e. the observed zero-field splitting) is an emergent property arising from the correlations that develop among the spins within a chain, and is not associated with the individual effective $S=1/2$ spins. As a consequence, different EPR resonances should appear at different magnetic fields for each temperature, increasing in value as the correlation length increases. However, the resulting anisotropy energy is not expected to grow indefinitely as the correlation length diverges, but to converge to a bulk ferromagnetic resonance mode determined by the saturation magnetization of the sample. This explains the observation of the reducing magnetic field spacing between the EPR resonances and the final collapse into a single broad peak at the highest field position, which survives at the lowest temperature. Indeed, the spacing between the first two peaks (black and red squares in Figure 4-3) is smaller than the subsequent ones. However, these two peaks are different in origin. The first peak corresponds to the individual Co ions, while exchange anisotropy only plays a role starting at the second peak, associated to domains of two or more ions coupled together. This distinct behavior of the first peak can also be noticed in its weaker angular modulation in Figure 4-2(b).

4.3 DC and AC magnetometry studies at low temperatures

The role of intra-chain interactions and their intrinsic 1D magnetic nature differentiates SCMs from their close zero-dimensional (0D) relatives, i.e. the SMMs [16,22,24,21]. However, both systems share a common fact that three-dimensional (3D) interactions may interfere with the low-dimensional magnetic dynamics. In practice, in a single crystal of SCMs, and of SMMs for that matter, three-dimensional ordering is an irrevocable consequence of the small inter-chain (inter-molecule in SMMs) interactions, both short (exchange) or long range (dipolar). The question is the temperature below which the 3D ordering appears, the lower the temperature, the weaker the inter-chain interactions are. It is for these reasons that one frequent criterion followed in synthesizing SCMs involves subduing inter-chain interactions, which among other things may reduce the magnetic bistability of the chains. Indeed, 3D ordering in SCMs systems may enable hard magnetic behavior (high coercivety) capable of competing with the best current intermetallic compounds used for permanent magnets (e.g. SmCo, NdFeB alloys), this explains independent efforts to enhance the inter-chain interactions in this class of systems. In any case, since a pure 1D magnetic system only exhibits long range order as $T \rightarrow 0$, understanding the magnitude and origin of inter-chain interactions while maintaining the intra-chain coupling strength is crucial for the future development of the field [32,50,94].

One synthetic technique to tune the interactions between chains in a crystal of SCMs consists of covering the inner magnetic core with non-magnetic organic ligands to modify the inter-chain metal connections [21,87]. In this section, we present ac and dc susceptibility studies of two $\mathrm{Co^{II}}$-based SCM systems purposely synthesized with different ligands in order to vary the interactions between neighboring chains within the crystal. An occurrence of 3D dynamics occurs at temperatures below 0.45 K in sample (**1**), while no such behavior is observed in sample (**2**) down to the lowest temperature achieved in the experiments (34 mK). Interestingly, a crossover between 1D and 3D magnetic dynamics can be induced, by varying the sweeping rate of the applied magnetic field. The exclusive “visco-magnetic” (in a parallelism to visco-elastic) behavior observed in this SCM compound may lead to novel applications in where the magnetic response of a device changes attending to the characteristic time of the input.

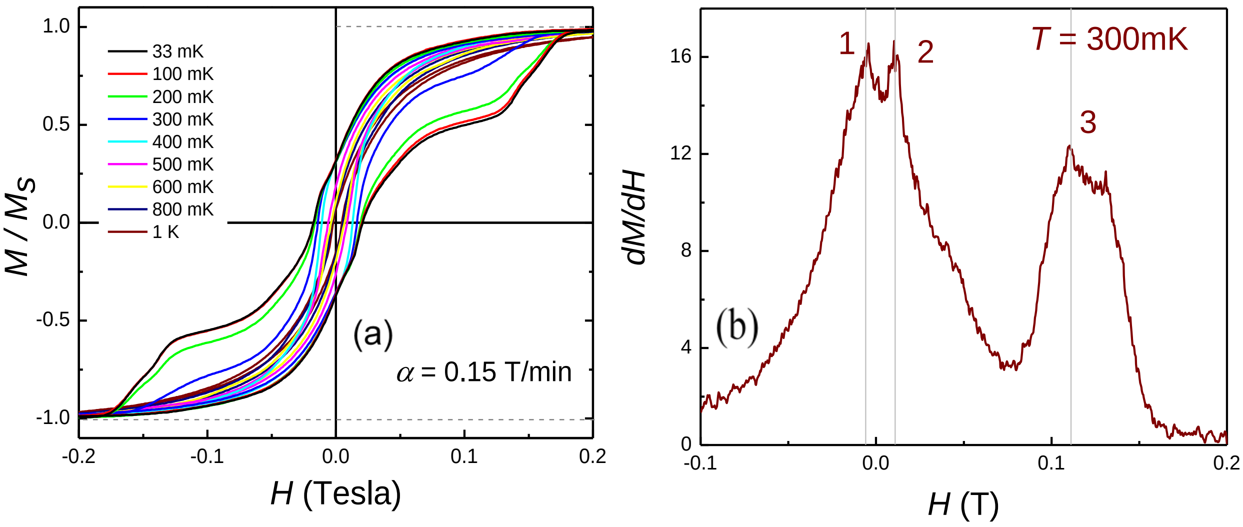

Figure 4-6: a) Hysteresis loops recorded on a single crystal of trans-[$\mathrm{CoCl_2(3,5\text{-}Br_2py)_2}$] SCMs at different temperatures. The single crystal of $\mathrm{Co^{II}}$ SCMs was placed on top of a micro Hall-effect sensor with the crystallographic c axis (direction of the chains) parallel to the sensor plane and to the main magnetic field of the superconducting vector magnet employed in the study. b) The field derivative of the magnetization at 300 mK, highlighting the three peaks characteristic of the distinct magnetic dynamics in this sample, as discussed in the text.

Figure 4-6 (a) shows Hall-effect magnetometry results obtained on a single crystal of sample (**1**) at low temperatures ($T = 0.034 – 1$ K), sweeping the magnetic field at a constant rate of 0.15 T/min. The hysteresis is observed with the magnetic field applied along the crystallographic *c*-axis. Clear hysteresis loops, shrinking as the temperature increased, identify the behavior of this compound as a molecular magnet. No hysteretic behavior is observed at T = 4.2 K (not shown).

Similar measurements carried out on sample (**2**) show hysteretic behavior with much narrower loops and a coercive field ~0.01 T at the lowest temperature (not shown). The hysteretic behavior in this sample is not simple, as can be clearly observed in the non-monotonous shape of the hysteresis loops. Figure 4-6 (b) shows the field derivative of the magnetization at $T = 300$ mK. For this temperature and sweep rate the hysteresis shows three distinct peaks, which are associated to three different relaxation dynamics in this sample. It will be shown later that peaks 2 and 3 are associated with 1D and 3D magnetic dynamics, respectively, while peak 1 corresponds to the zero-field susceptibility, which decreases when increasing temperature. Actually, the analysis of peak 1 as a function of the angle of the application of the external magnetic field can be used to determine the orientation of the magnetic symmetry axis of this sample.

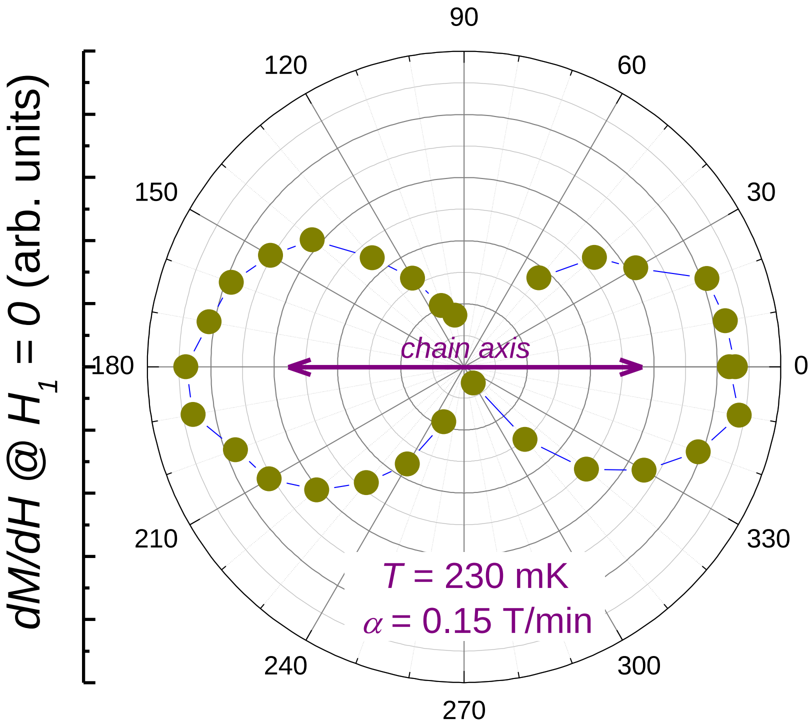

Figure 4-7: Angle dependence of the zero-field susceptibility of the Co SCM with Br calculated from the field derivative of the magnetic hysteresis obtained at 230 mK, with the field rotation in the ac plane. The starting angle corresponds to the magnetic field applied along the long axis of the crystal (c axis).

Figure 4-7 presents a polar plot showing the modulation of the zero-field susceptibility (i.e. height of peak 1) at 230 mK as a function of the angle of application of the magnetic field with respect to the crystallographic *c* axis. An angle increment of 10 degrees was used. Considering a good physical alignment between the field and the crystal axes (±5 degrees error), the observed 2-fold modulation, with minima along 90^{o}-270^{o} and maxima along 0-180^{o}, provides evidence for a magnetic symmetry axis directed along the crystallographic *c* axis, i.e. the magnetic easy axis lies parallel to the chains (long crystal axis).

4.3.1 Three-dimensional magnetic transition

The dependencies of the dM/dH maxima (peaks 1-3 in Figure 4-6 (b)) as a function of temperature are shown in Figure 4-8. Obviously, peak 1 (the zero-field susceptibility) does not change. Peak 2 decreases slightly as the temperature is raised. As mentioned above, this peak relates to 1D hysteretic dynamics intrinsic to the SCMs and survives at high temperatures ($T > 1$ K), and will be discussed in the following section. We focus here on the distinct temperature behavior of peak 3, which appears only below 0.45 K and whose field position quickly grows with decreasing temperature until saturating at $H_{max} = 0.14$ T. This behavior is characteristic of a magnetic dynamics transition, with the transition parameter vanishing at the transition temperature, $T_c = 0.45$ K, which we associate with three-dimensional magnetic correlations as a result of weak inter-chain exchange interactions. We exclude dipolar coupling as a possible cause since this 3D behavior is not observed in sample (2), which displays almost identical structural characteristics.

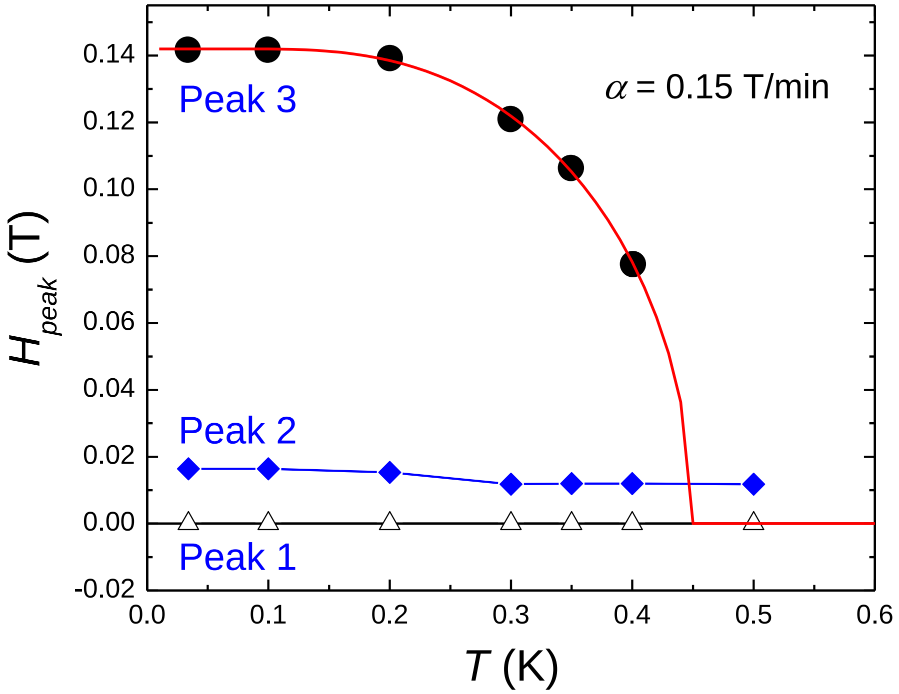

Figure 4-8: The magnetic correlations observed at 0.15 T/min magnetic field sweep rate in the trans-[$CoCl_2(3,5\text{-}Br_2py)_2$] chain. The symbols indicate the position of the peaks observed in the field derivative of the magnetic hysteresis loops of Figure 4-6 (b). The solid red line is the theoretical mean-field magnetization, assuming the chains behave as Ising spins (see text for details).

A quick estimate of the magnitude of the inter-chain exchange interactions giving rise to the 3D dynamics observed in this sample at low temperatures can be obtained using mean-field theory assuming the chains are represented by Ising spins. In this case, the reduced magnetization parameter $m = M/M_s$ is given by $m = \tanh(mJ_{inter}/k_BT)$. Since the magnetization value at a given field is directly related to the coercive field (represented by peak 3 in this case), the data in Figure 4-8 is directly fitted with the same model, multiplying m by the saturation coercive field $H_{peak} = 0.142$ T (continuous red curve in Figure 4-8). The result gives

J_{inter} = 0.45 K, which is substantially weaker than the exchange interaction between cobalt ions within a single-chain, J_{intra-} ~ 7 K, as expected from high-temperature susceptibility measurements [88].

The slow relaxation of the magnetization is further explored with zero-field-cooled (ZFC) and field-cooled (FC) experiments at a fixed magnetic field applied along the easy axis direction (parallel to the chains). In the ZFC measurement, the sample is cooled down to 34 mK in the absence of a magnetic field. At the lowest temperature, a measuring field is applied and the temperature is increased to 1.4 K while the sample magnetization is monitored. Subsequently, the sample is cooled again without eliminating the measuring field, i.e. the FC measurement. Figure 4-9 shows the ZFC-FC magnetization obtained in the presence of a measuring field H_{ZFC-FC} = 50 G (lower panel). A clear departure between the ZFC (solid purple circles) and FC (open dark yellow circles) curves occurs below T_c ~ 0.45 K, coinciding with the 3D transition temperature extracted from the magnetic hysteresis.

ZFC-FC measurements were carried out for different values of the measuring magnetic field. Figure 4-9 (b) shows the dependence of the transition temperature with the measuring field, decreasing slowly as the field increases until abruptly vanishing (not observable at T > 34 mK) for fields over ~ 0.14 T, which coincides with the saturation coercive field observed in the magnetic hysteresis (solid circles in Figure 4-8). This is indicative of the common origin of the blocking temperature observed in the ZFC-FC experiments and the transition temperature observed in the hysteresis measurements. In both cases, the abrupt disappearance of the slow relaxation dynamics (hysteretic behavior) with field and temperature indicates collective behavior as the most likely source.

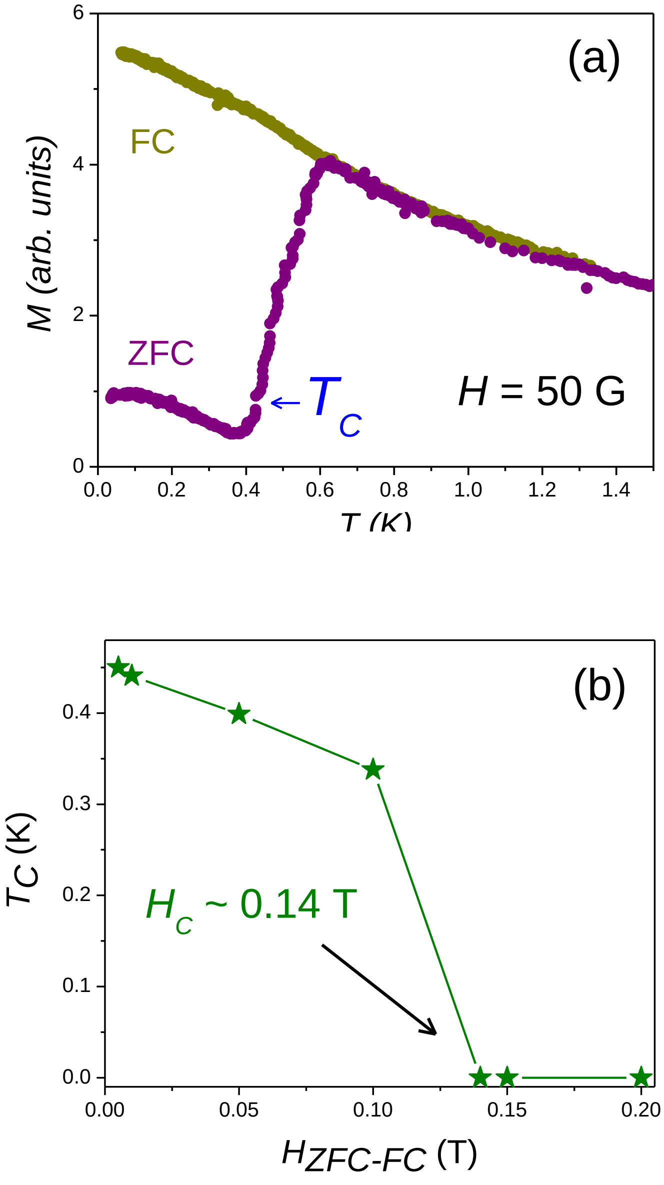

Figure 4-9: a) *ZFC-FC magnetization versus temperature measurements of the single crystal of -[CoCl$_2$(3,5-Br$_2$py)$_2$] chain in the presence of a measuring magnetic field H_{ZFC-FC} = 50 G.* b) *Behavior of the transition temperature as a function of the field applied for the ZFC-FC measurements. A critical field H_c ~ 0.14 T is observed, coinciding with the saturation field position of peak 3 in the hysteresis loops.*

As mentioned above, we associate this behavior with three-dimensional magnetic correlations due to exchange interactions between different chains in the crystal. Further evidence of this transition is given by ac susceptibility measurements (discussed in the following section), where a small bump in $\acute{\chi}$ is clearly observed at $T = 0.45$ K (see Figure 4-10 (a)).

4.3.2 One-dimensional dynamics

Above the 3D correlations temperature, $T > 0.45$ K and up to temperatures around 2 K, sample **1** shows simpler hysteresis loops in where only peaks 1 (zero field) and 2 are observed as seen in Figure 4-6 (a). The slow dynamics for fields below the coercive field represented by peak 2 and above the transition temperature must be associated with intra-chain relaxation processes (1D dynamics). Figure 4-10 (a) and (b) show the in- and out-of-phase susceptibilities recorded at different frequencies as a function of temperature. One main peak is observed in the out-of-phase susceptibility at 1.5 K, and a smaller one appears around 2 K. These two peaks should be related to two characteristic relaxation processes within the chains, with the latter becoming dominant for high frequencies. There is a third peak observed at 3.5 K and we have already mentioned a third and smaller peak at 0.45 K which we associate to the 3D magnetic dynamics in sample (**1**). Although we do not have a complete understanding of the distinct relaxation processes observed in the ac susceptibility (peaks at ~1.5, ~2 and 3.5 K), they may be related to the particular arrangement of the Co ions in neighboring chains, being orthogonally oriented within the bc-plane, i.e. the plane perpendicular to the chain axes (see Figure 4-1 (a)), and or to transitions between different relaxation regimes governed by different activation energies.

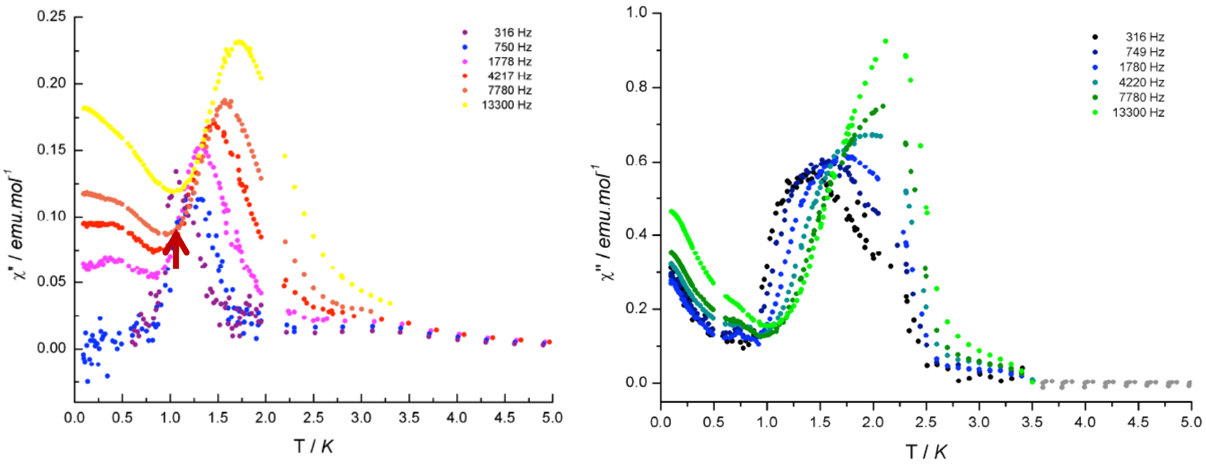

Figure 4-10: a) In-phase and b) out-of-phase susceptibilities of [CoCl$_2$(3,5-Br$_2$py)$_2$] SCM obtained at different frequencies as a function of temperature.

From measurements on a powder sample in the temperature range 2-20 K, the χT product follows an exponential behavior with T^{-1}, particularly $\ln\left(\frac{\chi T}{C}\right) = 4JS^2/k_BT$), where C is the curie constant ($\frac{g^2\mu_B^2S^2}{k_B}$) as expected from a ferromagnetic ID anisotropic Heisenberg system in the Ising limit. Fitting of the data with a close-chain computational procedure with 10 centers indicates FM coupling between the Co ions within the chains, with anisotropic exchange couplings $J_{//}$ = 7 K (along the chain) and $J_\perp$ = 3.8 K (perpendicular), as well as g-tensors $g_{//}$ = 4.8, $g_\perp$ = 3.5 [88]. Using these parameters, the activation energy to form a domain wall in the chain would be $\Delta_\xi = 2J_{//}S^2$ ~ 3.5 K, which is the temperature below which the susceptibility shows the main peaks. Indeed, the relaxation above 2 K does not follow a single linear behavior, as can be inferred from the slight bump in the susceptibilities around 3.5 K. This switch of the 1D relaxation dynamics can be related to a change in the activation barrier when the correlation length, which grows when decreasing temperature, is eventually saturated by defects in the crystal breaking the infinite chains into finite magnetic domains (as was observed in EPR studies of this sample shown earlier). The extracted values for sample **2** are similar, indicating that both compounds are composed of comparable SCMs. However, sample **2** does not show 3D magnetic dynamics down to the lowest temperature available in the magnetization experiments (34 mK), which we attribute to a different interactions between the chains as a result of the different ligands employed in the synthesis. Table 4-1 displays the characteristic parameters of the two samples as extracted from x-ray diffraction and susceptibility measurements.

Table 4-1: Structural comparison of the two halogen, cobalt-based chain [$CoCl_2(3,5\text{-}X_2py)_2$*]s. Structural parameters are obtained from x-ray diffraction studies while the exchange couplings and the g-tensors are extracted from susceptibility measurements [88].*

	(**1**) X = Br	(**2**) X = Cl
Space group	Tetragonal (*p*4*b*2)	Tetragonal (*p*4*b*2)
a=b (Å) c(Å)	13.7871(10) 3.7439(6)	13.7352(11) 3.6340(4)
Co…Co intra-chain distance (Å)	3.7439(6)	3.6340(4)
Inter-chain distance (Å)	9.7490(7)	9.7123(8)
Halogen bond strength R	0.969	1.070
$J_{\|\|}$ (cm^{-1})	4.9	3.9
$J_{\perp}$ (cm^{-1})	2.6	1.6
$g_{\|\|}$	4.8	6
$g_{\perp}$	3.5	3.8

4.3.3 Crossover between 1D and 3D dynamics

Once the two main relaxation dynamics of sample (**1**) have been identified, i.e. 3D magnetic dynamics below 0.45 K as a result of weak inter-chain exchange interactions and 1D dynamics associated to propagation of domain walls within the chains, we now focus our attention on the remarkable possibility to transit in between the two mentioned regimes just by tuning the sweep-rate of the applied magnetic field. Figure 4-11 shows magnetic hysteresis loops obtained at 34 mK (well below the transition temperature) obtained at various field sweep rates ($\alpha = dH/dt$) from 0.05 T/min to 0.45 T/min. The hysteresis is strongly field sweep rate dependent. For convenience, the three interesting phenomena discussed above are highlighted as 1, 2 and 3 in Figure 4-11 (in relation to the corresponding peaks in the dM/dH in Figure 4-6 (c)). At the lowest sweep rate (black curve in Figure 4-11), the magnetization only shows signs of peaks 1 and 3, the zero-field susceptibility and the 3D dynamics process. Peak 2 highlighted by a rectangle, related to intra-chain 1D dynamics, is completely absent. As the sweep rate is increased, signs of 1D dynamics (peak 2) start to emerge, while the slow 3D dynamics (large hysteresis delimited by peak 3) faints, eventually vanishing for rates over 0.25 T/min, for which peak 2 dominates the slow magnetic relaxation without any further changes at higher sweep rates.

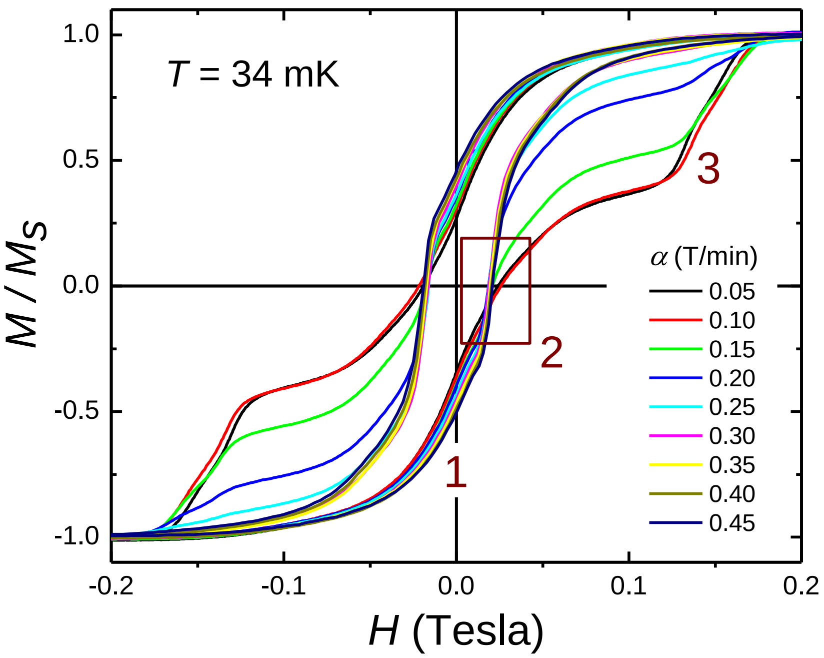

Figure 4-11: Magnetic hysteresis loops observed in [$CoCl_2(3,5\text{-}Br_2py)_2$] SCM at 34 mK, as a function of magnetic field sweep rate, with the magnetic field along the crystallographic c axis.

The crossover between the two regimes is more clearly observed in Figure 4-12, where the magnitude of the three dM/dH peaks is plotted as a function of the field sweep rate at 34 mK. Note that the fading of peak 3 as peak 2 emerges does not imply that the source of 3D dynamics is absent, since the inter-chain interactions remain intact and the temperature of the experiment is well below the transition temperature. Indeed, it is a direct consequence of the 1D dynamics taking over the relaxation at high sweep rates and making the magnetization to avoid overcoming the 3D interactions. In other words, below the transition temperature and provided there is enough time for the system to equilibrate during relaxation (slow sweep rates), the inter-chain interactions will fully develop and keep the system correlated until the corresponding reversal field ($H = 0.14$ K at 34 mK), when the Zeeman energy overcomes the inter-chain coupling. However, if the field is swept at a fast rate, faster than the characteristic rate of the 3D dynamics, the intra-chain dynamics prevents the system from developing 3D correlations.

The critical sweep rate, above which the 1D dynamics start governing the relaxation (the appearance of peak 2 in Figure 4-12), is $\alpha_c \sim 0.1$ T/min. Attending to the parameters used to fit the high temperature susceptibility data, this rate corresponds to a critical energy rate of $\frac{dE_c}{dt} = g\mu_B S\alpha = 0.24$ K/min. Note that at this rate the reversal due to the 1D dynamics (peak 2, $H_{p2} = 0.018$ T) is reached in 0.18 minutes (i.e. ~11 s), which illustrates a lower bound for the characteristic time associated to the 3D magnetic dynamics process. If the system is allowed to organize for a longer period (by sweeping slower), inter-chain exchange interactions will cause the sample to organize in a three-dimensional fashion. Note that for the typical time needed to sweep through the observed hysteresis loops at the critical sweep rate, the characteristic critical energy, $\frac{E_c}{k_B} \sim 0.5$ K, is comparable with the transition temperature, $T = 0.45$ K.

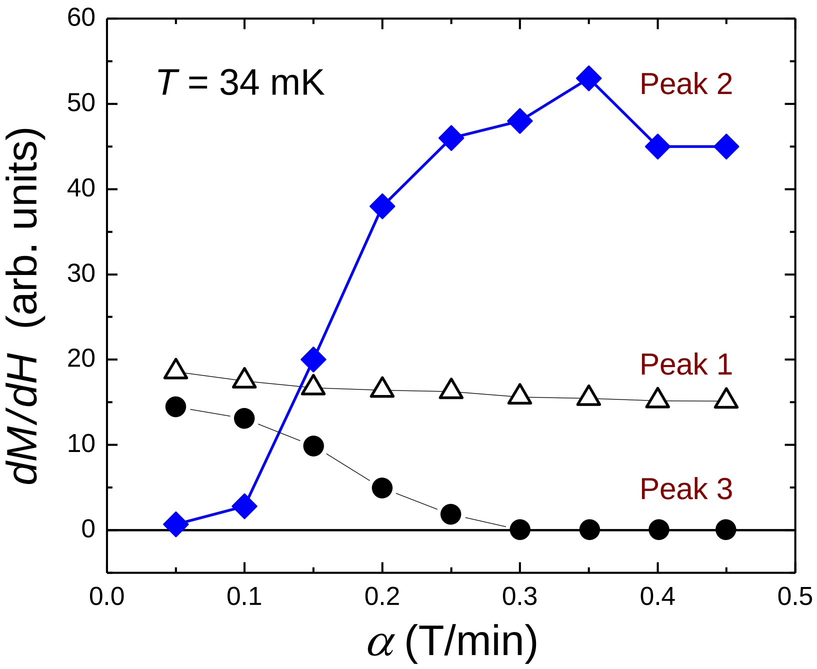

Figure 4-12: In [CoCl$_2$(3,5-Br$_2$py)$_2$], maximum of the susceptibility (dM/dH) calculated from the magnetization as functions of the applied magnetic field sweep rate. The solid curves are guides for the eyes.

4.4 Summary

We have presented detailed characterization of two *trans*-[CoCl$_2$(3,5-X$_2$py)$_2$] SCMs via EPR spectroscopy and Hall-effect magnetometry. The EPR experiments conducted over a wide range of frequencies (50 to 400 GHz) and temperatures (2 to 35 K) reveal infinite chains modeled as a cluster of magnetic segments (domains). The length of each segment results from a competition between the intra-chain exchange coupling between first neighbors, which builds magnetic correlations along the chain, and thermal spin fluctuations that attempt to break the chain into smaller and smaller segments, causing the sample to behave as a collection of individual anisotropic Co^{2+} ions at high enough temperatures. The current study clearly confirms the highly anisotropic nature of the system, with an easy axis type anisotropy coinciding with the chain axis, which emerges from the anisotropic nature of the exchange interaction between neighboring Co^{2+} ions. Furthermore the use of different halogens, X = Br for sample (**1**) and X = Cl for (**2**), allows tuning of the inter-chain interactions within the crystal. Remarkably, a crossover between 1D and 3D magnetic dynamics is obtained by varying the sweep rate of the applied magnetic field. This change in behavior may allow designing new molecular materials with a magnetic response, which depends on the characteristic time of the input stimulus.

CHAPTER 5 CONCLUSIONS

In this chapter a comprehensive summary of the projects discussed above is presented. In this thesis, the magnetic characterization of multi-dimensional molecular magnets is discussed. Different complexes of two types of molecular magnets, namely single-molecule magnets and single-chain magnets are studied using two mostly employed characterization techniques: Hall-effect magnetometry and electron paramagnetic resonance (EPR). In particular low-nuclearity molecules are explored to understand the role of single-ion anisotropy and exchange interactions on the overall magnetic behavior of the molecules.

The thesis begins with a chapter on a general introduction into the defining and unique characteristics associated with molecular magnets and more exclusively the chapter focuses on different relaxation phenomena seen in SMMs and SCMs.

In chapter 2, detailed EPR measurements are provided on a water-stable Mn(IV) mononuclear compound and a weakly ferromagnetically coupled $(\mathrm{Mn(II)})_2$ dimer. Detailed powder and single crystal multi-frequency, high-field EPR spectroscopy measurements show that the Mn(IV) presents a $S = 3/2$ ground spin state with a strong axial anisotropy of the easy-plane type ~ 1.7 cm^{-1}. In addition, spin echo experiments revealed a spin-spin relaxation time T_2 ~ 500 ns. Although this molecule is not a SMM, its strong anisotropic character and its stability in water may enable future technological applications. In the second half, we present a weakly coupled Mn(II) dimer that shows small hysteresis at low temperature. Detailed EPR measurements reveal a complicated energy landscape mostly originating from the inter-dimer interaction present in addition to the inter-ion exchange interactions present within the dimer.

In chapter 3 we discuss the first pristine demonstration that the reduced symmetry of the trinuclear AF Mn_3Zn_2 molecular nanomagnet relieves the spin frustration inherent in most other AF μ_3-oxo-centered triangular Mn_3^{III} complexes. The result is a relatively isolated $S = 2$ ground state that experiences a very significant axial anisotropy due to the near collinearity of the JT axes on the three Mn(III) ions. A significant magnetization hysteresis is observed below $T = 0.8$ K, indicating SMM behavior. A spin-crossover transition is observed at high magnetic fields as predicted by preliminary simulations of the EPR data employing a multi-spin Hamiltonian. These detailed multi-frequency EPR measurements allow us to explore important comparisons between related FM and AF Mn(III) systems that had previously been lacking in the literature.

In chapter 4 we present detailed characterization of two *trans*-$[CoCl_2(3,5\text{-}X_2py)_2]$ SCMs via EPR spectroscopy and DC Hall-effect magnetometry. We discuss a likely interpretation of the EPR resonant peaks observed in a Co-based SCM over a wide range of frequencies (50 to 400 GHz) and temperatures (2 to 35 K) in terms of infinite chains modeled as a cluster of magnetic segments (domains). The length of each segment rises from a competition between the intra-chain exchange coupling between first neighbors, which builds magnetic correlations along the chain, and thermal spin fluctuations that attempt to break the chain into smaller and smaller segments, causing the sample to behave as a collection of individual anisotropic Co^{2+} ions at high enough temperatures. The current study clearly confirms the highly anisotropic nature of the system, with an easy axis type anisotropy coinciding with the chains axis, which emerges from the anisotropic nature of the exchange interaction between neighboring Co^{2+} ions. Furthermore the use of different halogens, X = Br for sample (**1**) and X = Cl for (**2**), allows tuning of the inter-chain interactions within the crystal. Remarkably, a crossover between 1D and 3D magnetic dynamics is obtained by varying the sweep rate of the applied magnetic field. This change in behavior may allow the design of new molecular materials with a magnetic response, which depends on the characteristic time of the input stimulus.

REFERENCES

[1] E. Coranado, P. Delhaès, D. Gatteschi and J.S. Miller, *Molecular Magnetism: From Molecular Assemblies to the Devices, Klumer Academic Publishers* (1996).

[2] M. M. Turnbull, Toyonari Sugimoto and L. K. Thompson, *Molecule-based magnetic materials Theory, Techniques and Applications,* ACS Symposium series 644, (1996).

[3] J. Tejada, *Polyhedron,* **20,** 1751–1756 (2001).

[4] L. Bogani, A. Vindigni, R. Sessoli and D. Gatteschi, *J. Mater. Chem*., **18,** 4750–4758 (2008).

[5] M. N. Leuenberger and D. Loss, *Nature,* **410**, 789 (2001).

[6] J. Tejada, E. M. Chudnovsky, E. del Barco, and J. M. Hernandez, *Nanotechnology*, **12**, 181 (2001).

[7] Y. Nakamura, Yu. A. Pashkin, and J. S. Tsai, *Nature*, **398**, 786 (1999).

[8] T. Hayashi, T. Fujisawa, H. D. Cheong, Y. H. Jeong, and Y. Hirayama, *Phys. Rev. Lett.*, **91**, 26804 (2003).

[9] J. S. Miller, D. Gatteschi, *Chem. Soc. Rev*., 40, 3065-3066, (2011).

[10] J. R. Long, *Chemistry of Nanostructured Materials*; Yang, P., Ed.; World Scientific, Hong Kong, 291-315 (2003).

[11] D. Gatteschi and R. Sessoli, *Angew. Chem. Int., Ed.* 42, No. 3 (2003).

[12] Wolfgang Wernsdorfer, *C. R. Chimie*, 11, 1086-1109 (2008).

[13] S. Hill, S. Datta, J. Liu, R. Inglis, C.J. Milios, P.L. Feng, J.J. Henderson, E. del Barco, E.K. Brechin and D.N. Hendrickson, *Dalton Trans.*, **39**, 4693–4707 (2010).

[14] G. Christou, D. Gatteschi, D. N. Hendrickson and R. Sessoli, *MRS Bulletin*, 25, 66-71 (2000).

[15] A. Caneschi, D. Gatteschi, C. Sangregorio, R. Sessoli, L. Sorace, A.Cornia, M. A. Novak, C. Paulsen and W. Wernsdorfer, *JMMM.*, **200**, 182-201 (1999).

[16] E. M. Chudnovsky and J. Tejada, *Macroscopic Tunneling of the Magnetic Moment* Cambridge University Press, Cambridge (2005).

[17] M-H. Jo, J. E. Grose, K. Baheti, M. Deshmukh, J. J. Sokol, E. M. Rumberger, D. N. Hendrickson, J. R. Long, H. Park, D.C. Ralph, *Nano Lett.*, **6**, 2014-2020 (2006).

[18] Book Review, *An Introduction to Quantum Computing,* by Phillip Kaye, Raymond Laflamme, and Michele Mosca and *Introduction to Quantum Information Science* by Vlatko Vedral, J. R. Friedman, Physics Today, **61**, (2008).

[19] J. R. Friedman and M. P. Sarachik, *Annu. Rev. Condens. Matter Phys.*, **1**, 109 (2010).

[20] W. Wernsdorfer and R. Sessoli, *Science*, **284,** 133-135 (1999).

[21] D. Gatteschi, R. Sessoli and J. Villain, *Molecular Nanomagnets,* Oxford University Press (2006).

[22] T. Lisa, *Acta crystallogr.*, **B36**, 2042-2046 (1980).

[23] R. Sessoli, D. Gatteschi, A. Caneschi and M. A. Novak, *Nature*, **365,** (1993).

[24] J. R. Friedman, M.P. Sarachik, J. Tejada and R. Ziolo, *Phys. Rev. Lett.*, **76,** (1996)

[25] E. del Barco, A. D. Kent, S. Hill, J. M. North, N. S. Dalal, E. M. Rumberger, D. N. Hendrickson, N. Chakov, and G. Christou, *Journal of Low Temperature Physics*, **140**, (2005).

[26] R. J. Glauber, *J. Math. Physics*, **4,** 294 -307 (1963).

[27] A. Caneschi, D. Gatteschi, N. Lalioti, C. Sangregorio, R. Sessoli, G. Venturi, A. Vindigni, A. Rettori, M. G. Pini and M. A. Novak, *Angew. Chem. Int. Ed.*, **40,** No. 9 1760 (2001).

[28] R. Clérac, H. Miyasaka, M. Yamashita and C. Coulon, *J. Am. Chem. Soc.*, **124,** 12837 (2002).

[29] C. Coulon, H. Miyasaka and R. Clérac, *Struct Bond*, **122,** 163–206 (2006).

[30] D. Gatteschi and A. Vindigni, *Arxiv* (2013).

[31] R. Georges, J. J. Borrás-Almenar, E. Coronado, J. Curély and M. Drillon, *Magnetism: Molecules to Materials I: Models and Experiments,* Wiley-VCH Verlag GmbH & Co. KGaA (2003).

[32] H. Sun, Z. Wang and S. Gao, *Coordination Chemistry Reviews*, **254,** 1081–1100 (2010).

[33] H. Miyasaka and R. Clérac, *Bull. Chem. Soc. Jpn*., **78**, 1725 (2005).

[34] H. Miyasaka, M. Julve, M. Yamashita and R. Clérac, *Inorg. Chem.,* **48,** 3420 (2009).

[35] X. Feng, J. Liu, T. D. Harris, S. Hill, and J.R. Long, *J. Am. Chem. Soc.,* **134,** 7521−7529 (2012).

[36] F. Fominaya, J. Villain, P. Gandit, J. Chaussy and A. Caneschi, Phys. Rev. Lett., 79, 1126 (1997).

[37] A. D. Kent, S. von Molnar, S. Gider and D. D. Awschalom, *J. Appl. Phys.*, **76**, 6656 (1994).

[38] P. L. Feng, C.J. Stephenson, A. Amjad, G. Ogawa, E. del Barco and D.N. Hendrickson,. *Inorg Chem.*, **49,** 1304 (2010).

[39] A. Abragam and B. Bleaney, *Electron paramagnetic resonance of transition ions*, Dover publications, Inc (1986).

[40] F. E. Mabbs and D. Collison, *Electron paramagnetic resonance of transition metal compounds,* Elsevier, studies in organic chemistry 16, (1992).

[41] D. Gatteschi, A. L. Barra, A. Caneschi, A. Cornia, R. Sessoli and L. Sorace, *Coordination chemistry Reviews*, **250**, 1514-1529 (2006).

[42] S. Hill, N. S. Dalal, and J. S. Brooks, *Appl. Magn. Reson.,* **16**, 237-45 (1999).

[43] S. Takahashi and S. Hill, *Rev. Sci. Instrum.*, **76**, 023114 (2005).

[44] J. van Tol, L.C. Brunel and R.J. Wylde, *Rev. Sci. Instrum.*, **76,** 074101 (2005).

[45] G.W. Morley, L.C. Brunel, J. van Tol, *Rev. Sci. Instrum.*, **79,** 064703 (2008).

[46] A. K. Hassan, L. A. Pardi, J. Krzystek, A. Sienkiewicz, P. Goy, M. Rohrer and L.-C. J. Brunel, *Magn. Reson.*, **142**, 300−312 (2000).

[47] C. Rovira and J. Veciana, ***CrystEngComm*, 11**, 2031-2031 (2009).

[48] O. Khan, *Molecular magnetism*, VCH Publishers, New York, (1993).

[49] L. F. Jones, C. J. Milios, A. Prescimone, M. Evangelisti and E. K. Brechin, *CRC.*, **11**, 1175 (2008).

[50] R. Sessoli, *Angew. Chem. Int. Edn*., **47**, 5508 (2008).

[51] S. Carretta, E. Liviotti, N. Magnani, P. Santini and G. Amoretti, *Phys. Rev. Lett.*, **92**, 207205 (2004).

[52] D. Gatteschi, R. Sessoli and A. Cornia, *Comprehensive Coordination Chemitry II*, ed. *J. A. McCleverty and T. J. Meyer*, Elsevier, Vol. **7**, 779–813 (2004).

[53] D.N. Hendrickson *et al.*, *J. Am. Chem. Soc.*, **114,** 2455-2471 (1992).

[54] W. Wernsdorfer, N. Aliaga-Alcalde, D.N. Hendrickson and G. Christou, *Nature*, **416,** (2002).

[55] S. Hill, R. S. Edwards, N. Aliaga-Alcalde and G. Christou, *Science*, **302,** (2003).

[56] D. C. Weatherburn, S. Mandal, S. Mukhopadhyay, S. Bahduri and L. F. Lindoy, Manganese in *Comprehensive Coordination Chemistry II*, ed. *J. A. McCleverty and T. J. Meyer*, Elsevier Pergamon, Oxford, Vol. **5**, 1 (2004).

[57] Stephen Blundell, *Magnetism in Condensed Matter* (Oxford University Press, Oxford, 2001).

[58] B. Meunier, *Chem. Rev*., **92**, 1411 (1992).

[59] V. C. Quee-Smith, L. DelPizzo, S. H. Jureller, and J. L. Kerschner, *Inorg. Chem.*, **35**, 6461-6465 (1996).

[60] C. Duboc, M. Collomb, *Chem. Commun.*, 2715-2717 (2009).

[61] J. J. Davies, S. R. P. Smith and J. E. Wertz, *Phys. Rev*., 178, 608 (2008).

[62] Q. Wei and Z.-Y. Yang, *Solid State Commun.*, 146, 307 (2008).

[63] S. Takahashi, J. van Tol, C. C. Beedle, D. N. Hendrickson, L-C. Brunel and M. S. Sherwin, *Phys. Rev. Lett*., **102**, 087603 (2009).

[64] C. N. R. Rao, B. Raveau, *Transition Metal Oxides*; CVCH Publishers: New York, (1995).

[65] R. F. Service, *Science*, **271**, 920 (1996).

[66] D. Gatteschi, A. Caneschi, L. Pardi, R. Sessoli, *Science*, **265**, 1054 (1994).

[67] A. Wilson, J. Lawrence E. C. Yang, M. Nakano, D. N. Hendrickson and S. Hill, Phys. Rev. B., **74**, 140403 (2206).

[68] J. A. Weil, J. R. Bolton and J. E. Wertz, *Electron paramagnetic resonance, elementary theory and practical applications*, John Wiley & sons, INC (1994).

[69] D. V. Efremov and R. A. Klemm, *Phys. Rev. B.*, **74**, 064408 (2006).

[70] R. Sessoli, H. L. Tsai, A. R. Schake, S. Wang, J. B. Vincent, K. Folting, D. Gatteschi, G. Christou and D. N. Hendrickson, *J. Am. Chem. Soc*., **115,** 1804 (1993).

[71] R. E. P. Winpenny, *Magnets and Related Phenomena*, Springer, Structure and Bonding, **122**, (2006).

[72] O. Ciftja, M. Luban, M. Auslender, J. H. Luscombe, *Phys. Rev. B.*, **60**, 10122 (1999).

[73] P. L. Feng, C. Koo, J. J. Henderson, M. Nakano, S. Hill, E. del Barco, and D. N. Hendrickson, *Inorg. Chem*., **47**, 8610 (2008).

[74] J. Laawrence, E.-C. Yang, R. Edwards, M. M. Olmstead, C. Ramsey, N. S. Dalal, P. K. Gantzel, S. Hill, and D. N. Hendrickson, *Inorg. Chem.,* **47**, 1965 (2008).

[75] P. L. Feng, C. Koo, J. Henderson, P. Manning, M. Nakano, E. del Barco, S. Hill, and D. N. Hendrickson, *Inorg. Chem*., **48**, 3480 (2009).

[76] R. Inglis, S. M. Taylor, L. F. Jones, G. S. Papaefstathiou, S. P. Perlepes, S. Datta, S. Hill, W. Wernsdorfer and E. K. Brechin, *Dalton Trans.*, 9157 (2009).

[77] J. Cano, T. Cauchy, E. Ruiz, C. J. Milios, C. C. Stoumpos, T. C. Stamatatos, S. P. Perlepes, G. Christou and E. K. Brechin, *Dalton Trans.*, **234** (2008).

[78] J. J. Henderson, C. Koo, P. L. Feng, E. del Barco, S. Hill, I. S. Tupitsyn, P. C. E. Stamp, and D. N. Hendrickson, *Phys. Rev. Lett*., **103**, 017202 (2009).

[79] R. A. Klemm and D. V. Efremov, *Phys. Rev. B*, **77**, 184410 (2008).

[80] G. H. Wannier, *Physical Rev*., **79**, Issue 2, pp. 357-364 (1950).

[81] R. Mossner, Can. *J. Phys.*, **79**, 1283 (2001).

[82] Y-Z. Zheng, M-L. Tong, W. Xue, W-X. Zhang, X-M. Chen,F. Grandjean, and G. J. Long, *Angew. Chem. Int. Ed.*, **46**, 6076-6080 (2007).

[83] S. Datta, O. Waldmann, A. D. Kent, V. A. Milway, L. K. Thompson, and S. Hill, *Phys. Rev. B,* **76**, 052407 (2007).

[84] S. Datta, E. Bolin, R. Inglis, C. J. Milios, E. K. Brechin, S. Hill, *Polyhedron,* **28**, 1788 (2009).

[85] O. Waldmann, S. Carretta, P. Santini, R. Koch, A. G. M. Jansen, G. Amoretti, R. Caciuffo, L. Zhao, and L. K. Thompson, *Phys. Rev. Lett*., **92**, 096403 (2004).

[86] C. Coulon, R. Clérac, W. Wernsdorfer, T. Colin, H. Miyasaka, *PRL*., **102**, 167204 (2009).

[87] H. Miyasaka, M. Yamashita, *Dalton Trans*., **399** (2007).

[88] J. M. Clemente-Juan, E. Coronado, G. Mínguez Espallargas, H. Adams, L. Brammer, *Cryst. Eng. Comm.*, **12**, 2339 (2010).

[89] L. L. Lohr, J. C. Miller, R. R. Sharp, *J. Chem. Phys.*, **111,** 10148 (1999).

[90] A. B. Boeer, Doctoral thesis.

[91] J. K. L. da Silva et al., *Phys. Rev. E*, 52, 4527 (1995).

[92] J. H. Luscombe et al., *Phys. Rev. E*, 53, 5852 (1996).

[93] J. Lawrence, C. C. Beedle, E. Yang, J. Ma, S. Hill, D. N. Hendrickson, *Polyhedron*, **26,** 2299-2303 (2007).

[94] H. Miyasaka et al., *Chem. Eur. J.*, **16**, 3656 – 3662 (2010).